Supporting Information for

Alloyed Molybdenum Enables Efficient Alcohol Hydrodeoxygenation with Supported Bimetallic Catalysts

Christian Ehinger[a,‡], Stephan Pollitt[b,‡], Jordan De Jesus Silva[a], Xiaoyu Zhou[a], Kazutaka Sakamoto[a], Maarten Nachtegaal[a,b], Olga Safonova[b]*, and Christophe Copéret[a]*

[a]D-CHAB, ETH Zürich, Vladimir–Prelog-Weg 1–5, 8093 Zürich, Switzerland

[b]Center for Energy and Environmental Sciences, PSI, Forschungsstrasse 111, 5232 Villigen, Switzerland

Contents

1. General Considerations

Unless noted otherwise, all syntheses were performed using standard Schlenk techniques under Ar atmosphere or inside an MBraun glovebox filled with Ar. Benzene and benzene-d_6 were dried over Na/benzophenone and distilled before use, and stored over molecular sieves (3 Å). Pentane, toluene and diethyl ether were dried using an MBraun solvent purification system (alumina columns), then subjected to three freeze-pump-thaw cycles and stored over molecular sieves (3 Å). $SiO_{2\text{-}700}$ (from compacted Degussa Aerosil-200 by Evonik, BET Surface area ca. 200 m^2/g) was prepared according to published procedures.[1] Across several batches, OH densities on $SiO_{2\text{-}700}$ ranged 0.28–0.30 mmol/g, ~1 OH/nm^2. The surface OH density was determined by titration using $[Mg(CH_2Ph)_2(THF)_2]$ (prepared according to published procedures[2]) in C_6D_6 and quantification of toluene by ^{1}H-NMR spectroscopy, using ferrocene, prepared according to published procedures,[3] as internal standard. Celite® and molecular sieves (3 Å) were activated by evacuation at 10^{-5} mbar and 350 °C for ca. 12 h. Deionized water was collected from Merck Millipore Synergy® Water Purification System. The organometallic amidinate (*N*,*N*'-diisopropylacetamidinate, DIA) precursors used for the synthesis of supported nanoparticles were prepared according to published procedures (M = Ni, Pd, Pt: M(allyl)(DIA), M = Rh, Ir: M(COD)(DIA)).[4-6]

Solution NMR Spectroscopy: Solution ^{1}H-NMR and were recorded on a 300 MHz Bruker DRX spectrometer at room temperature. Spectra were processed, analyzed, and plotted using the MestreNova software package. For quantification of graftings or -OH densities, ferrocene ($FeCp_2$) was used as internal standard, and extended recycle delay (58 s) was used to ensure accurate quantification.

Elemental analysis: EA was performed by Mikroanalytisches Labor Pascher (an der Pulvermühle 1, D-53424 Remagen, Germany) using ICP-AES.

IR Spectroscopy: IR spectra were recorded inside an Ar-filled glovebox on a Bruker FT-IR Alpha spectrometer. Molecular complexes were measured using ATR-IR, silica- and alumina-based materials were measured in transmission mode. Stacked spectra of silica-based materials were baseline corrected and normalized with respect to the Si-O-Si overtone band maximum at 1868 cm^{-1}. For adsorption experiments (CO), spectra were recorded in transmission mode on a Nicolet 6700 FTIR spectrophotometer, equipped with an uncooled deuterated tryglycine sulfate (DTGS)KBr detector, using 32 scans at a resolution of 2 cm^{-1}. For adsorption experiments, a wafer of catalyst material was pressed into an aluminum ring, which was placed into a glass IR cell with CaF_2 windows. For IR spectra with adsorbed CO, the evacuated cell was exposed to different pressures incrementally (typically ca. 2.5, 10, 50 mbar) at 298 K and a spectrum was recorded after each dosage. Finally, the cell was evacuated for ca. 10 minutes and another spectrum was recorded.

Electron Microscopy: Micrographs of the materials were acquired by high angle annular dark-field scanning transmission electron microscopy (HAADF-STEM). The instrument used was a FEI Talos F200X, which was operated at 200 KV. Samples were prepared by placing a powder on a Lacey-C 400 mesh Cu grid in a glovebox under Ar atmosphere, then transferring the grid to the microscope using a vacuum transfer tomography holder from Fischione Instruments (model #2560). This ensured that the samples were transferred into the microscope without exposure to air. To evaluate particle size, particles were measured manually from the micrographs. Approximately 200 particles were measured for each sample.

CO-Chemisorption: CO-Chemisorption was performed using a BELSORP MAX X gas and vapor adsorption analyzer from Microtrac. Ca. 100 mg of sample was transferred air-free to the sample cell. First, a pre-treatment consisiting dosing 100 mbar H_2 at 250 °C for 10 min, followed by evacuation for 30 min at 250 °C was performed. Then the CO uptake was measured at 25 °C. The uptake for

generating a monolayer of CO was determined as the axis intercept from interpolating the points after the initial jump with a linear regression between p=5 kPa and p=45 kPa. The data was normalized by amount of surface metal estimated from TEM, this corresponds to normalizing by total metal content and dispersion (where the dispersion is the ratio of metal atoms on the surface of a spherical nanoparticle of a given diameter).[7]

2. Synthesis of Materials

MoO_3/SiO_2. MoO_3/SiO_2 with a target Mo loading of 0.33% was prepared by incipient wetness impregnation. Previous reports have shown that at low weight percentage (i.e. < 8 wt-% Mo) only bipedal isolated Mo(VI) dioxo sites are formed, without formation of bulk oxide domains.[8, 9]

SiO_2 (Aerosil Degussa, 200 m^2/g) was compacted with deionized water and dried at 100 °C for 7 days. The obtained agglomerates were crushed with a mortar and sieved for the fraction in the 250–400 µm range to give a white, free flowing powder for easy handling. The point of incipient wetness for this material was determined at 1.6 g H_2O/ g SiO_2.
Compacted SiO_2 (5.5 g, dried at 100 °C for 24 h) was treated with a solution of $(NH_4)_6Mo_7O_{24} \cdot 4 H_2O$ (34 mg) in deionized H_2O (8.8 mL), by dropwise addition and occasional stirring with a glass rod, without crushing the material. The obtained material was dried at room temperature for 72 h, then at 80 °C for 24 h, before calcination under a flow of dry synthetic air (120 °C for 2 h, then 500 °C for 6 h; heating ramp 1 °C/min). The reactor was cooled down under vacuum (for 2 h, 10^{-5} mbar). The obtained white material was recovered in the glovebox and stored under an inert Ar atmosphere.

Monometallic materials. Monometallic materials were prepared in two steps: first the respective organometallic amidinate precursor was grafted onto $SiO_{2\text{-}700}$, then the obtained material was subjected to a hydrogen-temperature treatment.[4-6]

Bimetallic materials. Bimetallic materials were prepared in two steps: first the respective organometallic amidinate precursor was grafted onto MoO_3/SiO_2, then the obtained material was subjected to a hydrogen-temperature treatment.

General procedure A: Grafting of Organometallic Precursors
The support material was transferred to a Schlenk flask equipped with a stir bar and dispersed in benzene (ca. 10 mL benzene /g support). The respective organometallic precursor (target 0.25 mmol metal /g support) was weighed in a vial and dissolved in benzene (ca. 10 mL benzene /g support). The precursor solution was added dropwise over ca. 5 min to the support suspension while stirring at 200 rpm and occasional light shaking of the Schlenk flask. The obtained mixture was then stirred at 100 rpm for 4 h. The liquid was decanted, and the material was washed with benzene (2 x 10 mL/g) and pentane (2 x 10 mL/g), then dried at 10^{-5} mbar for 1 h. All handlings and storage are performed under protective Ar atmosphere in a glovebox. Grafting was confirmed by IR spectroscopy, from the decrease of the OH stretching band intensity and the emergence of bands associated with C–H bonds and, characteristic for the protonation of the amidinate ligand, a C=N stretching band (Section SXX).

General procedure B: Hydrogen Treatment
The grafted material was transferred to a reactor with a frit. A flow of hydrogen is established (ca. 60 mL/min), and the materials are heated at 500 °C for 8-12 h (heating ramp 1 °C/min). The materials are cooled down at 10^{-5} mbar, and transferred to a glovebox without exposure to air. Removal of organic residues, and restoration of OH groups was confirmed by IR spectroscopy. Formation of nanoparticles was confirmed by HAADF-STEM imaging (Section SXX).

Ni/SiO_2: Prepared according to General Procedure A and B, with $SiO_{2\text{-}700}$ and Ni(allyl)(DIA). Black material.
Elemental analysis: Ni 1.36%.

Pd/SiO_2: Prepared according to General Procedure A and B (final temperature at 400 °C instead of 500 °C) with $SiO_{2\text{-}700}$ and Pd(allyl)(DIA). Black material.
Elemental analysis: Pd 2.59%.

Pt/SiO_2: Prepared according to General Procedure A and B (final temperature at 300 °C instead of 500 °C) with $SiO_{2\text{-}700}$ and Pt(allyl)(DIA). Black material.
Elemental analysis: Pt 3.98%.

Rh/SiO_2: Prepared according to General Procedure A and B (final temperature at 400 °C instead of 500 °C) with $SiO_{2\text{-}700}$ and Rh(COD)(DIA). Black material.
Elemental analysis: Rh 2.38%.

Ir/SiO_2: Prepared according to General Procedure A and B, with $SiO_{2\text{-}700}$ and Ir(COD)(DIA). Black material.
Elemental analysis: Ir 4.32%.

Ni-Mo/SiO_2: Prepared according to General Procedure A and B, with MoO_3/SiO_2 and Ni(allyl)(DIA). Black material.
Elemental analysis: Ni 1.33%, Mo 0.30%.

Pd-Mo/SiO_2: Prepared according to General Procedure A and B, with MoO_3/SiO_2 and Pd(allyl)(DIA). Black material.
Elemental analysis: Pd 2.41%, Mo 0.22%.

Pt-Mo/SiO_2: Prepared according to General Procedure A and B, with MoO_3/SiO_2 and Pt(allyl)(DIA). Black material.
Elemental analysis: Pt 3.56%, Mo 0.28%.

Rh-Mo/SiO_2: Prepared according to General Procedure A and B, with MoO_3/SiO_2 and Rh(COD)(DIA). Black material.
Elemental analysis: Rh 2.44%, Mo 0.27%.

Ir-Mo/SiO_2: Prepared according to General Procedure A and B, with MoO_3/SiO_2 and Ir(COD)(DIA). Black material.
Elemental analysis: Ir 4.26%, Mo 0.27%.

3. IR Spectra

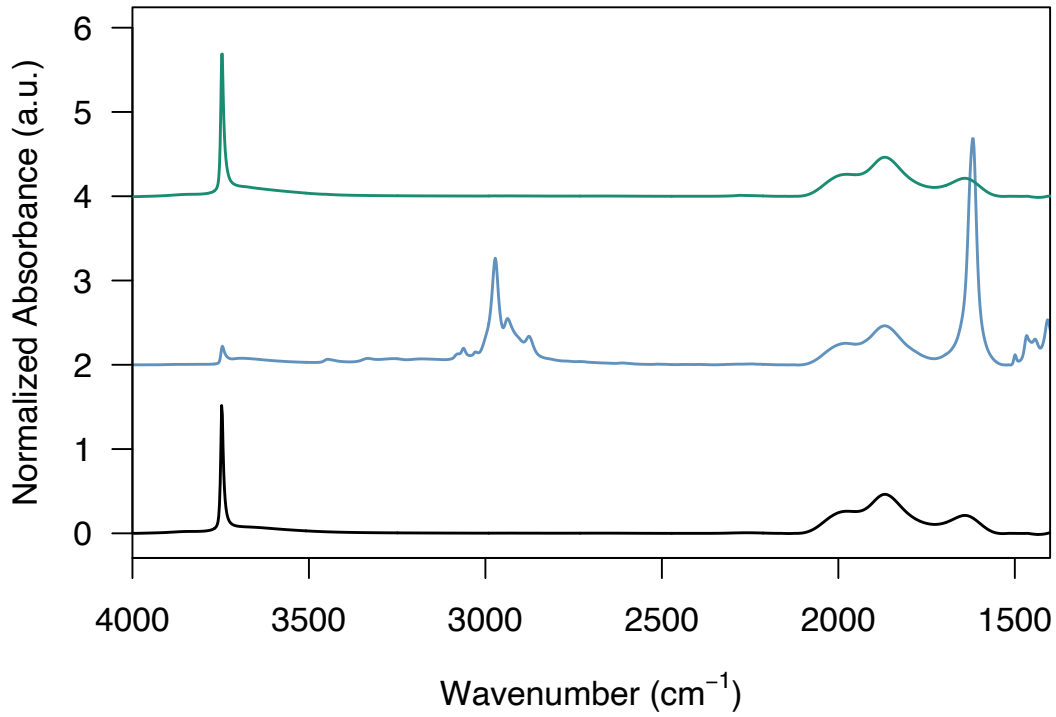

Figure S1. IR spectra of $SiO_{2\text{-}700}$ (black spectrum), Ni(allyl)(DIA)/$SiO_{2\text{-}700}$ (blue spectrum), and Ni/SiO_2 (green spectrum).

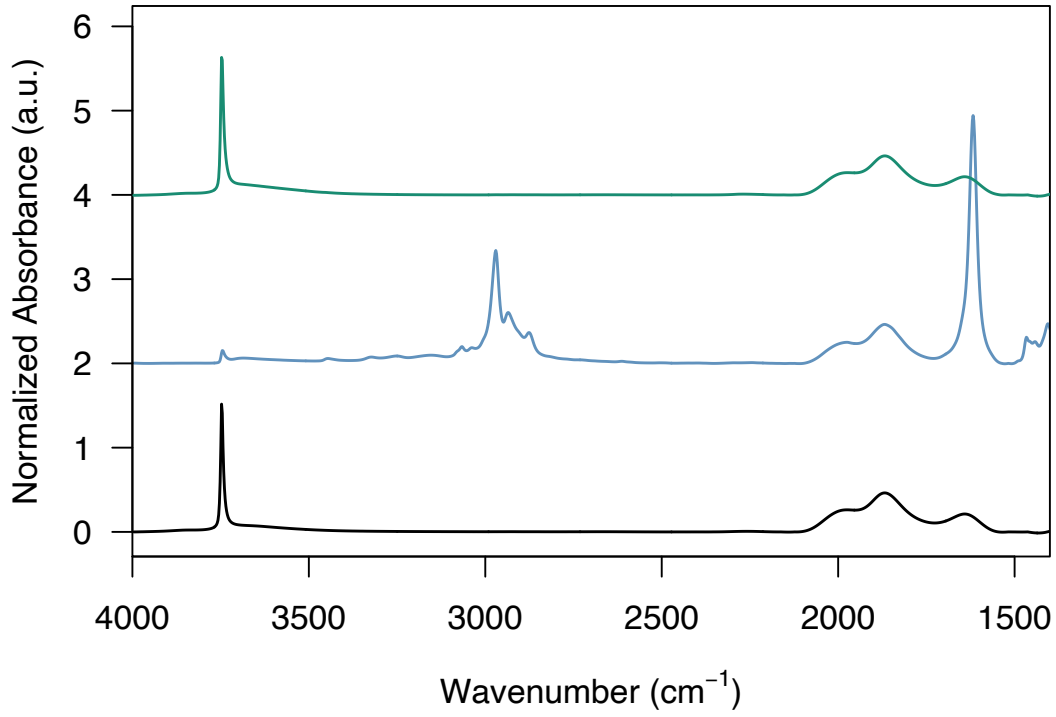

Figure S2. IR spectra of $SiO_{2\text{-}700}$ (black spectrum), Pd(allyl)(DIA)/$SiO_{2\text{-}700}$ (blue spectrum), and Pd/SiO_2 (green spectrum).

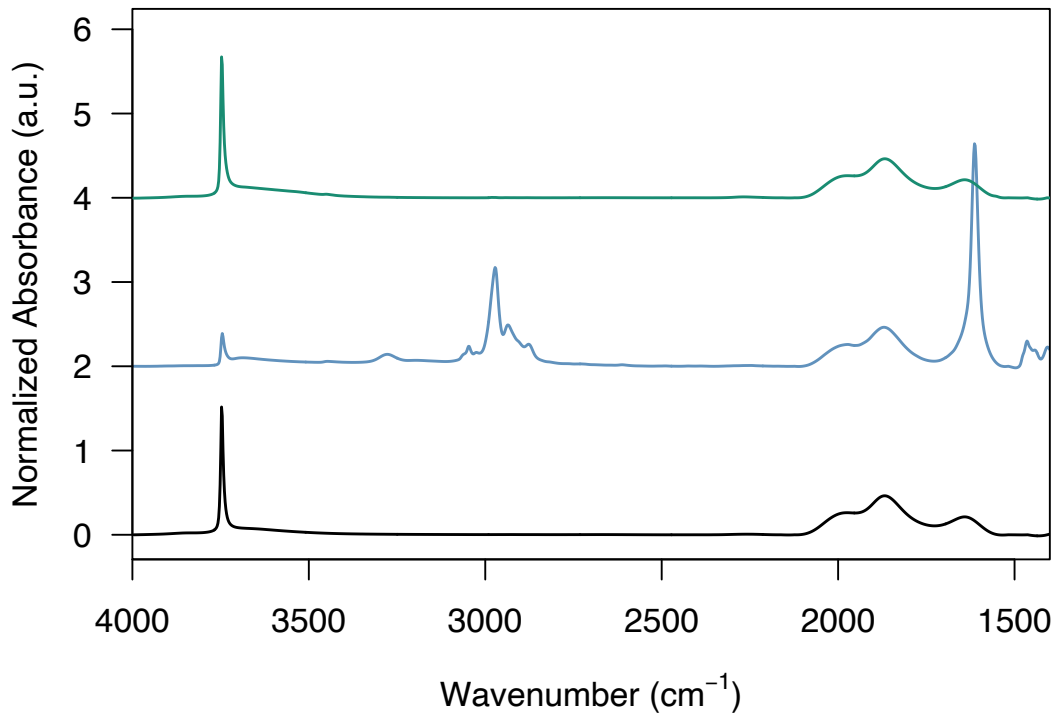

Figure S3. IR spectra of $SiO_{2\text{-}700}$ (black spectrum), Pt(allyl)(DIA)/$SiO_{2\text{-}700}$ (blue spectrum), and Pt/SiO_2 (green spectrum).

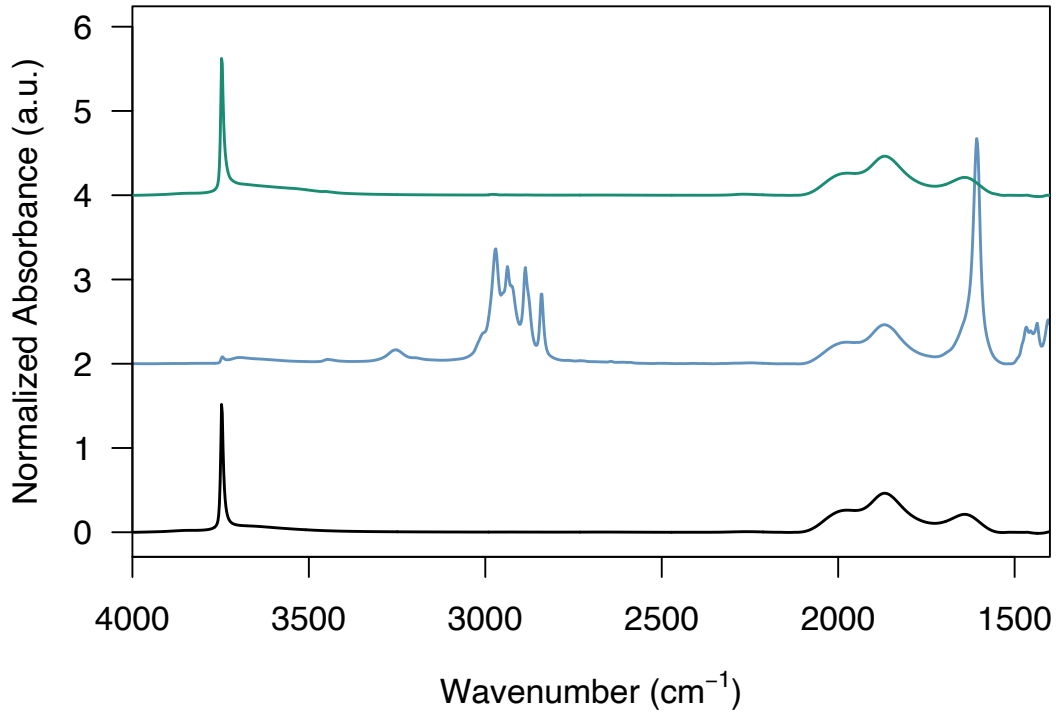

Figure S4. IR spectra of $SiO_{2\text{-}700}$ (black spectrum), Rh(COD)(DIA)/$SiO_{2\text{-}700}$ (blue spectrum), and Rh/SiO_2 (green spectrum).

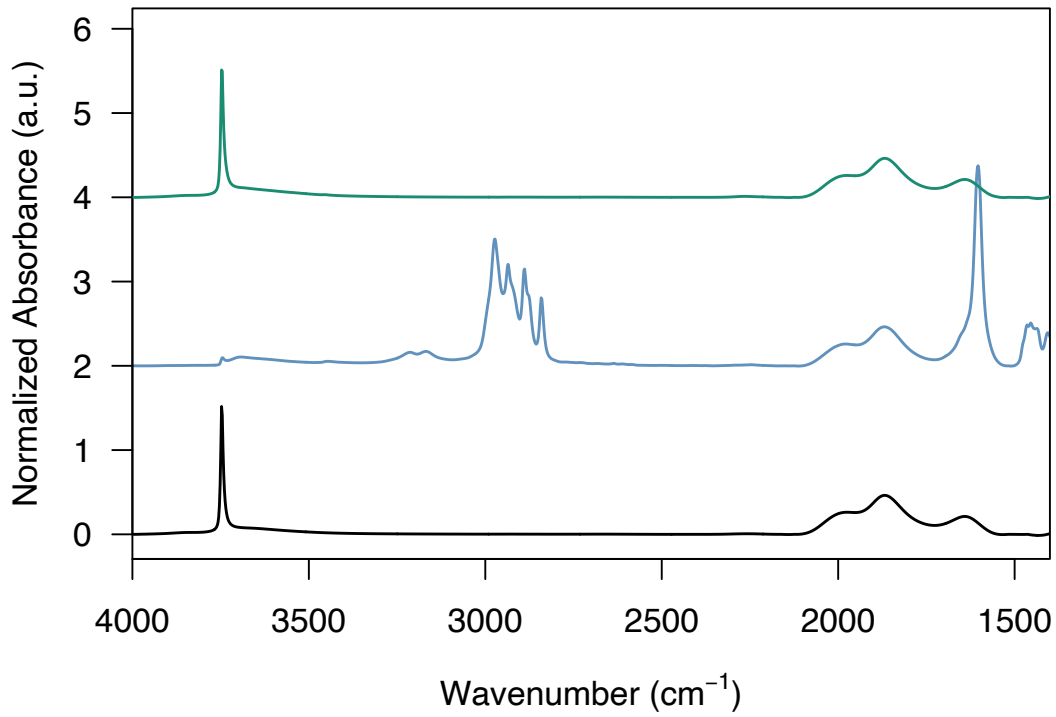

Figure S5. IR spectra of $SiO_{2\text{-}700}$ (black spectrum), Ir(COD)(DIA)/$SiO_{2\text{-}700}$ (blue spectrum), and Ir/SiO_2 (green spectrum).

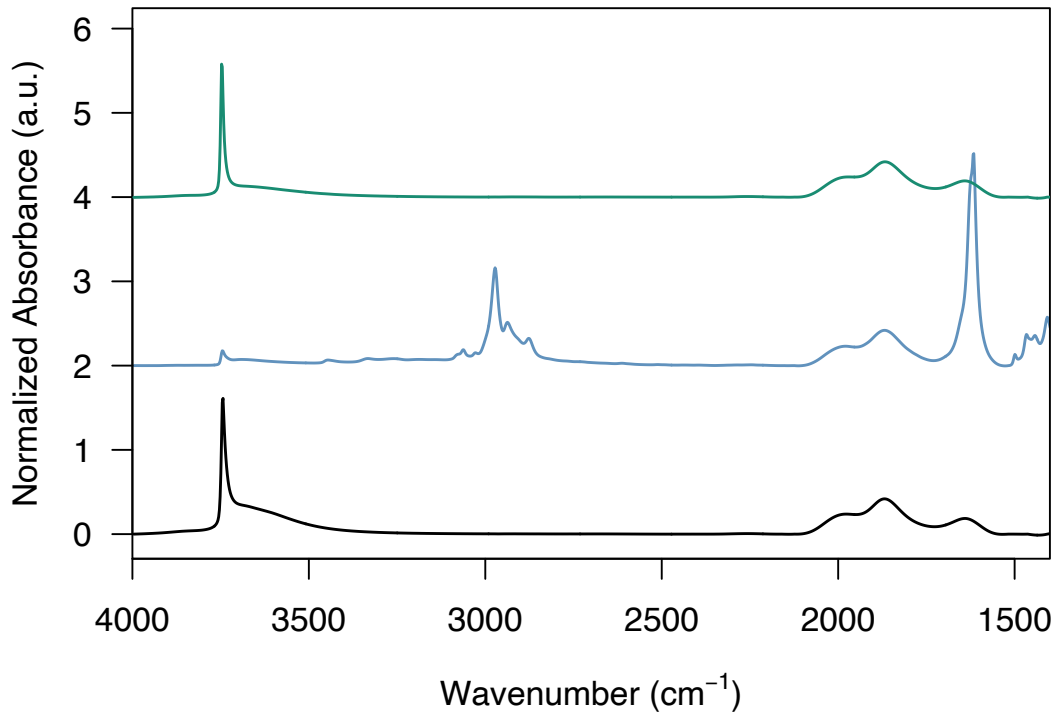

Figure S6. IR spectra of MoO_3/SiO_2 (black spectrum), Ni(allyl)(DIA)/MoO_3/SiO_2 (blue spectrum), and Ni-Mo/SiO_2 (green spectrum).

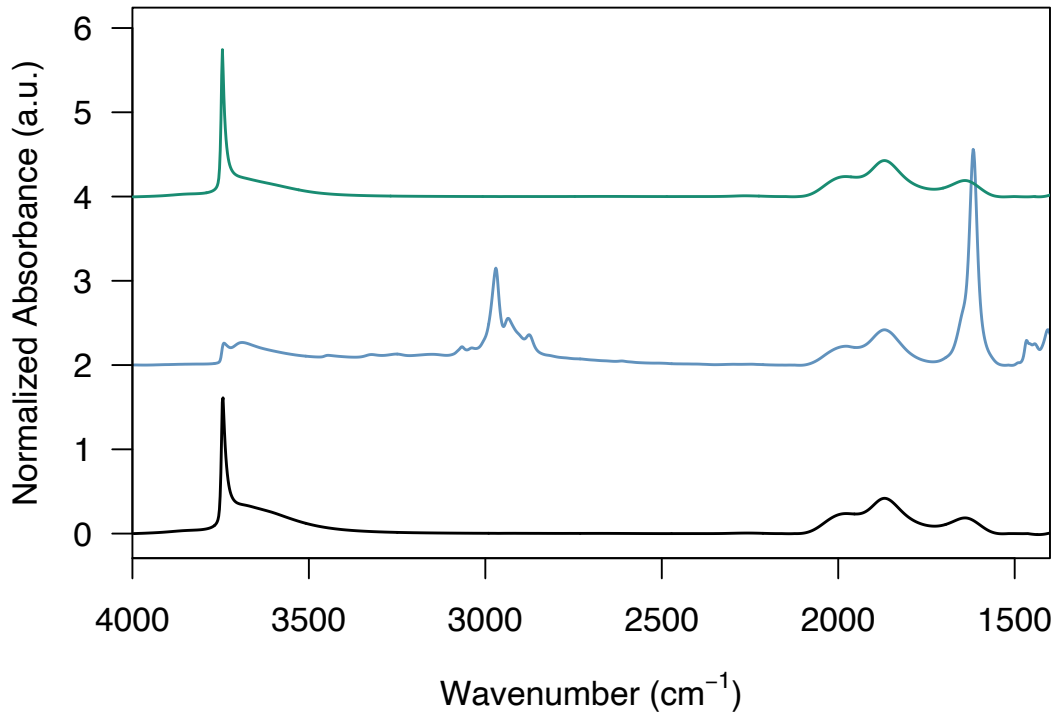

Figure S7. IR spectra of MoO_3/SiO_2 (black spectrum), Pd(allyl)(DIA)/MoO_3/SiO_2 (blue spectrum), and Pd-Mo/SiO_2 (green spectrum).

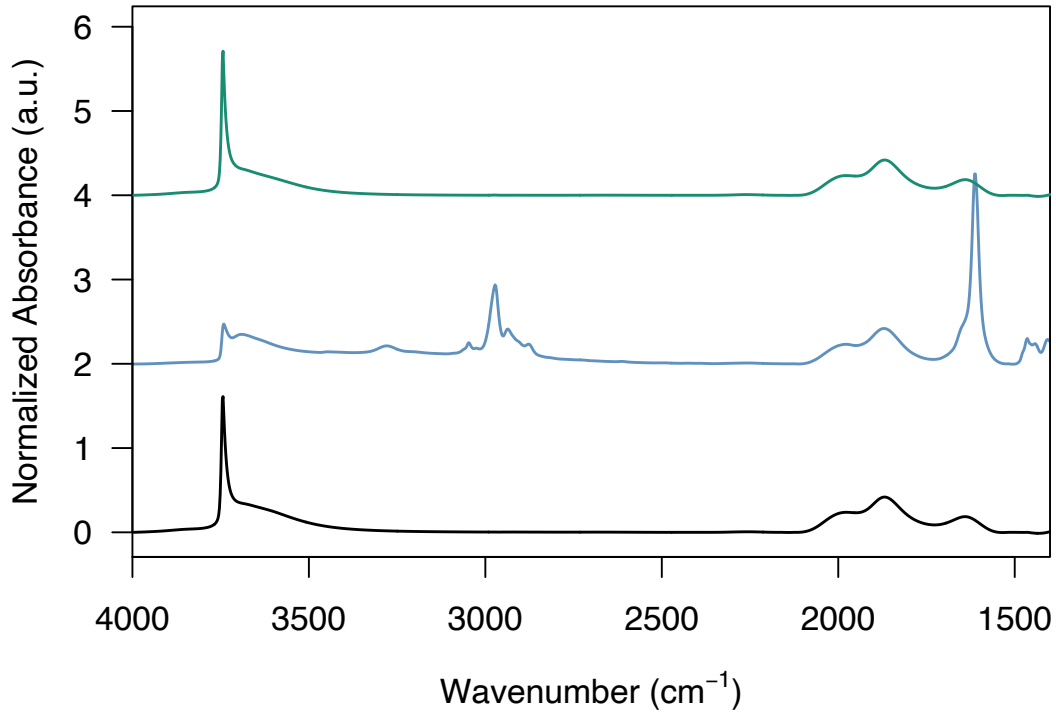

Figure S 8. IR spectra of MoO_3/SiO_2 (black spectrum), Pt(allyl)(DIA)/MoO_3/SiO_2 (blue spectrum), and Pt-Mo/SiO_2 (green spectrum).

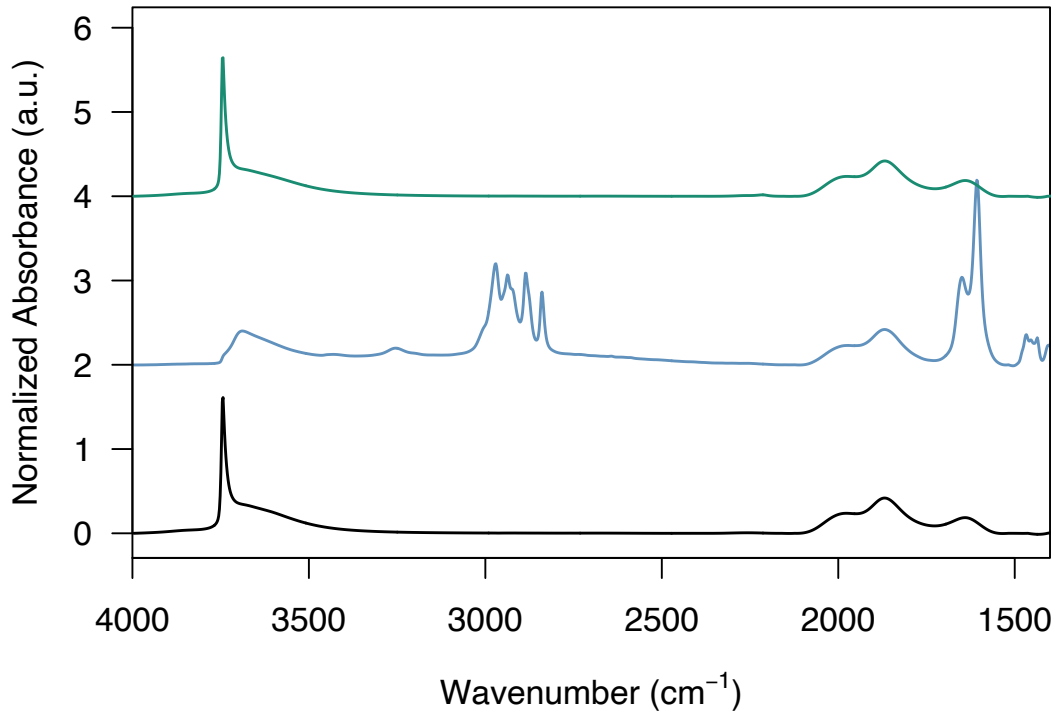

Figure S9. IR spectra of MoO_3/SiO_2 (black spectrum), Rh(COD)(DIA)/MoO_3/SiO_2 (blue spectrum), and Rh-Mo/SiO_2 (green spectrum).

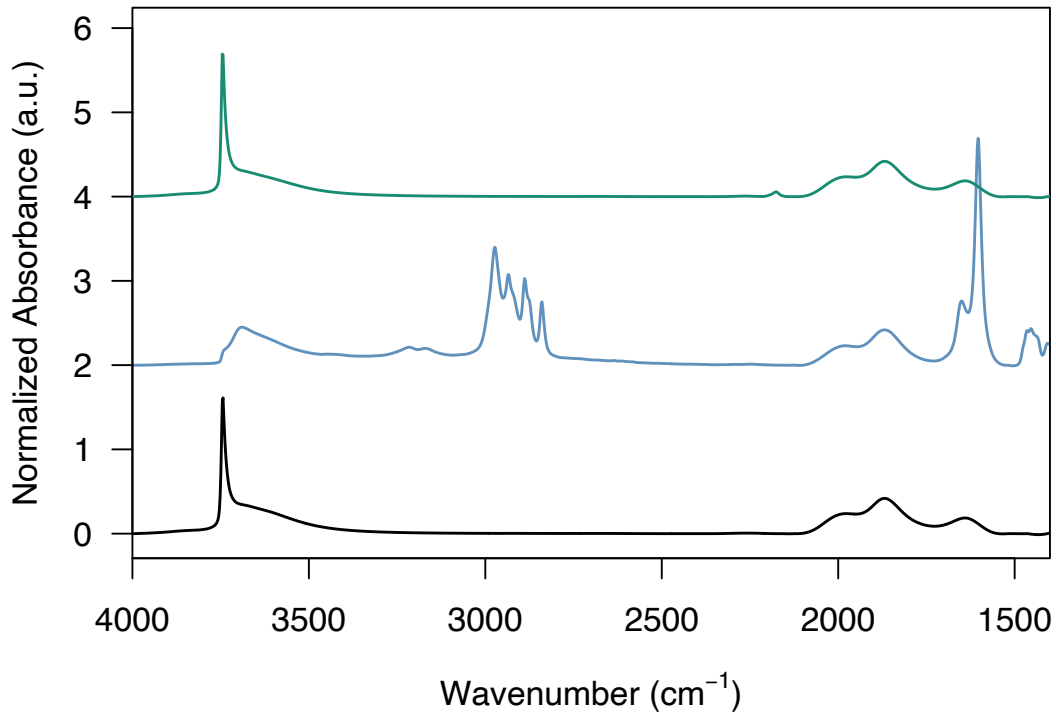

Figure S10. IR spectra of MoO_3/SiO_2 (black spectrum), Ir(COD)(DIA)/MoO_3/SiO_2 (blue spectrum), and Ir-Mo/SiO_2 (green spectrum).

4. CO-IR Spectra

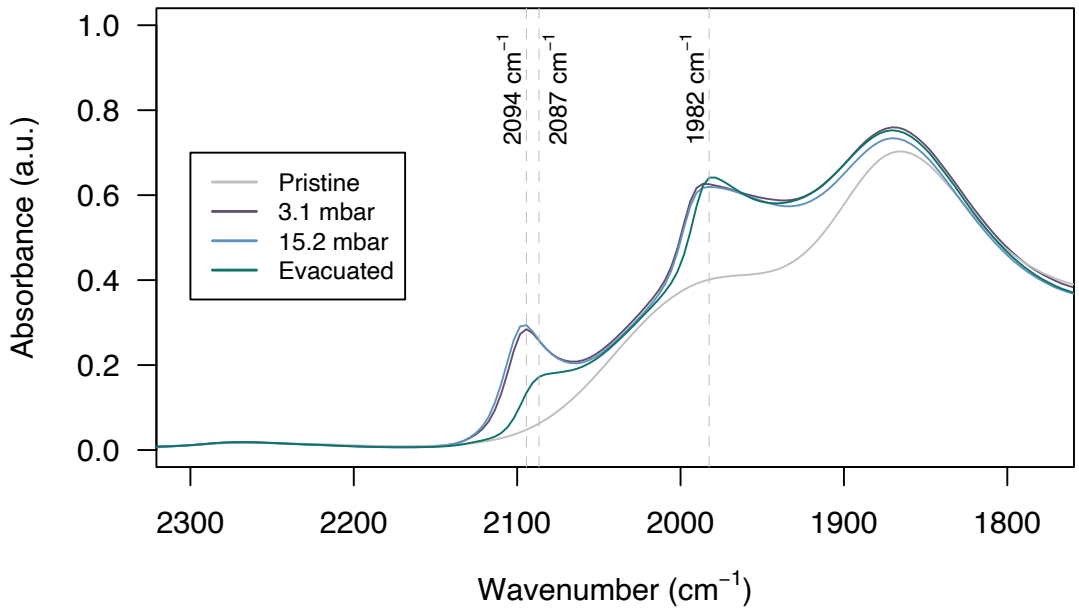

Figure S11. CO-Adsorbed IR spectra of Pd/SiO_2 at various pressures of CO.

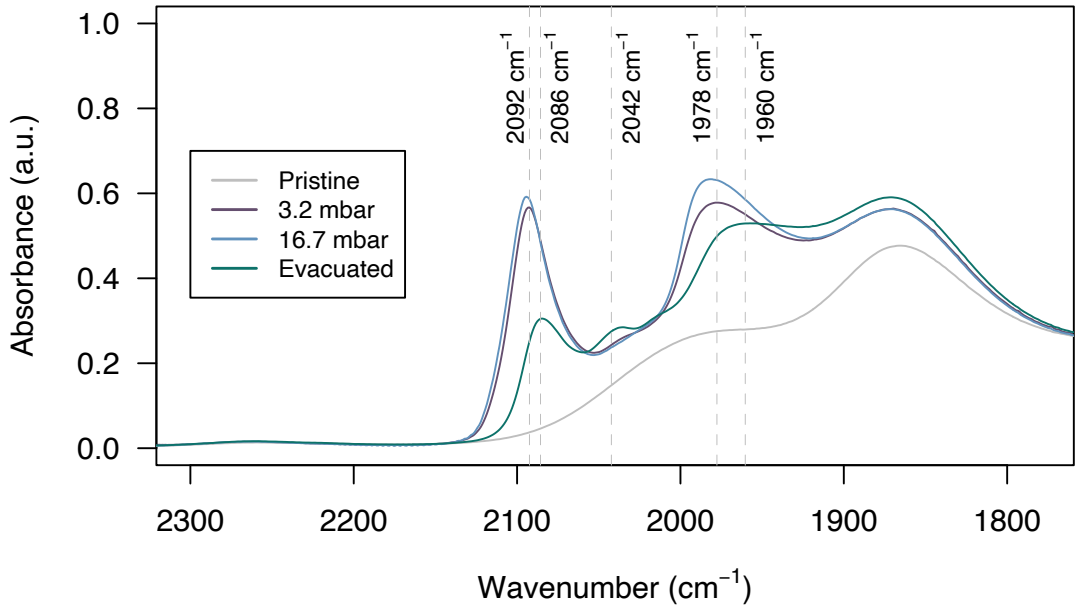

Figure S12. CO-Adsorbed IR spectra of $Pd\text{-}Mo/SiO_2$ at various pressures of CO.

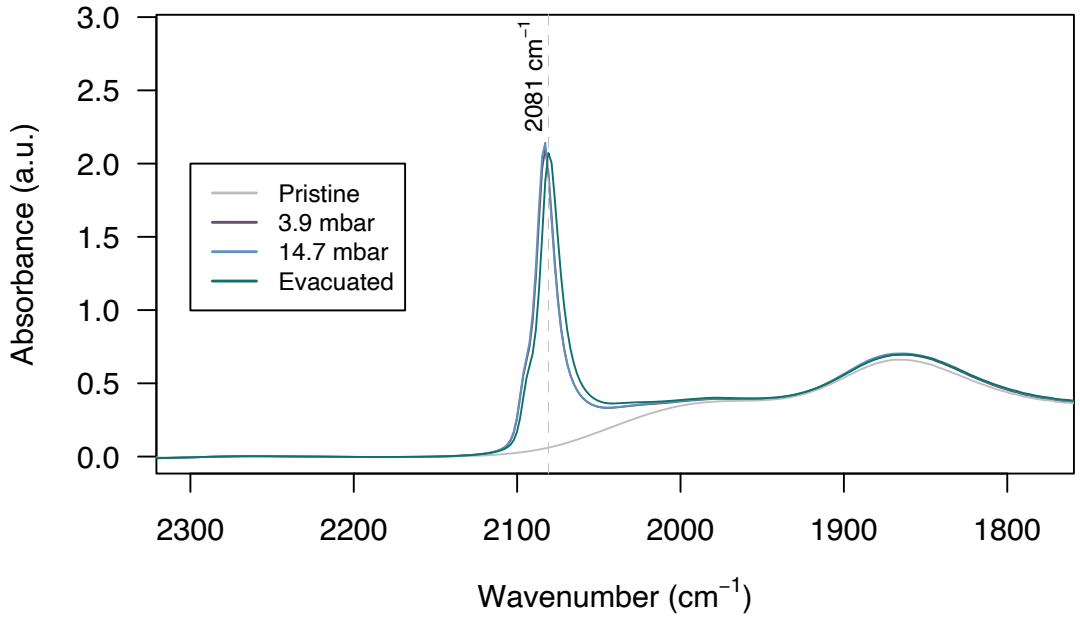

Figure S13. CO-Adsorbed IR spectra of Pt/SiO_2 at various pressures of CO.

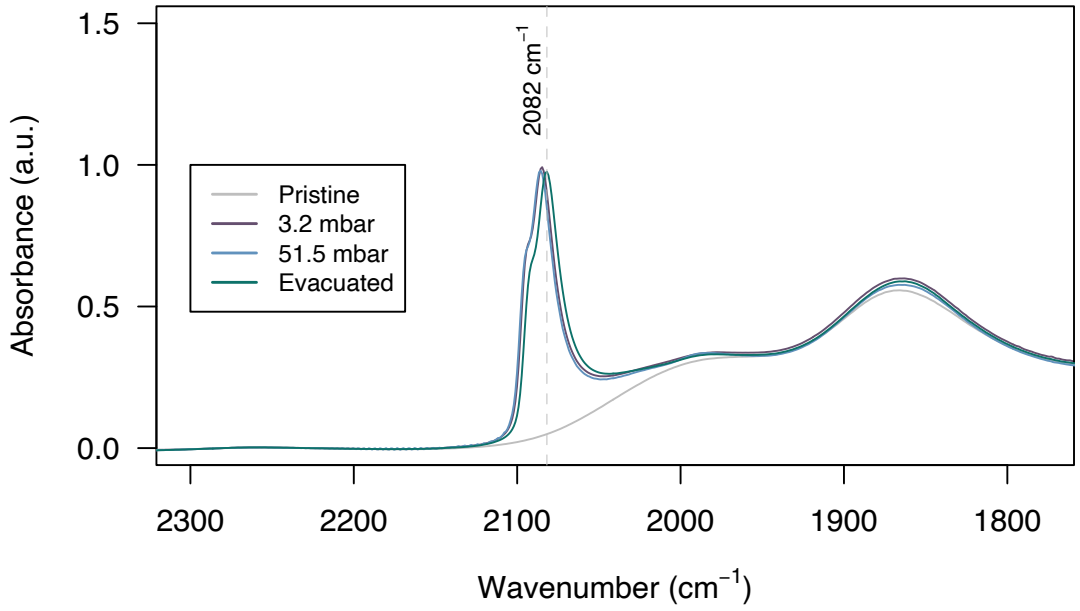

Figure S14. CO-Adsorbed IR spectra of $Pt\text{-}Mo/SiO_2$ at various pressures of CO.

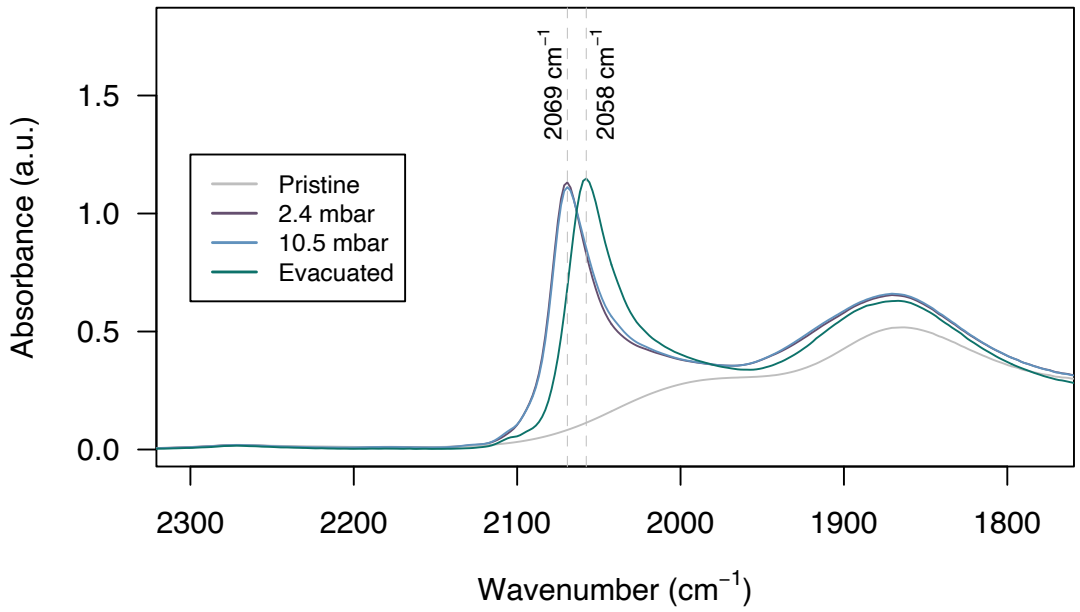

Figure S15. CO-Adsorbed IR spectra of Rh/SiO_2 at various pressures of CO.

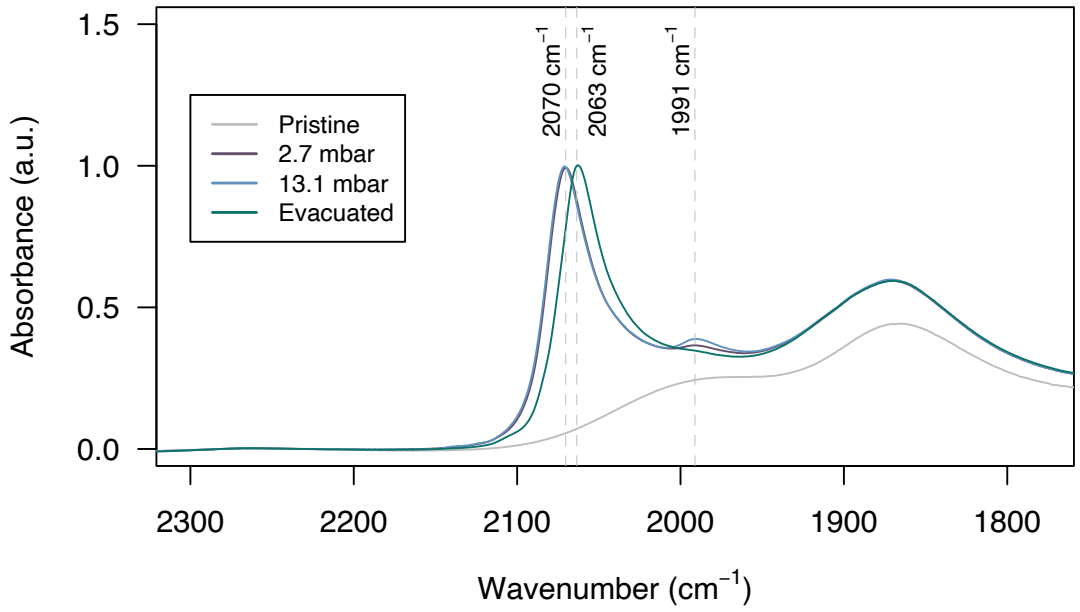

Figure S16. CO-Adsorbed IR spectra of $Rh\text{-}Mo/SiO_2$ at various pressures of CO.

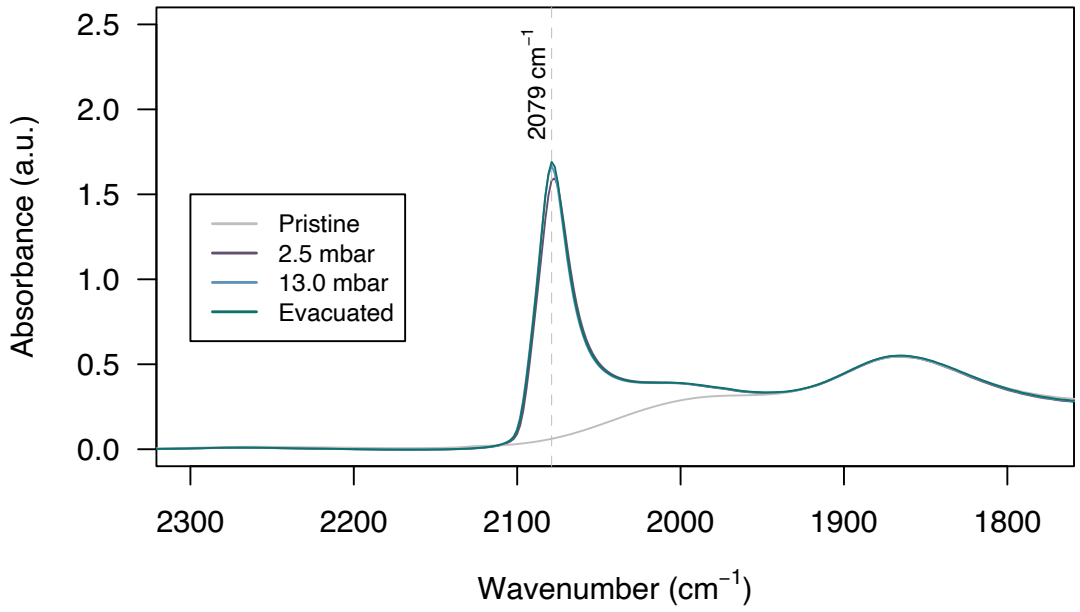

Figure S17. CO-Adsorbed IR spectra of Ir/SiO_2 at various pressures of CO.

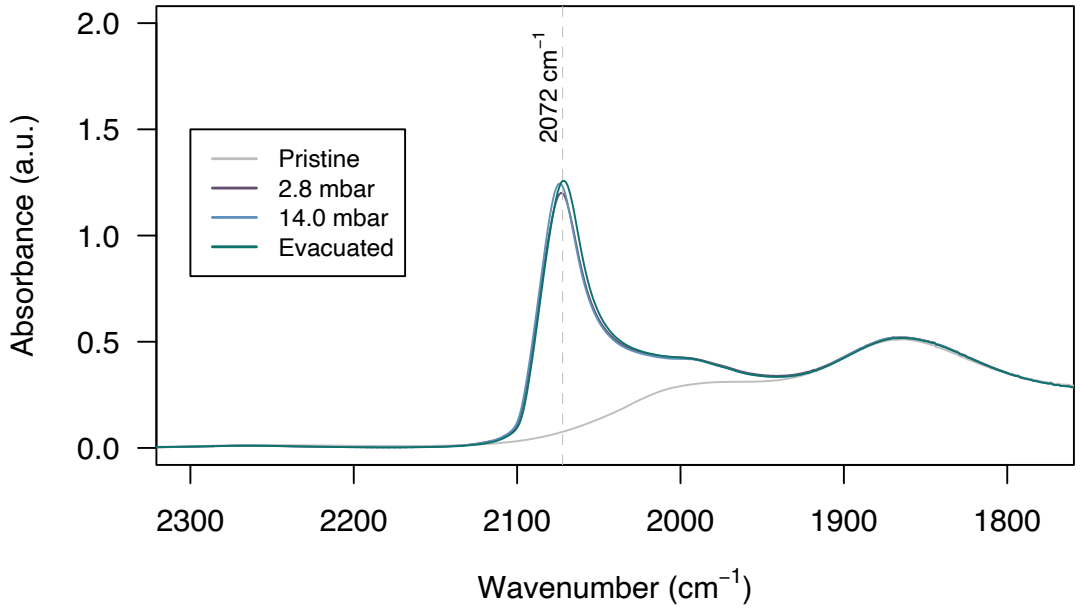

Figure S18. CO-Adsorbed IR spectra of $Ir\text{-}Mo/SiO_2$ at various pressures of CO.

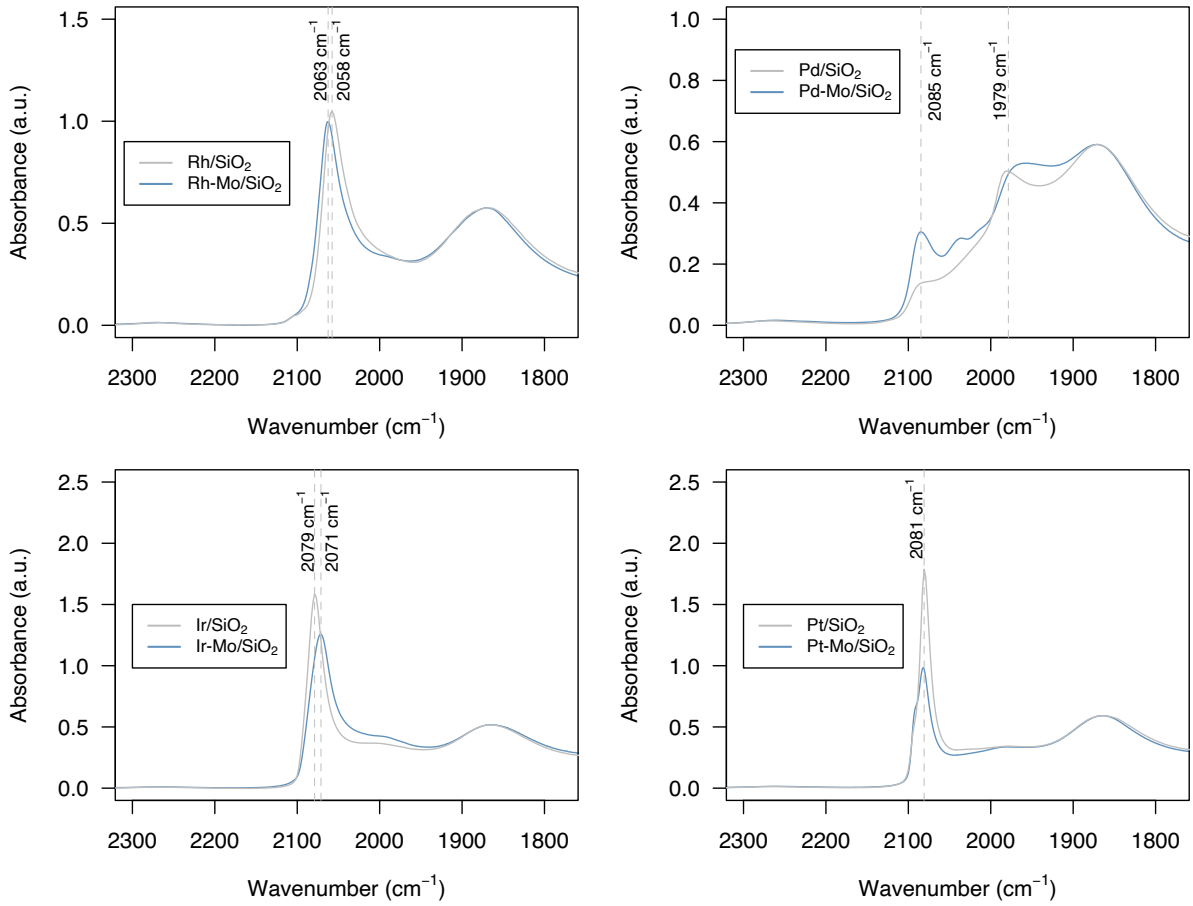

Figure S19. CO adsorbed IR-spectra of mono- and bimetallic materials after dosing ca. 10–20 mbar CO followed by evacuation at 10^{-5} mbar for 10 minutes. Spectra are normalized with respect to the Si–O–Si band at 1868 cm^{-1} for comparison of intensity of CO bands.

5. Electron Microscopy

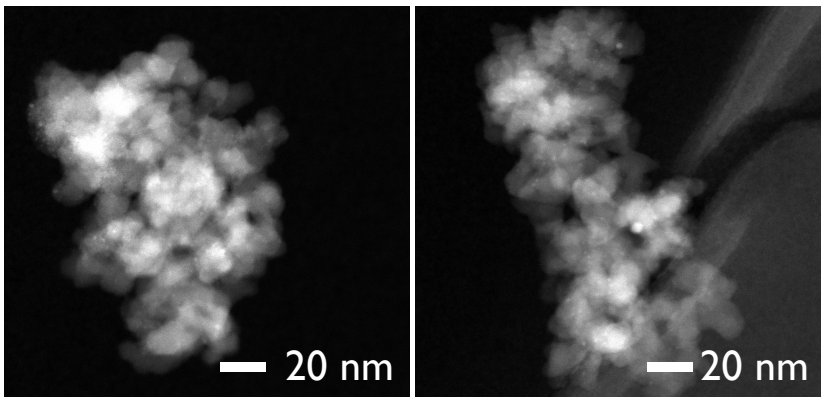

Figure S20. HAADF-STEM micrographs of NiMo/SiO_2. While visible, most of the particles were too small to allow for an accurate determination particle size distribution, and the average diameter was estimated at <1 nm.

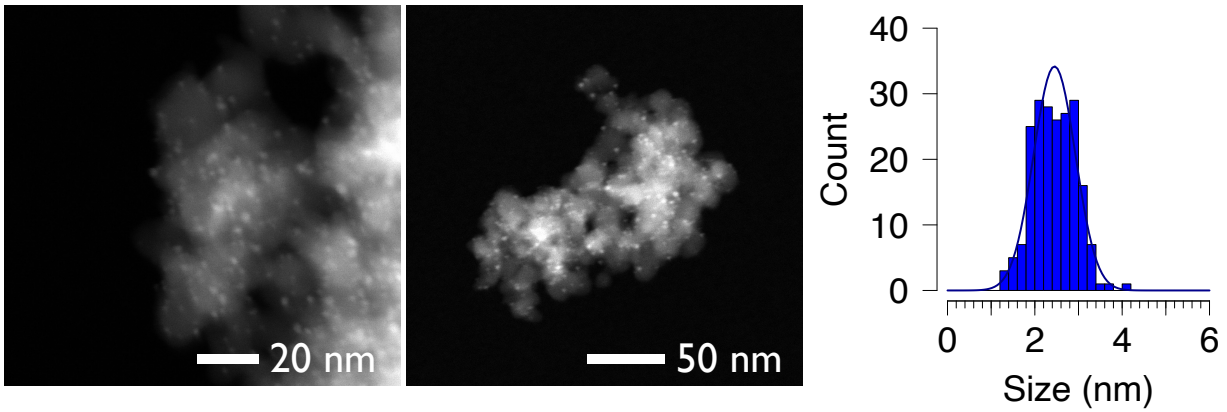

Figure S21. HAADF-STEM micrographs and particle size distribution histogram of PdMo/SiO_2. The fitted normal distribution has a mean value μ = 2.5 nm, with a standard deviation σ = 0.5 nm, for N = 205 particles counted.

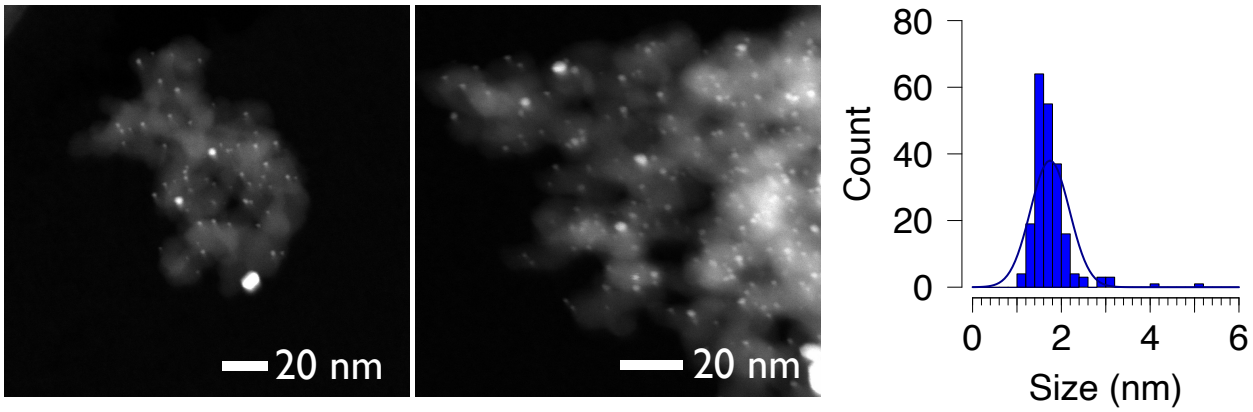

Figure S22. HAADF-STEM micrographs and particle size distribution histogram of PtMo/SiO_2. The fitted normal distribution has a mean value μ = 1.7 nm, with a standard deviation σ = 0.4 nm, for N = 210 particles counted.

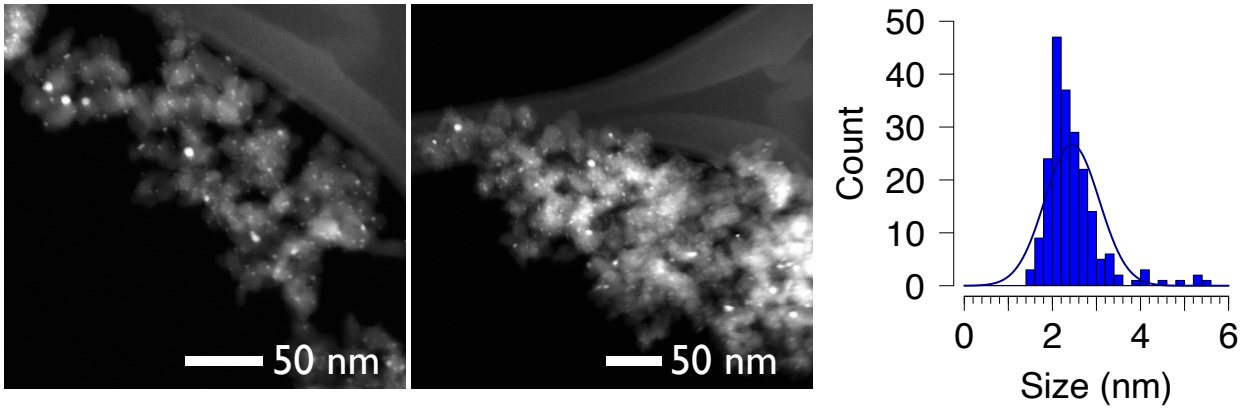

Figure S23. HAADF-STEM micrographs and particle size distribution histogram of $RhMo/SiO_2$. The fitted normal distribution has a mean value $\mu = 2.4$ nm, with a standard deviation $\sigma = 0.6$ nm, for N = 207 particles counted.

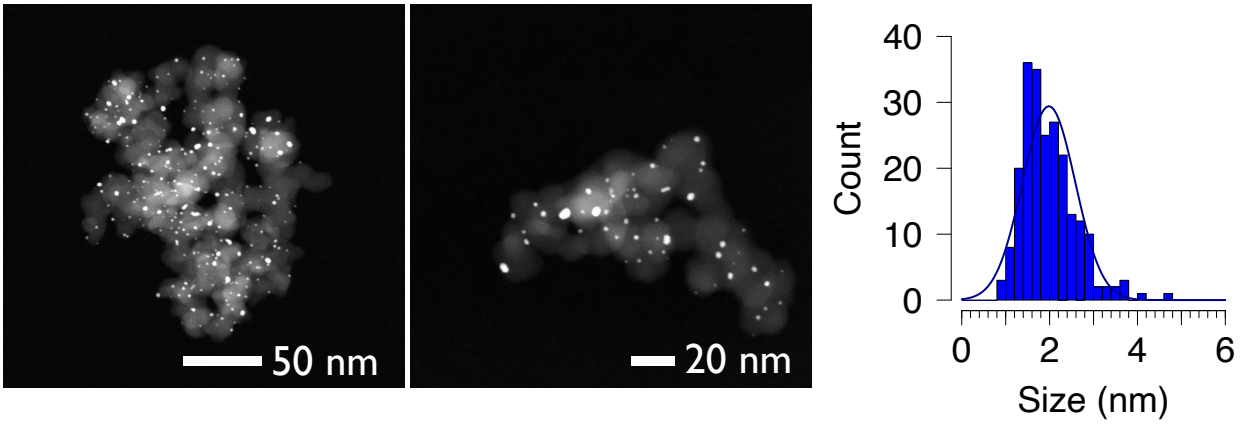

Figure S24. HAADF-STEM micrographs and particle size distribution histogram of $IrMo/SiO_2$. The fitted normal distribution has a mean value $\mu = 2.0$ nm, with a standard deviation $\sigma = 0.6$ nm, for N = 222 particles counted.

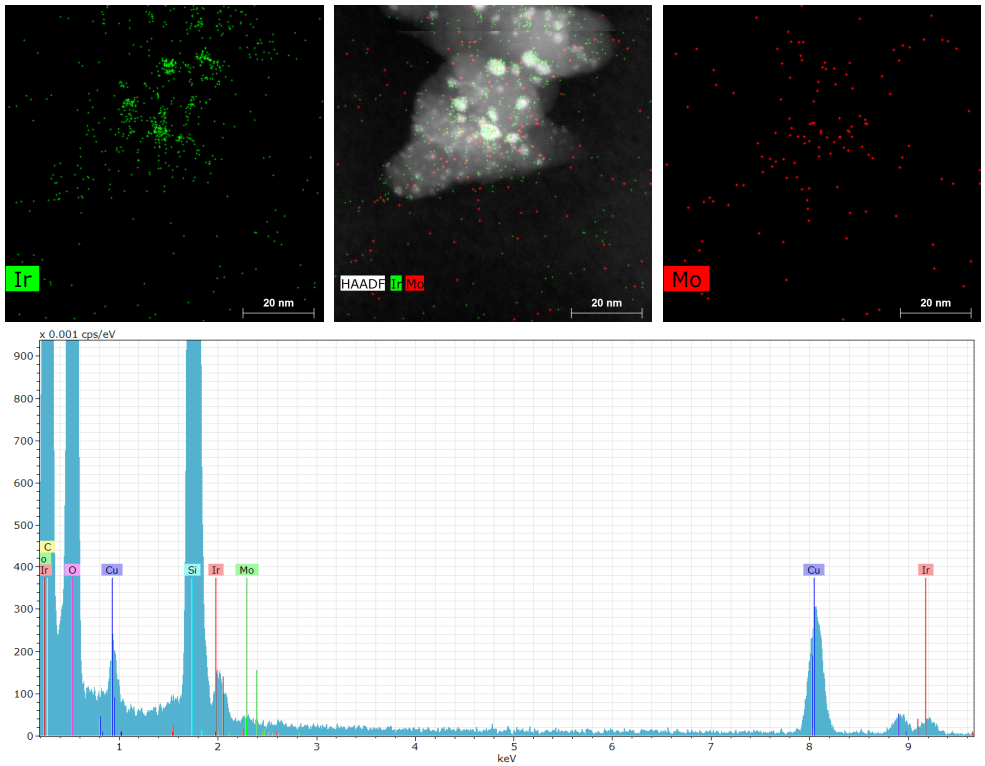

Figure S25. HAADF-STEM micrograph and EDX maps of Ir (green) and Mo (red) in fresh Ir-Mo/SiO_2 (top) and corresponding spectrum (bottom).

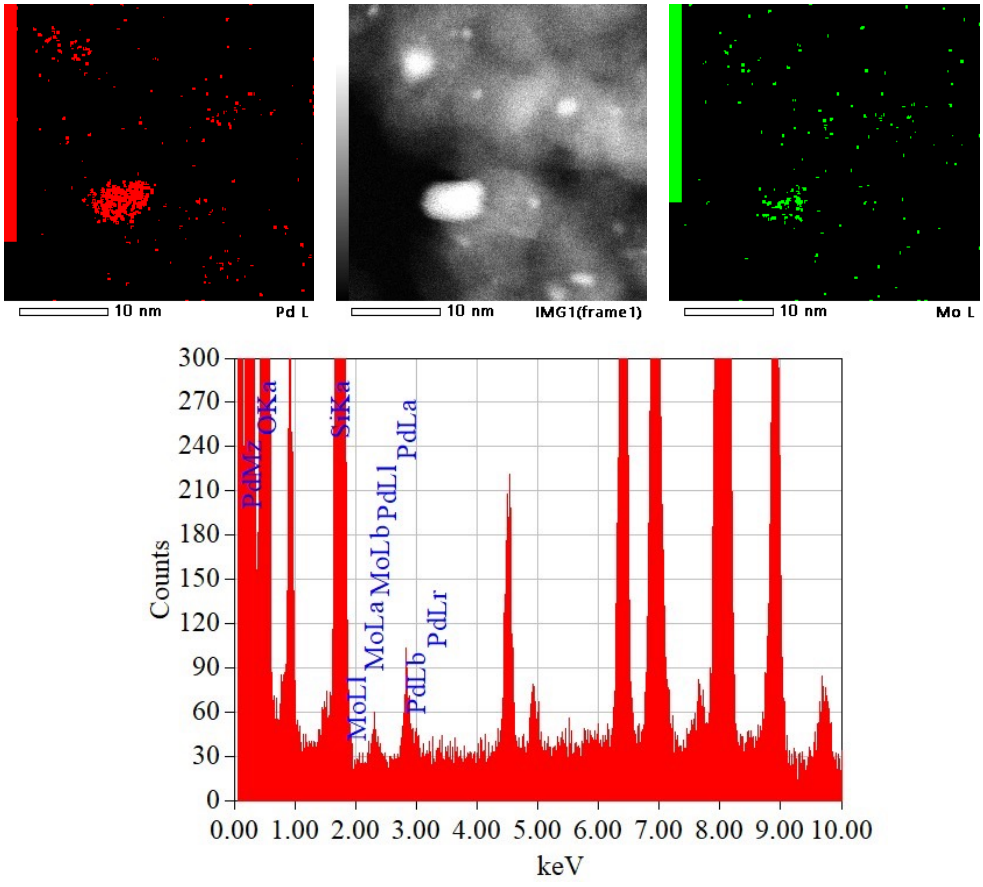

Figure S26. HAADF-STEM micrograph and EDX maps of Pd (red) and Mo (green) in spent Pd-Mo/SiO_2 (top) and corresponding spectrum (bottom).

6. CO-Chemisorption Measurements

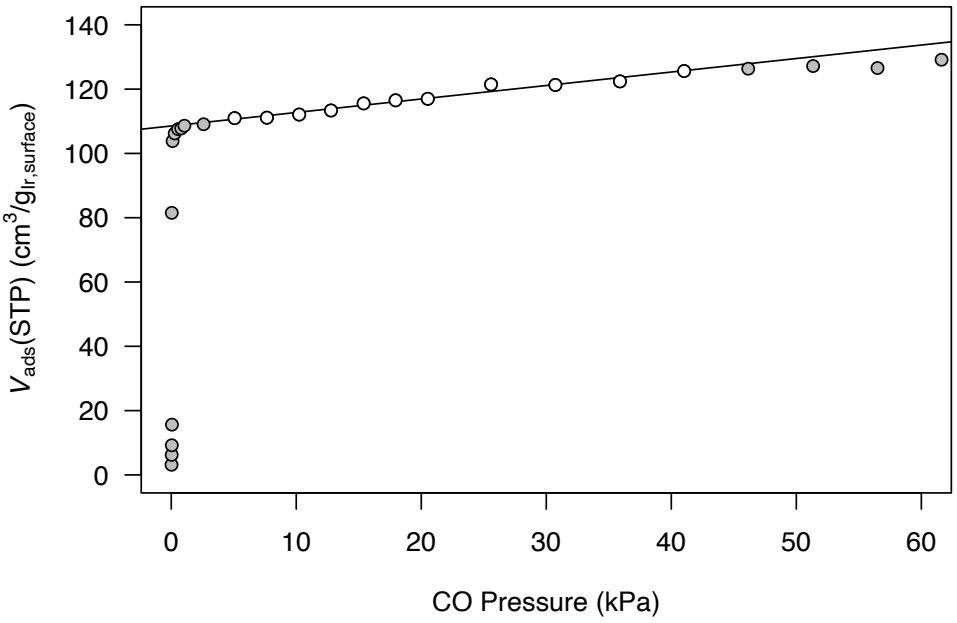

Figure S27. CO-uptake curve of Ir/SiO_2. The data was interpolated (R^2=0.97) between p=5 kPa and p=45 kPa (white data points) indicating an uptake of 109 cm^3 (STP)/$g_{Ir,Surface}$. The uptake data was normalized by the mass of Ir present on the surface of nanoparticles with a diameter of 2.9 nm (dispersion of 38%).

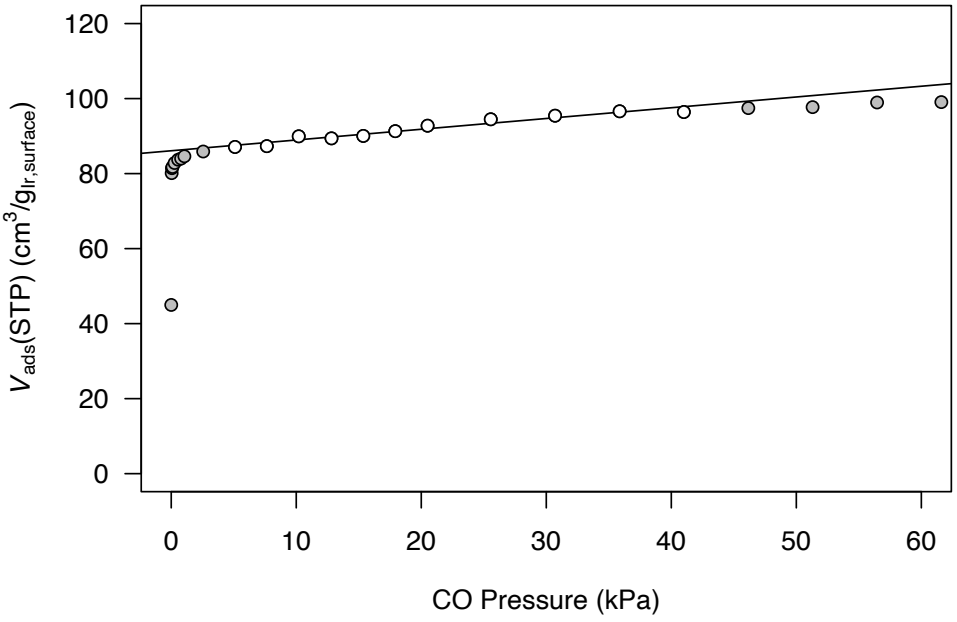

Figure S28. CO-uptake curve of $Ir\text{-}Mo/SiO_2$. The data was interpolated (R^2=0.95) between p=5 kPa and p=45 kPa (white data points) indicating an uptake of 86 cm^3 (STP)/$g_{Ir,Surface}$. The uptake data was normalized by the (expected) mass of Ir present on the surface of nanoparticles with a diameter of 2.0 nm (dispersion of 55%).

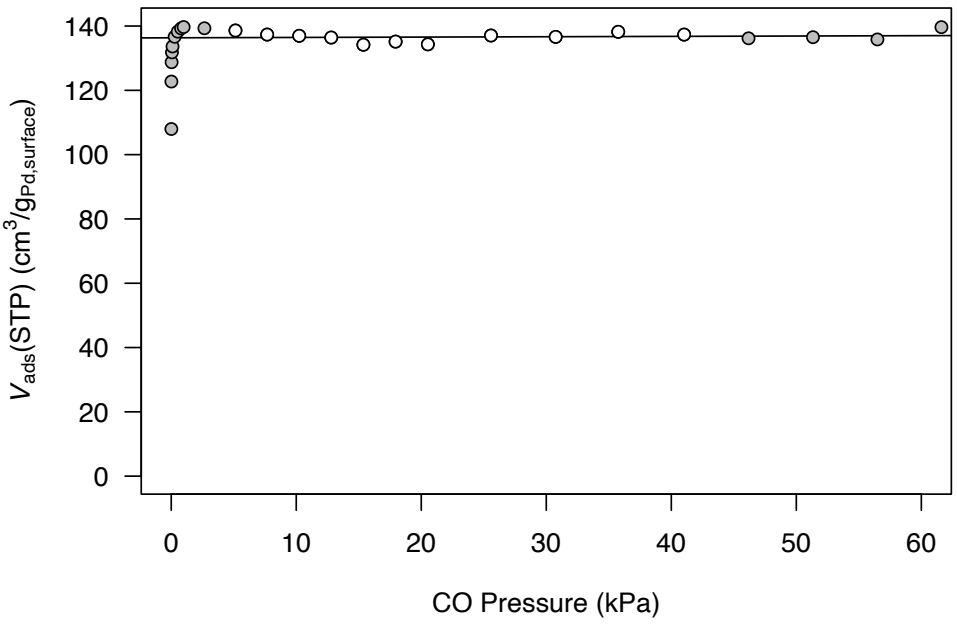

Figure S29. CO-uptake curve of Pd/SiO_2. The data was interpolated (R^2=0.01, due to V_{ads} being constant, corresponds to the average of points) between p=5 kPa and p=45 kPa (white data points) indicating an uptake of 136 cm^3 (STP)/$g_{Pd,Surface}$. The uptake data was normalized by the mass of Pd present on the surface of nanoparticles with a diameter of 3.1 nm (dispersion of 36%).

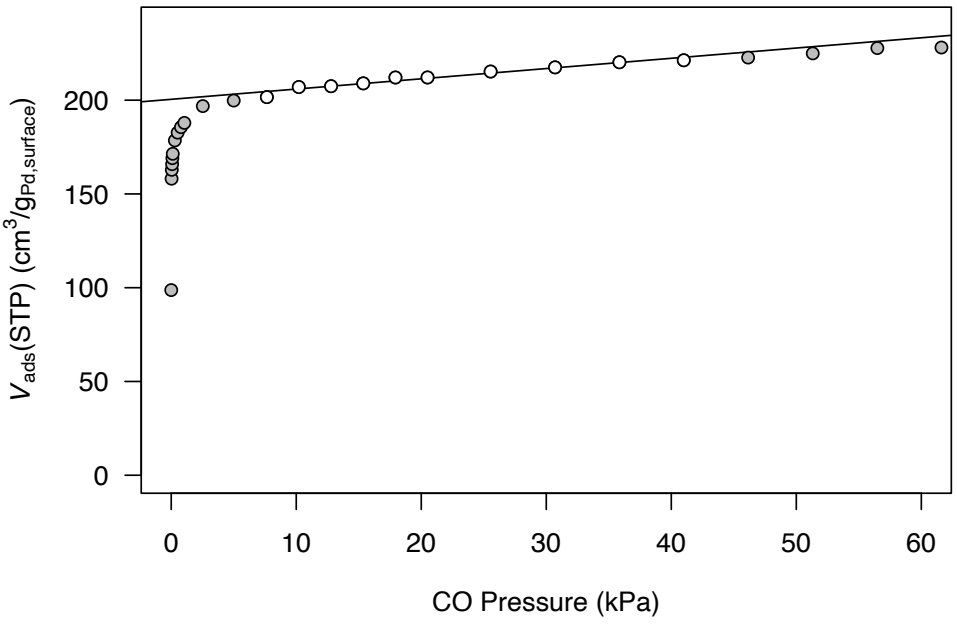

Figure S30. CO-uptake curve of $Pd\text{-}Mo/SiO_2$. The data was interpolated (R^2=0.95) between p=5 kPa and p=45 kPa (white data points) indicating an uptake of 200 cm^3 (STP)/$g_{Pd,Surface}$. The uptake data was normalized by the (expected) mass of Pd present on the surface of nanoparticles with a diameter of 2.5 nm (dispersion of 44%).

7. Pyridine Adsorption SS MAS NMR Spectroscopy

$IrMo/SiO_2$ (88 mg) was exposed to ^{15}N-pyridine saturation vapor at room temperature for 10 min. The excess physisorbed pyridine was removed by dynamic evacuation at 10^{-5} mbar for 1 h. Without air-exposure, the ^{15}N-pyridine adsorbed material was then transferred to an Ar-filled glovebox and packed in a 3.2 mm rotor. The low-temperature (100 K) solid-state $^{15}N\{^1H\}$ CP-MAS NMR spectrum was acquired on a Bruker Avance III 600 MHz (14.1 T) DNP NMR spectrometer equipped with a low-temperature 3.2 mm double-resonance MAS DNP probe operating at Larmor frequencies of 600.020 and 60.812MHz for ^1H and ^{15}N, respectively. CP-MAS ^{15}N NMR spectroscopy was measured at 101 K, with an MAS frequency of 8 kHz. The recycle delay was set at 8.5 s, with a contact time of 3 ms, measuring 10240 scans.
Only one species was observed with an isotropic chemical shift of 292 ppm, which matches well with H-bonded pyridine.[10, 11]

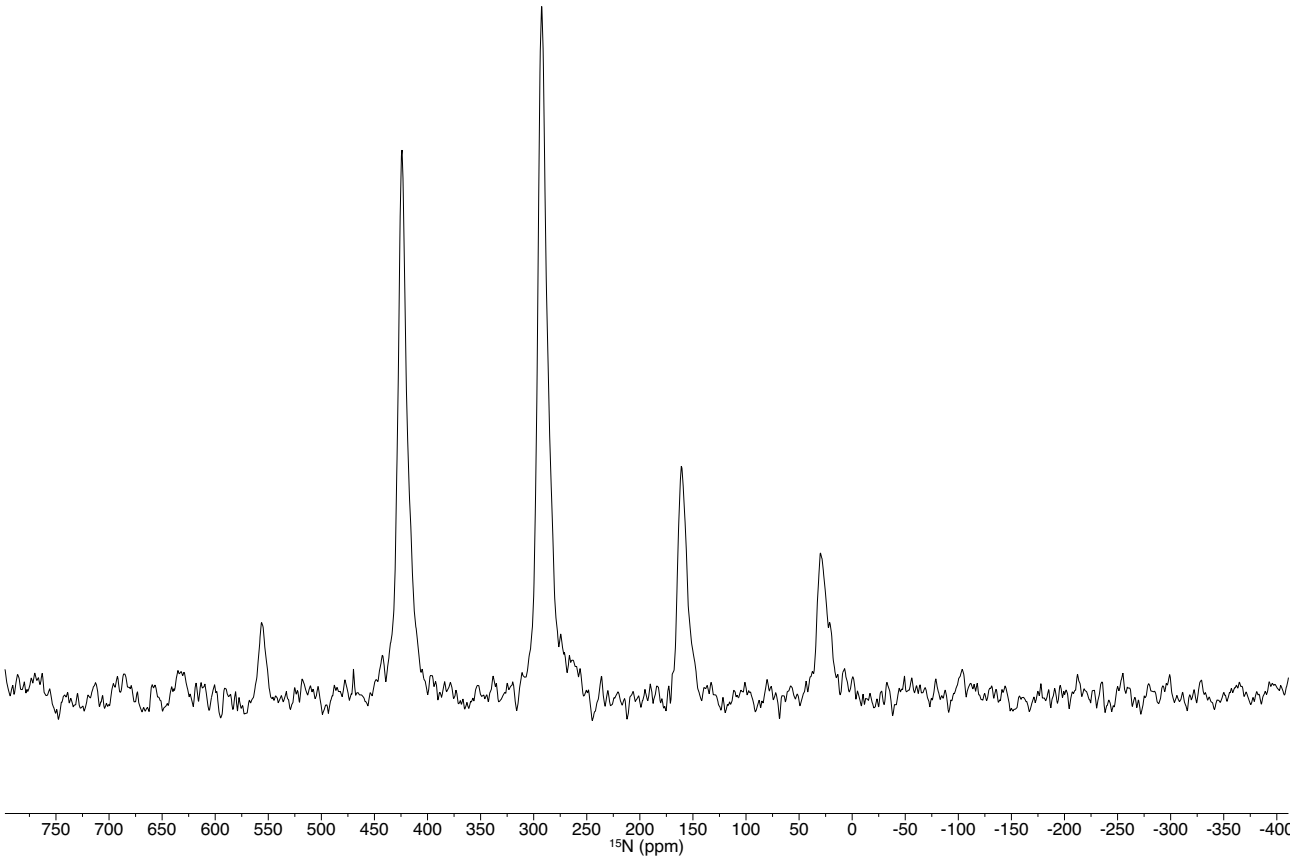

Figure S31. Low-temperature (100 K) solid-state $^{15}N\{^1H\}$ CP-MAS NMR spectrum of ^{15}N-pyridine adsorbed $IrMo/SiO_2$.

8. Catalysis

8.1 HDO High-Throughput Catalyst Evaluation

Catalytic evaluation was performed using a high-pressure parallel batch reactor from Integrated Lab Solutions (ILS) featuring 2x48 slots for septum sealed vials with 10 mL volume. Reaction vials were prepared in a nitrogen-filled glovebox. First, the catalyst material (20 mg, corresponds to ca. 5 µmol M and ca. 0.6 µmol Mo for bimetallic materials) and a stir bar were added to the vial, then a stock solution containing the respective alcohol (0.66 M) and tridecane (internal standard, 0.2 M) in decalin (1 mL, substrate to metal ratio ca. 130:1, and substrate to Mo ratio ca. 1:1000 for bimetallic materials) was added and the mixture was diluted with decalin (1 mL). The vials were closed with a viton®-lined septum inside the glovebox, then transferred to the reactor manifold, the septa were pierced and the reactor was closed under a positive flow of argon. The reactor containing the reaction vials was then pressurized with hydrogen to 10 bars and vented 3 times, before pressurizing to 20 bar (reaction pressure) and leak tested. Stirring (500 rpm) and heating (130 °C for 1-nonanol and 2,6-dimethyl heptanol, 160 °C for 2-nonanol) was initiated. After ca. 20 h, heating was stopped and the reactor was allowed to cool down to ca. 45 °C. The pressure was released and the reactor was flushed with Ar by pressurizing to 8 bar, and venting again 3 times. The vials were removed from the reactor manifold, and GC samples were prepared by taking 50 µL aliquots and diluting with 450 µL decalin. Yields and conversion were determined by GC/FID from external 5-point calibration curves using either a Shimadzu GCMS-QP2010 Ultra with an HP-5 column or an Agilent 7890A with an HP-5 column. Note that conversion of 2-nonanol could not be determined due to inseparable overlap of the starting material with one isomer of decalin.

For most reactions, the observed carbon balance revolves around ~90% for 1-nonanol and 2,6-dimethylhepan-2-ol, paralleling what has been observed for Ir-Mo/SiO_2 based catalysts for the deoxygenation of furanes.[12] This loss is likely a result of substrate decomposition (cracking) or could also be associated to strong adsorption of substrates/products to the catalyst surface.

8.2 Deoxygenation with MoO_x/SiO_2

The deoxygenation data of monometallic MoO_x/SiO_2 was performed in the same way. The observed yields and conversion are shown in **Figure S32**.

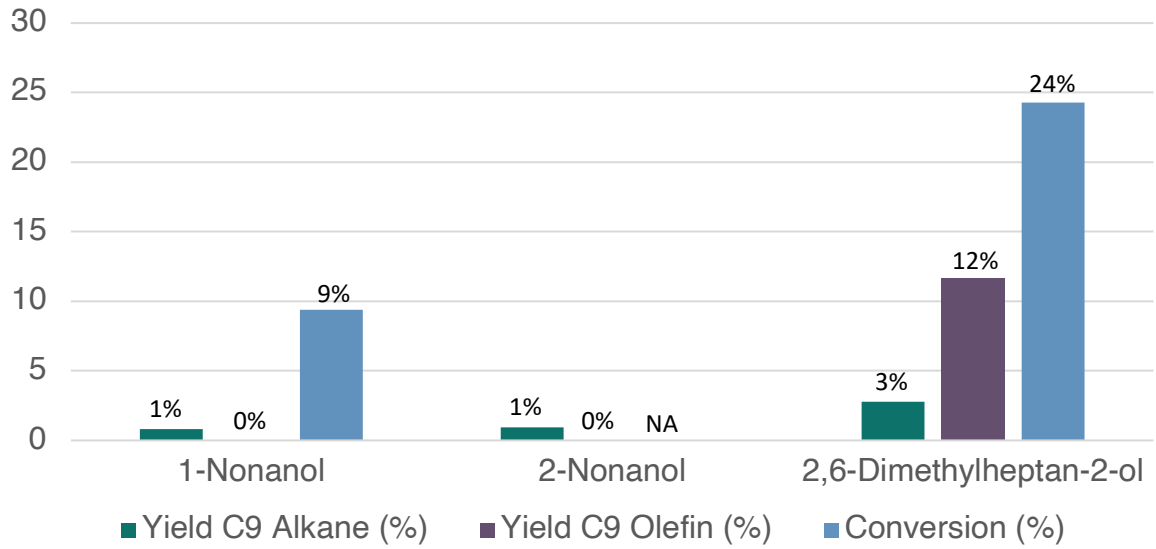

Figure S32. Observed product yields and conversion for the deoxygenation of 1-nonanol (product: n-nonane = C9 Alkane), 2-nonanol (product: n-nonane = C9 Alkane), and 2,6-dimethylheptanol (products: 2,6-dimethylheptane = C9 Alkane, and 1:1 mixture of 2,6-dimethylhept-1-ene and 2,6-dimethylhept-2-ene = C9 Olefin) with MoO_x/SiO_2.

8.3 Spent Catalysts

Due to location of the ILS reactor outside the glovebox, spent catalyst materials could not be prepared in the same way without exposure to air and moisture. For this, a digiCat96 reactor from the H.E.L. group was used, that was located in an Ar-filled glovebox. Reaction vials were prepared in the same way as above and after completion of the HDO conditions, the reaction solutions were decanted, the residue was washed with pentane (3 x 2 mL). The reaction vials were capped with a septum, pierced with a thick needle and transferred (with the needle still in place) to a Schlenk flask. The flask containing the vials was removed from the glovebox and evacuated at 10^{-5} mbar for 16 h. The flask was then reintroduced to the glovebox, and XAS samples were prepared for analysis (*vide infra*).

8.4 Reactions under Inert Conditions

The reactivity of 2,6-dimethylheptan-ol and 1-nonaol with Ir-Mo/SiO_2 as well as 2,6-dimethylheptan-ol with Ir/SiO_2 under inert atmosphere was evaluated using a high-pressure batch reactor from Premex AG according to the following procedure. In air, the respective alcohol (144 mg, 1 mmol, 1 equiv.) and n-tridecane (ca. 54 mg, 0.3 mmol, internal standard) were dissolved in decalin (3 mL) and added to the reactor. An aliquot of 50 µL was taken and diluted with decalin (450 µL) for later GC quantification (blank spectrum). The catalyt material (30 mg, ca. 7.5 µmol Ir, 0.75 mol-%) was added. The reactor was sealed under air, purged with Ar by pressurizing 6 times to 5 bar(g) and releasing the pressure, then pressurized to 5 bar(g). Stirring was initiated and heating (at 10 °C/min) to 130 °C (reaction temperature). After 20 h, heating was stopped, and the reactor was allowed to cool down. When it reached T < 40 °C (after ca. 3 h), the pressure was released and the reactor was opened. The solution was decanted and the reactor rinsed with decalin (2 x 1 mL). An aliquot of 75 µL of the combined washings was diluted with decalin (425 µL) for GC analysis. The results of GC-FID quantification are shown below.

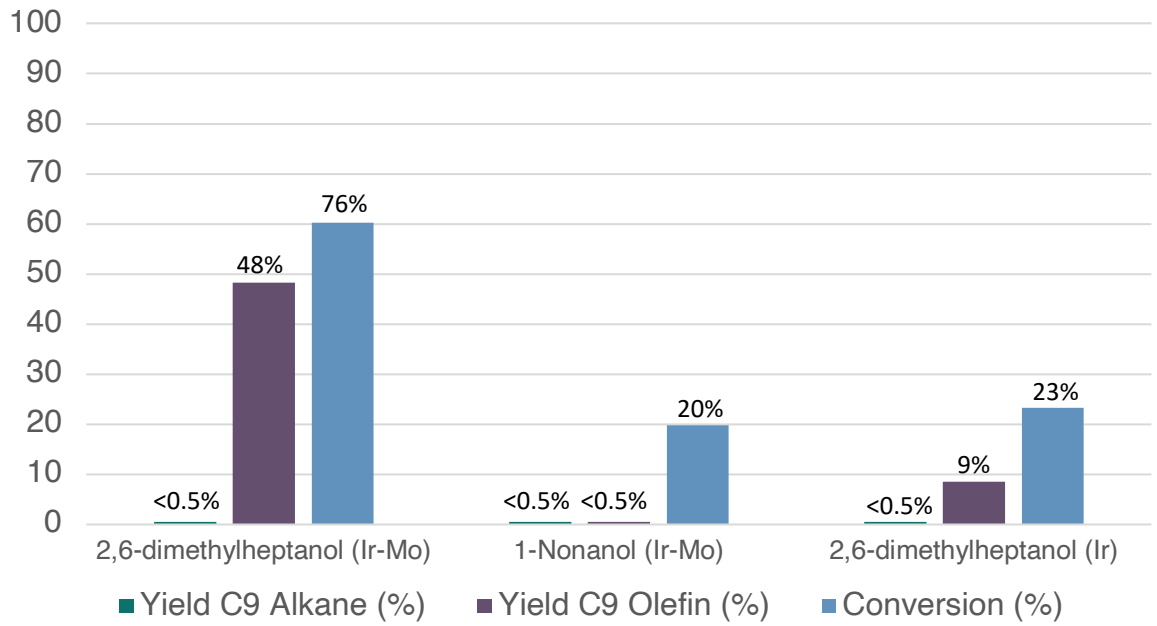

Figure S33. Observed product yields and conversion for the reaction of 2,6-dimethylheptanol (products: mixture of 2,6-dimethylhept-1-ene and 2,6-dimethylhept-2-ene = C9 Olefin) and 1-nonanol with Ir-Mo/SiO_2, and 2,6-dimethylheptanol with Ir/SiO_2. Conditions: 5 bar Ar, 130 °C, 20 h.

9. Competitive Deoxygenation of Tertiary over Primary Alcohols

Competitive deoxygenation of tertiary alcohols over primary alcohols was evaluated using a high-pressure batch reactor from Premex AG. Ir-Mo/SiO_2 as well as Pd-Mo/SiO_2 were investigated for the possibility of selectively deoxygenating tertiary over primary alcohols in a (1:1) mixture of 2,6-dimethylheptan-2-ol and 1-nonanol. Yields and conversion were determined by GC/FID from external 5-point calibration curves using an Agilent 7890A with an HP-5 column.

Ir-Mo/SiO_2: In air, 2,6-dimethylheptan-2-ol (99 mg, 0.69 mmol) and 1-nonanol (93 mg, 0.64 mmol) and n-tridecane (70 mg, 0.38 mmol, internal standard) were dissolved in decalin (4 mL) and added to the reactor. An aliquot of 50 µL was taken and diluted with decalin (450 µL) for later GC quantification (blank spectrum). Ir-Mo/SiO_2 (40 mg, ca. 0.01 mmol Ir, 0.75 mol-% w.r.t. to total alcohol amount) was added. The reactor was sealed under air, purged with Ar by pressurizing 4 times to 5 bar(g) and releasing the pressure, then purged with H_2 by pressurizing 3 times to 10 bar(g) and releasing the pressure, before pressurizing to 20 bar(g) with H_2 (reaction pressure). Stirring was initiated and heating (at 10 °C/min) to 130 °C (reaction temperature). After 15 h, heating was stopped, and the reactor was allowed to cool down. When it reached T < 40 °C (after ca. 3 h), the pressure was released, the reactor was purged with Ar (2 times 5 bar) and opened. The solution was decanted and the reactor rinsed with decalin (2 x 1 mL). An aliquot of 75 µL of the combined washings was diluted with decalin (425 µL) for GC analysis. Both substrates were deoxygenated, with the corresponding alkanes (2,6-dimethylheptane and n-nonane) being the only observed products. The observed yields and conversion data are shown in **Figure S34**.

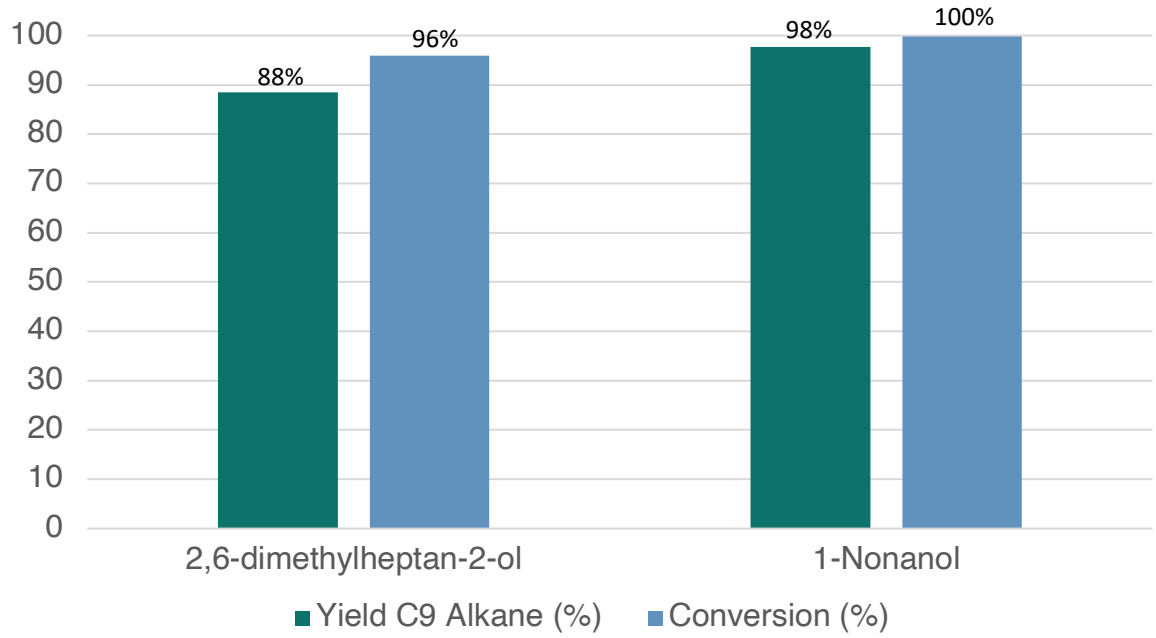

Figure S34. HDO yield and conversion of a 1:1 mixture of 2,6-dimethylheptan-2-ol (affording 2,6-dimethylheptane = C9 Alkane) and 1-nonanol (affording n-nonane = C9 alkane) with Ir-Mo/SiO_2.

Pd-Mo/SiO_2: In air, 2,6-dimethylheptan-2-ol (146 mg, 1.01 mmol) and 1-nonanol (149 mg, 1.04 mmol) and n-tridecane (58 mg, 0.31 mmol, internal standard) were dissolved in decalin (4 mL) and added to the reactor. An aliquot of 50 µL was taken and diluted with decalin (450 µL) for later GC quantification (blank spectrum). Pd-Mo/SiO_2 (60 mg, ca. 0.015 mmol Pd, 0.74 mol-% w.r.t. to total alcohol amount) was added. The reactor was sealed under air, purged with Ar by pressurizing 4 times to 5 bar(g) and releasing the pressure, then purged with H_2 by pressurizing 3 times to 10 bar(g) and releasing the pressure, before pressurizing to 20 bar(g) with H_2 (reaction pressure). Stirring was initiated and heating (at 10 °C/min) to 130 °C (reaction temperature). After 20 h, heating was stopped,

and the reactor was allowed to cool down. When it reached T < 40 °C (after ca. 3 h), the pressure was released, the reactor was purged with Ar (2 times 5 bar) and opened. The solution was decanted and the reactor rinsed with decalin (2 x 1 mL). An aliquot of 75 µL of the combined washings was diluted with decalin (425 µL) for GC analysis. Only 2,6-dimethylheptan-2-ol was deoxygenated, with the corresponding alkane being the only observed product. The conversion of 1-nonanol was 3%, with no deoxygenated product detected. The observed yield and conversion are shown in **Figure S35**.

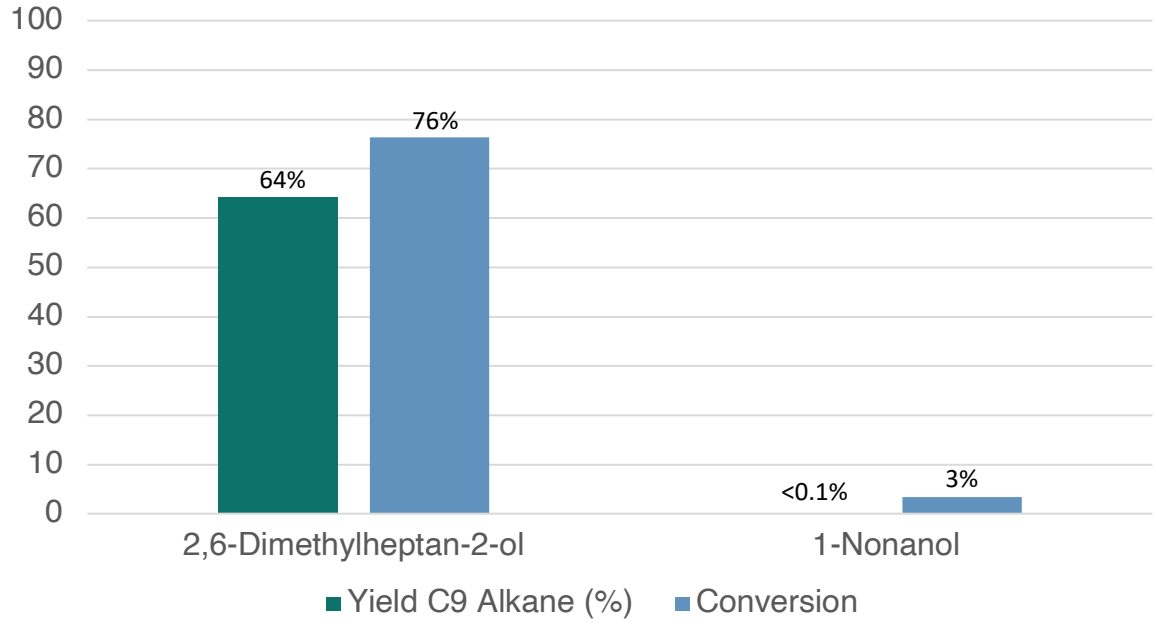

Figure S35. HDO yield and conversion of a 1:1 mixture of 2,6-dimethylheptan-2-ol (affording 2,6-dimethylheptane = C9 Alkane) and 1-nonanol (affording n-nonane = C9 alkane) with Pd-Mo/SiO_2.

10. Kinetic Profile of $IrMo/SiO_2$

The kinetic profile was evaluated using a high-pressure batch reactor from Premex AG. For every data point, the reactor was charged under air with a stock solution containing 1-nonanol (0.66 M) and tridecane (internal standard, 0.2 M) in decalin (1 mL) and was diluted with decalin (1 mL). $IrMo/SiO_2$ (20 mg, corresponds to a substrate to metal ratio of ca. 130:1) was added and the reactor was closed, flushed with Ar by pressurizing to 5 bar and releasing the pressure 3 times. Then flushed with H_2 by pressurizing to 10 bar and releasing the pressure 3 times, before pressurizing to 20 bar (reaction pressure). Overhead stirring was initiated and the heating (130 °C) was initiated. After 10 minutes, the temperature was reached which was marked as t = 0. The reaction was stopped after 1 h, 3 h, 8 h, 24 h, by removing the reactor from the heating block and placing it in an ice bucket. After reaching ca. 35 °C, the pressure was released and the reactor was flushed with Ar by pressurizing to 5 bar and releasing the pressure 3 times before opening the reactor and analyzing the reaction mixture by GC-FID against an external calibration curve using an Agilent 7890A with an HP-5 column.

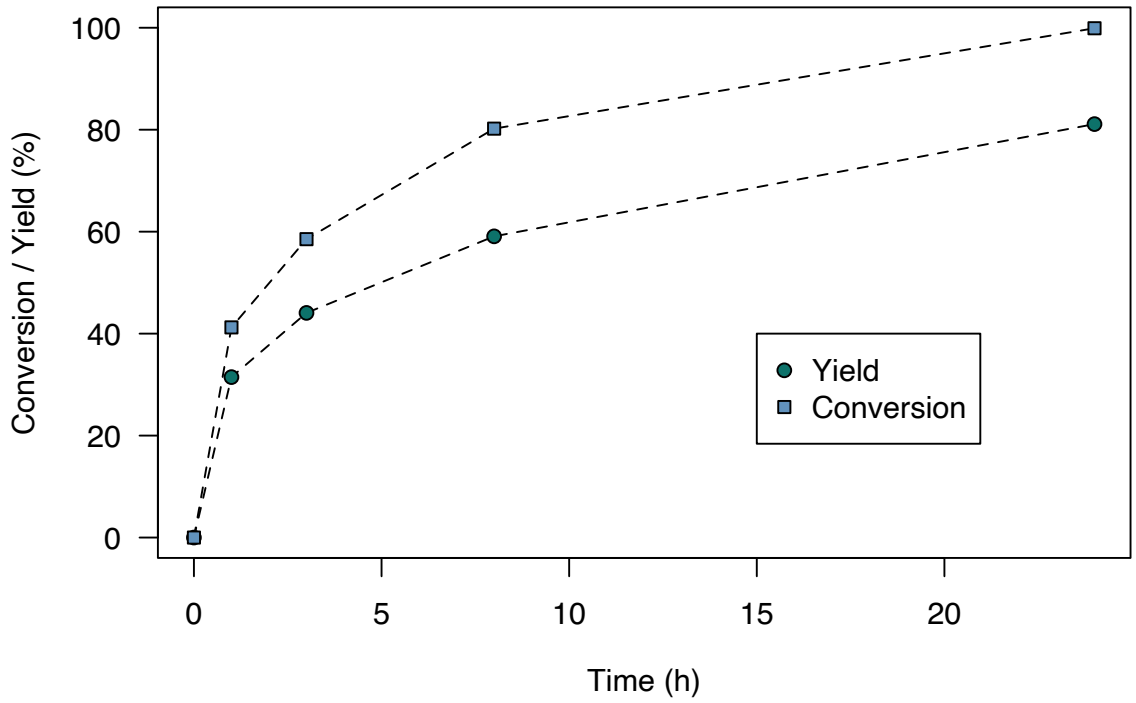

Figure S36. Yield of n-nonane and conversion of 1-nonanol in HDO with $IrMo/SiO_2$ after various reaction durations (1, 3, 8, 24 hours).

11. Recycling Study of $IrMo/SiO_2$

The recyclability of $IrMo/SiO_2$ was evaluated using a high-pressure batch reactor from Premex AG. The reactor was charged under air with a stock solution containing 1-nonanol (0.66 M) and tridecane (internal standard, 0.2 M) in decalin (4 mL) and was diluted with decalin (4 mL). $IrMo/SiO_2$ (80 mg, corresponds to a substrate to metal ratio of ca. 130:1) was added and the reactor was closed, flushed with Ar by pressurizing to 5 bar and releasing the pressure 3 times. Then flushed with H_2 by pressurizing to 10 bar and releasing the pressure 3 times, before pressurizing to 20 bar (reaction pressure). Overhead stirring was initiated and the heating (130 °C) was initiated and kept for 20 h, before it was allowed to cool down. After reaching ca. 35 °C, the pressure was released and the reactor was flushed with Ar by pressurizing to 5 bar and releasing the pressure 3 times before opening the reactor and analyzing the reaction mixture by GC-FID against an external calibration curve using an Agilent 7890A with an HP-5 column. The reaction mixture was decanted, and the residual material was rinsed with pentane (2 x 10 mL). The material was dried at 10^{-3} mbar for 1 h, weighed, and again transferred to the reactor. The subsequent cycles were conducted in the same way, ensuring a substrate to metal ratio of 130:1 considering the recovered catalyst mass.
After 5 cycles, the recovered material was subjected to a hydrogen treatment in flow at 400 °C for 12 h. This material displayed marginally increased activity (**Figure S37**, "Regen."). EA analysis of the spent material after 5 cycles and regeneration: Ir 3.57%, Mo 0.17%.

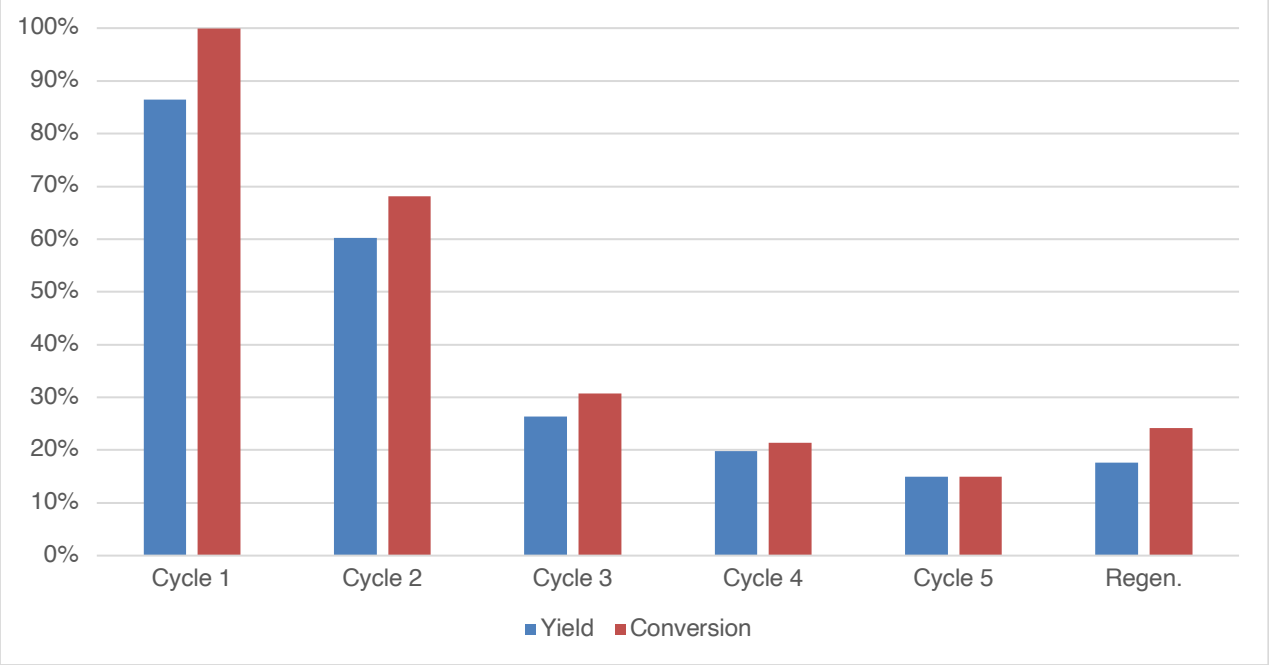

Figure S37. Recycling study of $IrMo/SiO_2$ in 1-nonanol HDO.

In a second attempt, the material isolated after 1 cycle (affording a yield of 87% and 100% conversion, Figure S26, "Cycle 1") a combined calcination/reduction procedure was applied (calcination at 500 °C for 6 h under a flow of synthetic air, then reduction at 500 °C for 6 h). However, this material exhibited inferior performance to the non-treated recovered material (see "Cycle 2" in **Figure S37**), affording a yield of 32% and conversion of 40% (not displayed).

12. X-Ray Absorption Spectroscopy

Quick-scanning extended x-ray absorption fine-structure spectroscopy (QEXAFS) was performed on the Ni, Rh, Pd, Mo K-edges, and the Pt and Ir L_3-edges. For QEXAFS measurements, the samples were placed in quartz capillaries (with a diameter of 1.5 mm and 0.01 mm wall thickness) under an inert gas atmosphere and sealed by vacuum grease and wax. Before capillary filling, the samples before the reaction were just ground. The after-reaction samples were separated from the reaction mixture, pre-dried on a Schlenk line, and finally dried by evaporation of the remaining solvent on a high vacuum line with a pressure between 10^{-5} to 10^{-6} mbar. All the steps were carried out without air exposure.

QEXAFS was performed at the SuperXAS beamline of the Swiss Light Source (SLS, Villigen, Switzerland),[13] which operates in top-up mode at 2.4 GeV and a ring current of 400 mA. The polychromatic X-rays from a 2.9 T superbend magnet were collimated by a silicon-coated mirror (for Ni K-edge), rhodium-coated mirror (Mo K-, Pt L_3-, and Ir L_3-edges), or platinum-coated mirror (for Rh, Pd, Mo K-edges) at 2.5 mrad, which also served to reduce higher-order harmonics. The collimated X-rays were monochromatized by a Si(111) channel-cut crystal. The monochromator was oscillating at a frequency of 1 Hz, resulting in two spectra per second. For the Ni K-, Mo K-, Pt L_3-, and Ir L_3-edges, a rhodium-coated toroidal mirror focused the beam on 300 x 1000 μm^2 spot on the sample. Other absorption edges were measured using a platinum-coated toroidal mirror focusing the beam on the same sample area. Ir L_3-edge XAS spectra were collected in transmission mode; other edges were measured in fluorescence mode. For transmission detection, we used three 15 cm long ionization chambers filled with 1 bar N_2 (for Ni K-edge), 1 bar N_2 + 1 bar Ar mixture (for Mo, Rh, and Pd K-edges), or 2 bar N_2 (for Pt and Ir L_3-edges). PIPS diode (Mirion Technologies) was used for fluorescence detection.[14] Reference foils of Ni (Ni K-edge), Pd(Rh K-edge, Pd K-edge), Pt (Ir L_3-edge, Pt L_3-edge), and Mo (Mo K-edge) were placed between the second and the third ionization chamber for simultaneous absolute energy calibration. For each sample, 600 spectra were taken over 5 minutes and averaged. Beam-induced spectral changes were not observed throughout the measurements. Spectra from the reference powders were taken from pellets containing reference compounds diluted with cellulose. XAS data background subtraction, normalization, interpolation, and averaging were done with the Python-based software ProQEXAFS Gui.[15] XANES analysis and fitting of the EXAFS region were performed with Athena and Artemis of the Demeter software.[16]

Linear combination fittings of XANES data

Linear combination fitting (LCF) of Mo K-edge XANES data were done using the Athena software. The fitting was performed from -20 eV to 30 eV with respect to the Mo K-edge energy. **Figure S38** compares the Mo K-edge XANES spectra of Mo/SiO_2 catalyst in the as-prepared (green) and post-reaction (orange) states with the crystalline references of MoO_2 (dashed red), MoO_3 (dashed purple), and Mo foil (dashed blue). Considering strong similarity of the Mo K-edge positions of the as-prepared state of Mo/SiO_2 to MoO_3 and post-reaction state of Mo/SiO_2 to MoO_2, the spectra of highly-dispersed Mo in Mo/SiO_2 were used for LCF as references representing Mo(VI) and Mo(IV) states in all supported bimetallic compositions. Mo foil spectrum was utilized to fit Mo(0) state.

EXAFS fitting

EXAFS fitting was performed in R-space. k-range, R-range, k-weighting, and amplitude reduction factors (So^2) are summarized in Table S2. EXAFS fitting of reference metal foils determined the amplitude reduction factors. Metal foils of Rh and Ir were not available. For them, the S_0^2 was extrapolated from the Pd and Pt foil fits, since similar value can be expected based on the neighboring atomic numbers. To fit Rh K-, Pd K-, Ir L_3- and Pt L_3-edge EXAFS data, we used only Rh-Rh, Pd-Pd, Ir-Ir, and Pt-Pt paths. Due to low Mo loading of bimetallic compositions (M:Mo = 8:1), M-Mo bond could not be reliably detected. M-O bonds were also not detected for all the catalysts studied at Rh K-, Pd K-, Ir L_3-, and Pt L_3-edges. A Mo-O and Mo-M path were used to fit Mo K-edge data. To obtain the Mo-M paths (M=Rh, Pd, Ir, and Pt), we used the standard crystal structures of Rh, Pd, Ir, and Pt and generated Mo-M path by replacing the central atom by Mo. For bimetallic compositions,

the EXAFS data at both absorption edges were fitted simultaneously, keeping the same Debye-Waller factors for M-M and Mo-M bonds. The fitting results are shown in **Figure S59**–**Figure S83** and **Table S2**–**Table S18**.

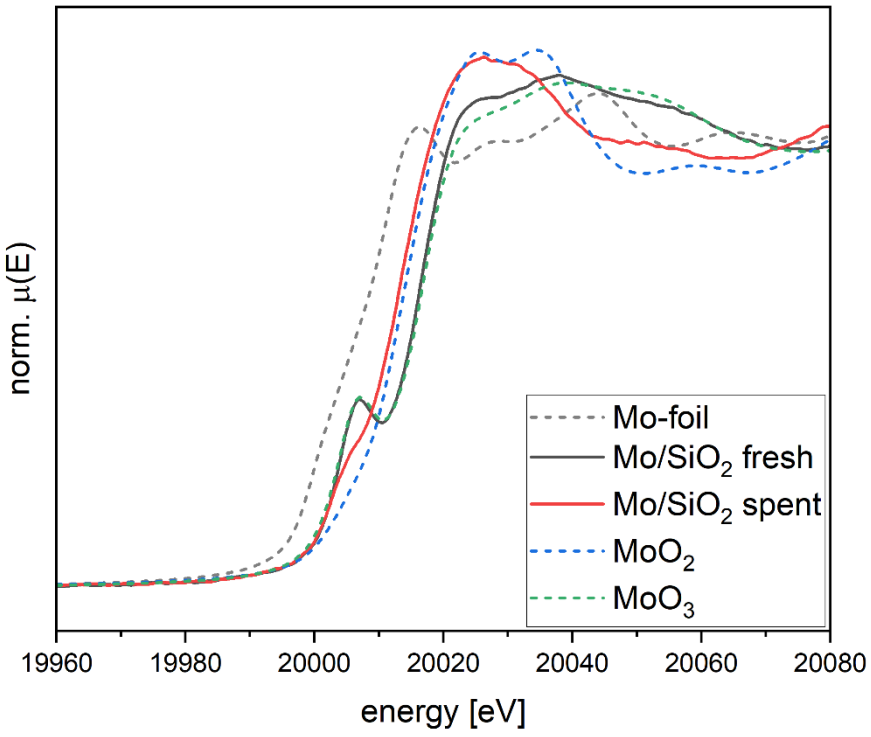

Figure S38. Mo K-edge XANES spectra of reference compounds including Mo foil, MoO_2, MoO_3, as-prepared (black) and post-reaction states (red) of MoO_3/SiO_2.

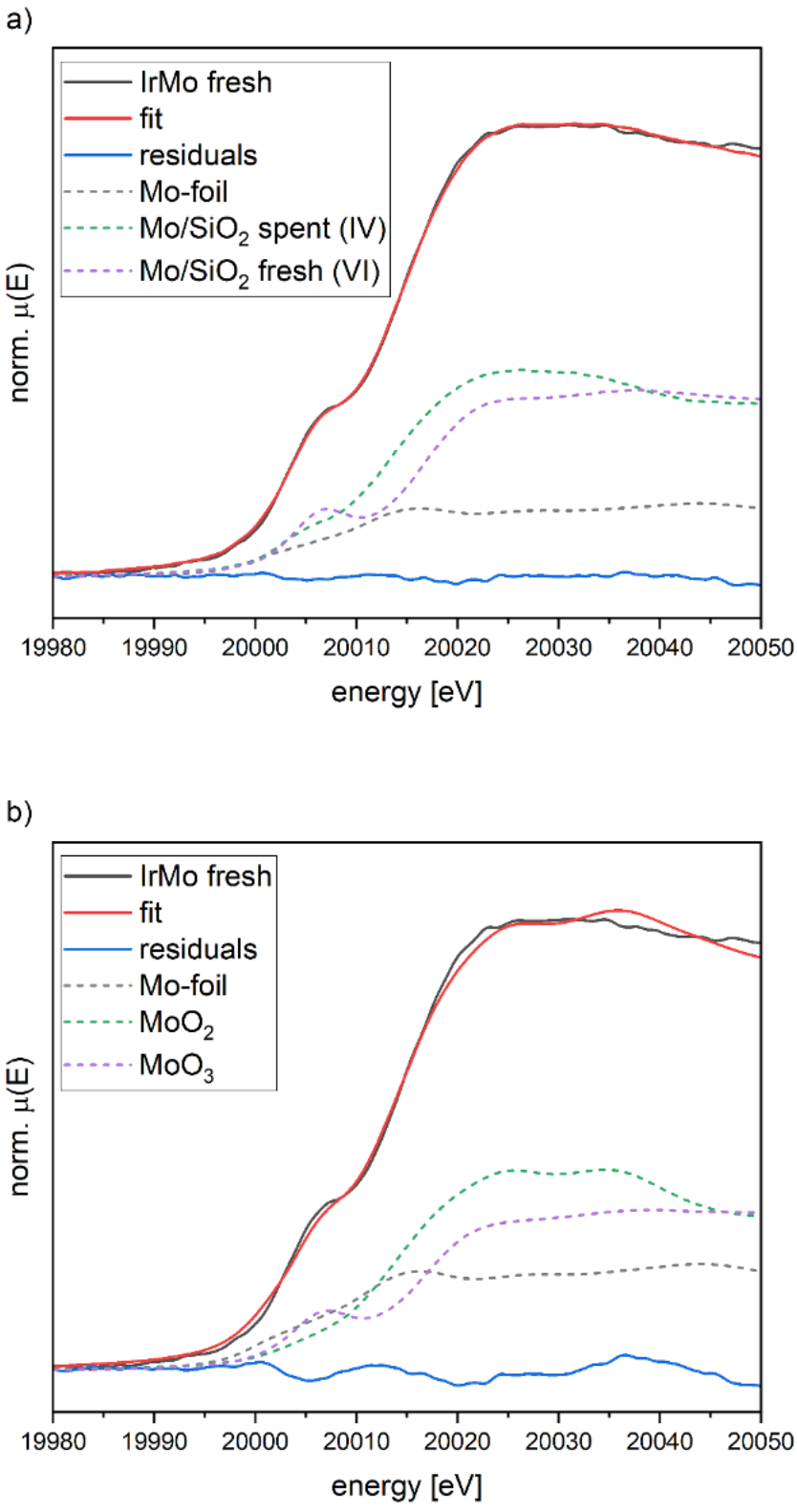

Figure S39. LCF comparison of a) monometallic MoO_3/SiO_2 materials before and after HDO reaction (R-factor: 0.0004) and b) metal oxide references (R-factor: 0.0029).

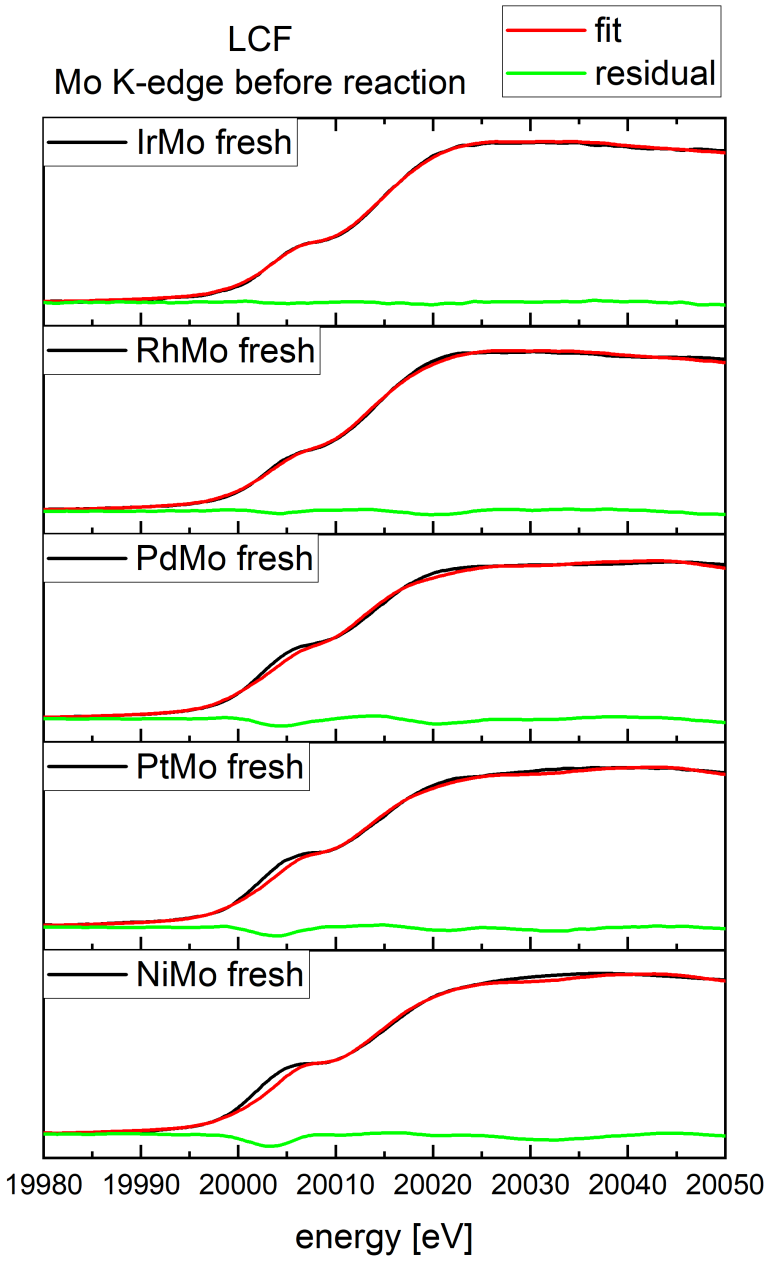

Figure S40. Mo K-edge XANES LCF results with residuals for the bi-metallic IrMo/SiO_2, RhMo/SiO_2, PdMo/SiO_2, PtMo/SiO_2 and NiMo/SiO_2 materials before the HDO reaction.

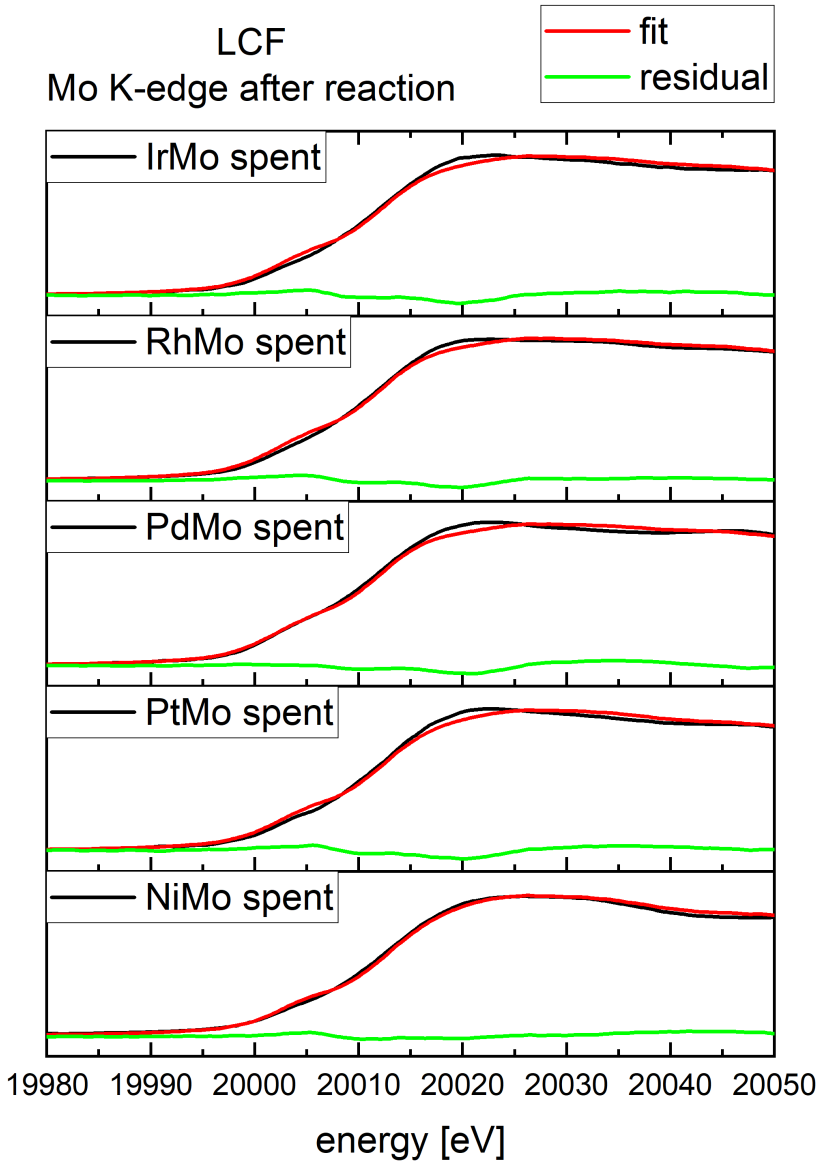

Figure S41. Mo K-edge XANES LCF results with residuals for the bi-metallic IrMo/SiO_2, RhMo/SiO_2, PdMo/SiO_2, PtMo/SiO_2 and NiMo/SiO_2 materials after the HDO reaction.

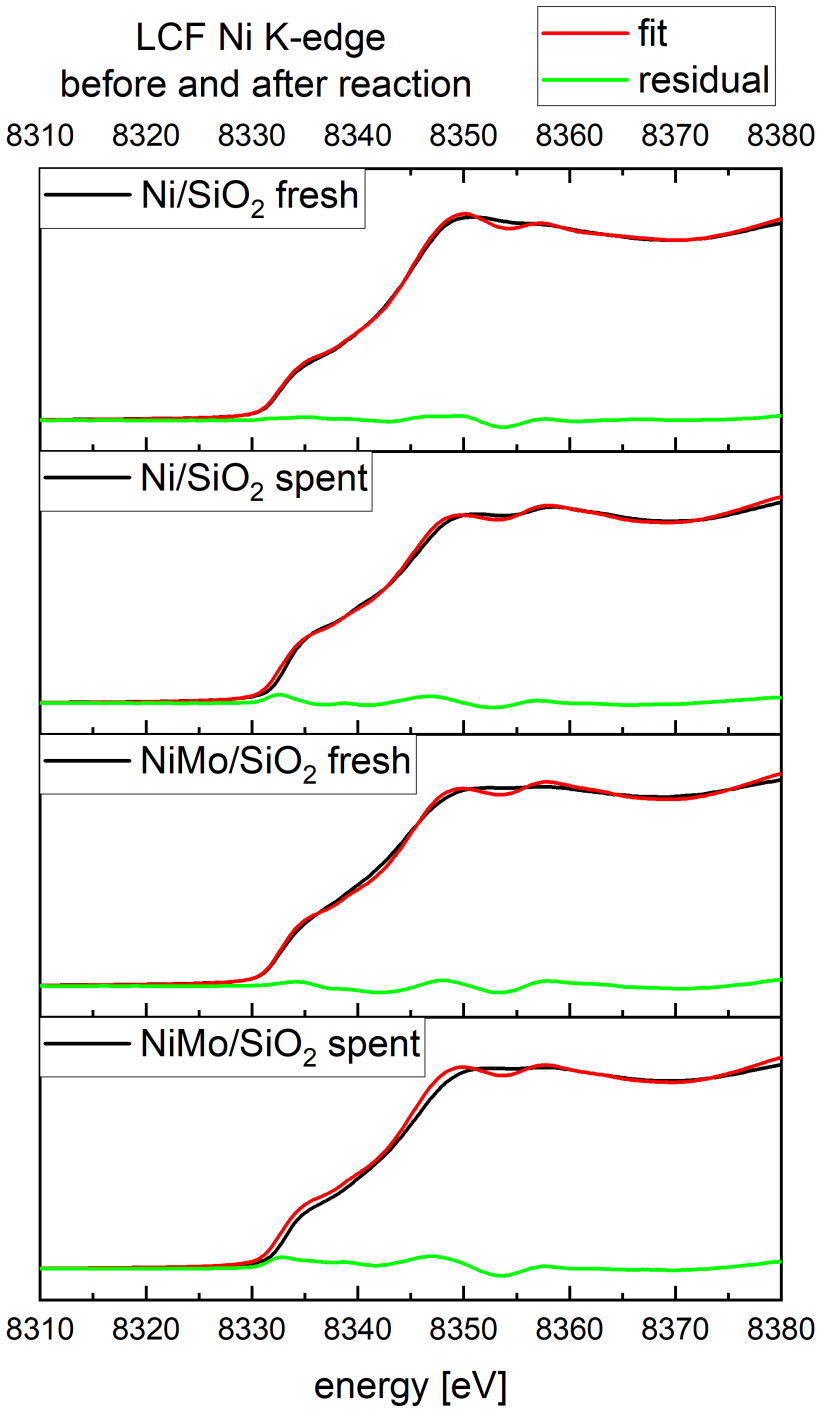

Figure S42. Ni K-edge XANES LCF results with residuals for the Ni/SiO_2 and $NiMo/SiO_2$ materials before and after the HDO reaction.

Table S1. Results of LCF of the Ni K-edge spectra of the mono- and bi-metallic Ni materials before and after reaction.

Material	**Ni (%)**	**NiO (%)**
Ni/SiO_2 fresh	88	12
Ni/SiO_2 spent	100	0
NiMo/SiO_2 fresh	98	2
NiMo/SiO_2 spent	95	5

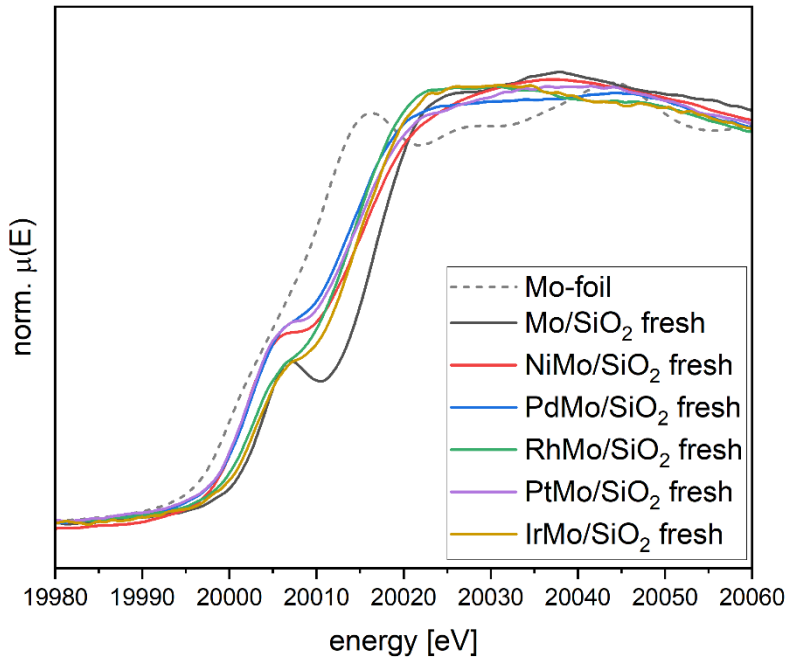

Figure S43. Mo K-edge XANES spectra of the materials before the HDO reaction.

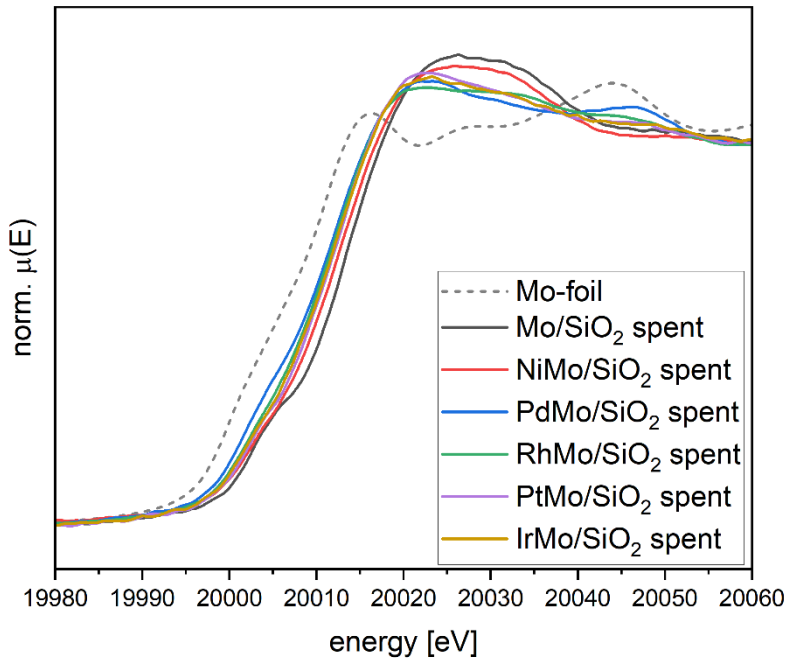

Figure S44. Mo K-edge XANES spectra of the materials after the HDO reaction.

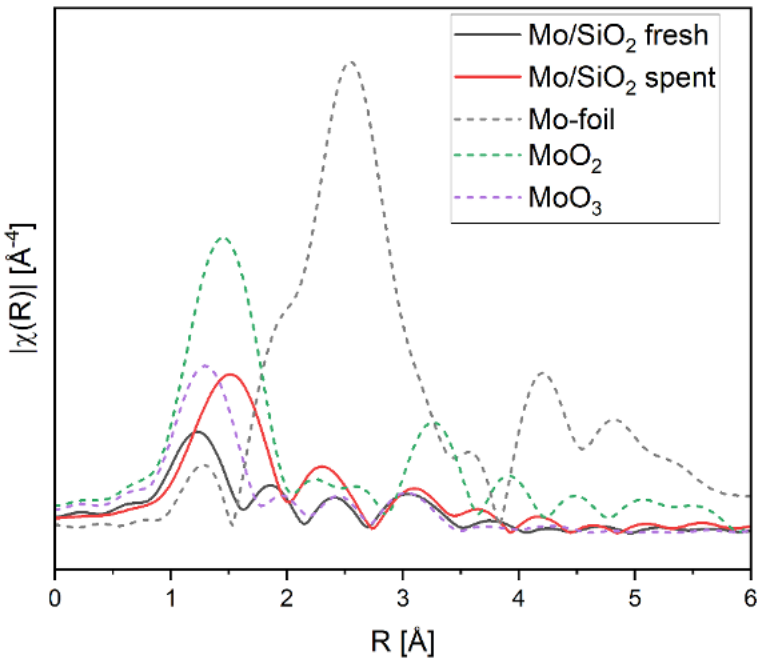

Figure S45. Mo K-edge R-space of Mo/SiO_2 before and after HDO reaction together with Mo reference foil and oxide references.

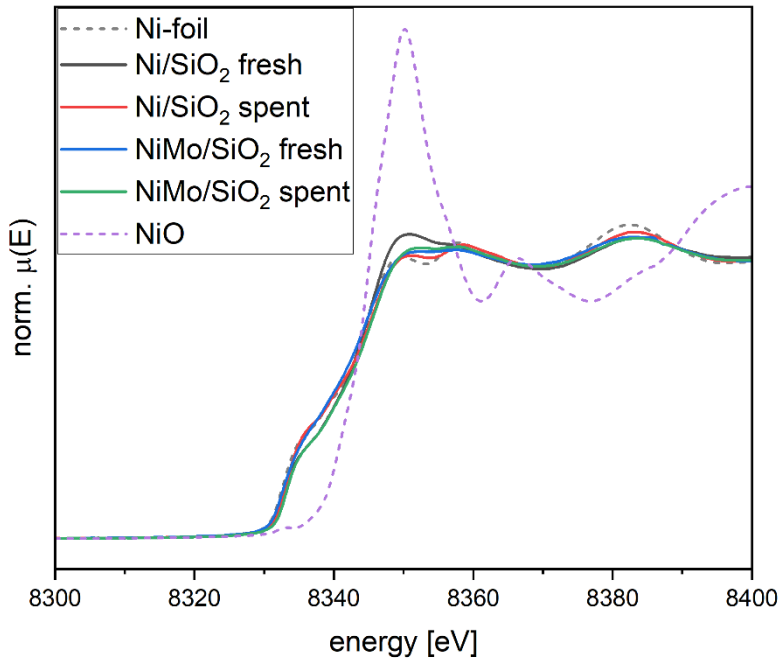

Figure S46. Ni K-edge XANES spectra of the Ni/SiO_2 and $NiMo/SiO_2$ materials before and after HDO reaction together, with Ni foil and NiO references.

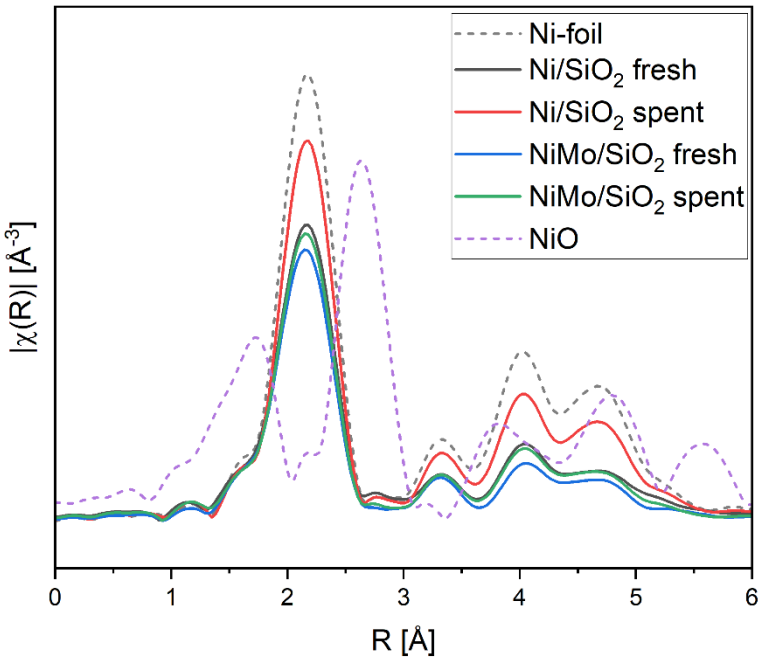

Figure S47. Ni K-edge R-spaces of the Ni/SiO_2 and $NiMo/SiO_2$ materials before and after reaction together with Ni foil and NiO references.

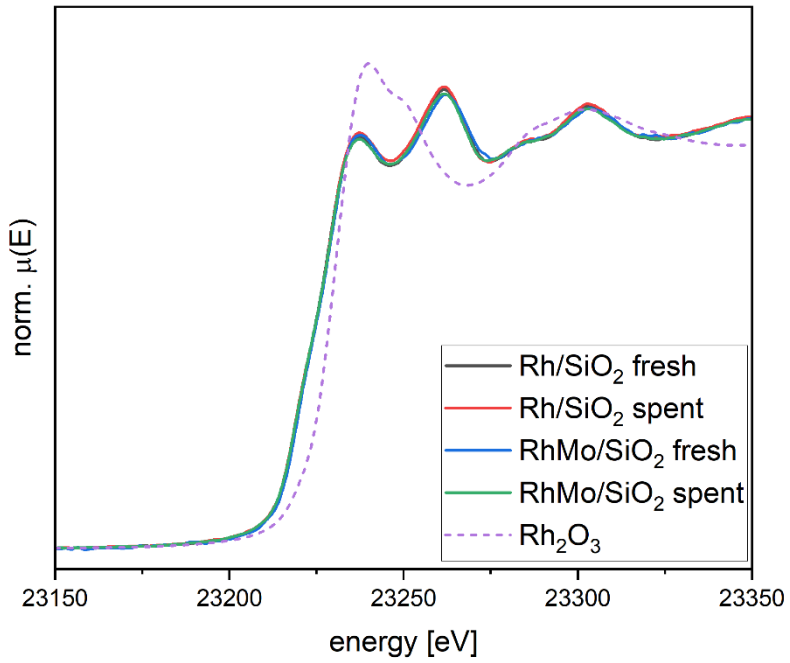

Figure S48. Rh K-edge XANES spectra of Rh/SiO_2 and $RhMo/SiO_2$ materials before and after HDO reaction.

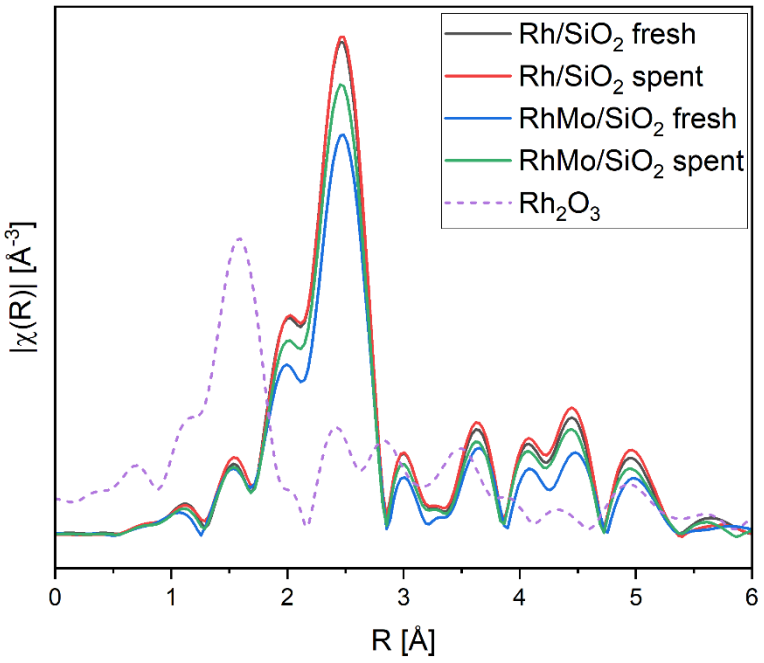

Figure S49. Rh K-edge R-space of Rh/SiO_2 and $RhMo/SiO_2$ materials before and after the HDO reaction with Rh_2O_3 reference.

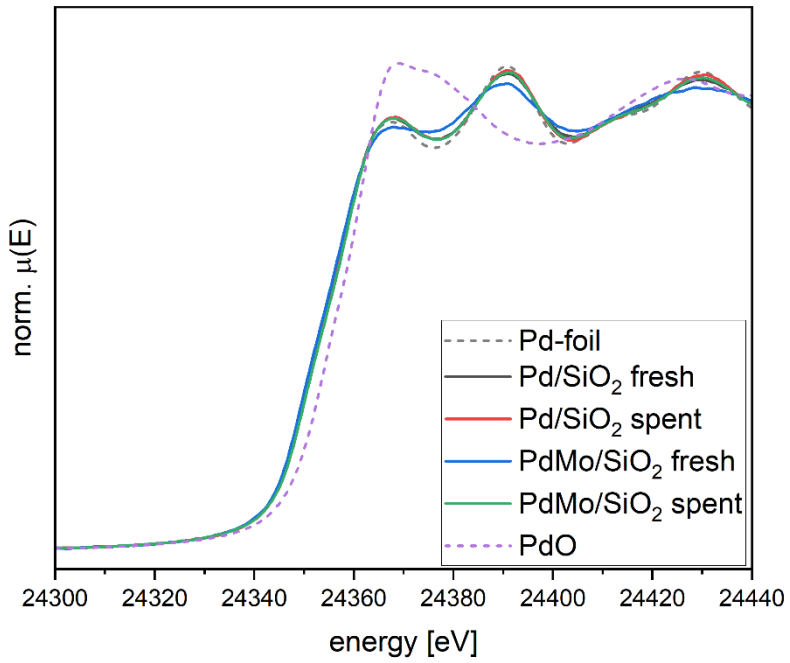

Figure S50. Pd K-edge spectra of the Pd/SiO_2 and $PdMo/SiO_2$ materials before and after the HDO reaction together with Pd foil and PdO references.

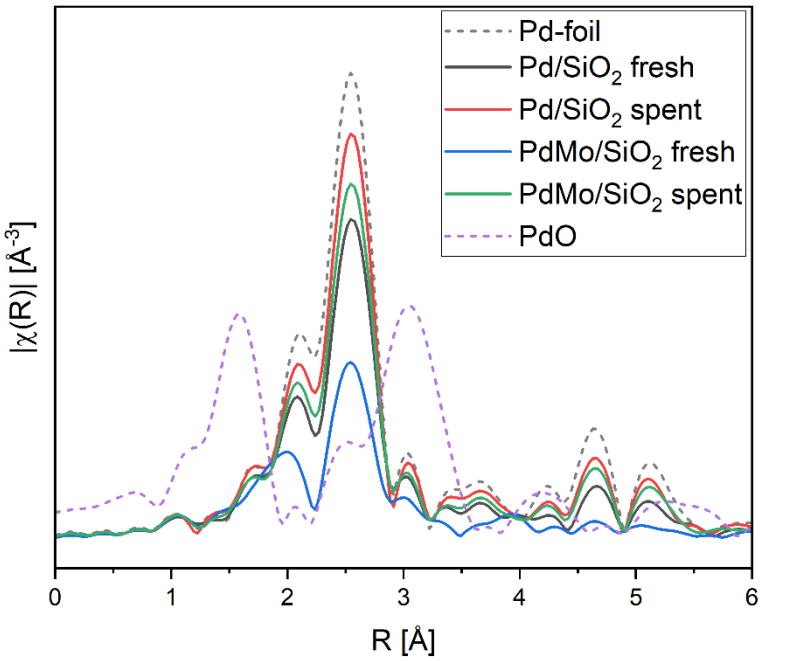

Figure S51. Pd K-edge R-space of the Pd/SiO_2 and $PdMo/SiO_2$ materials before and after HDO reaction together with Pd foil and PdO references.

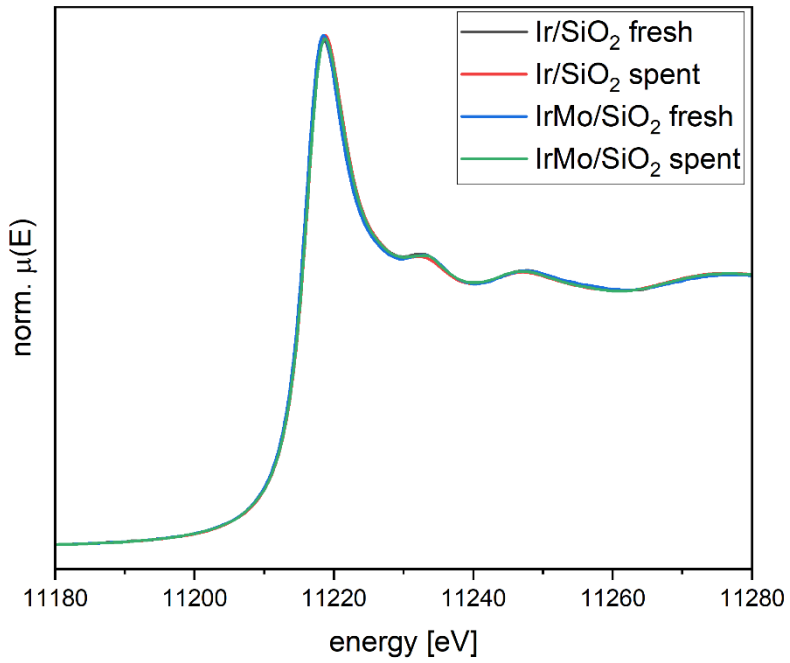

Figure S52. Ir L_3-edge XANES spectra of the Ir/SiO_2 and $IrMo/SiO_2$ materials before and after HDO reaction.

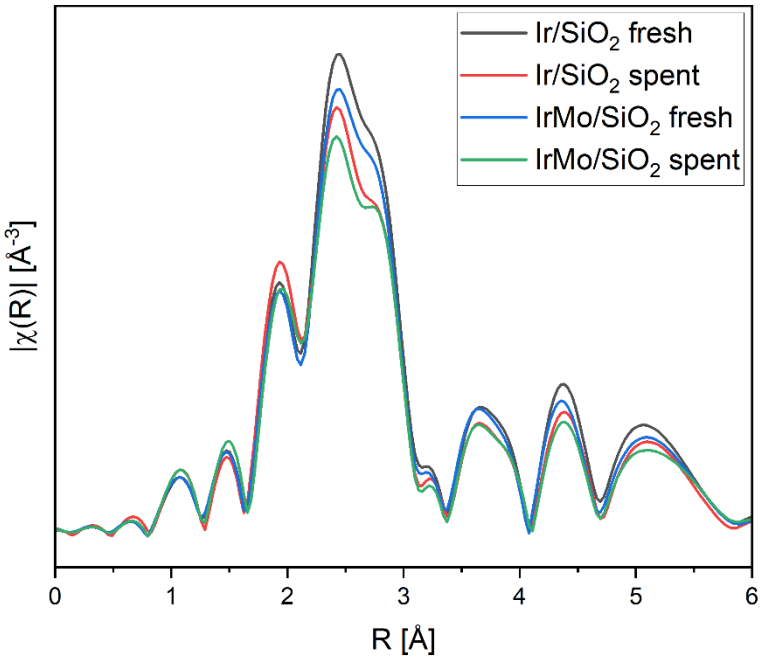

Figure S53. Ir L_3-edge R-space of Ir/SiO_2 and $IrMo/SiO_2$ catalyst before and after the HDO reaction.

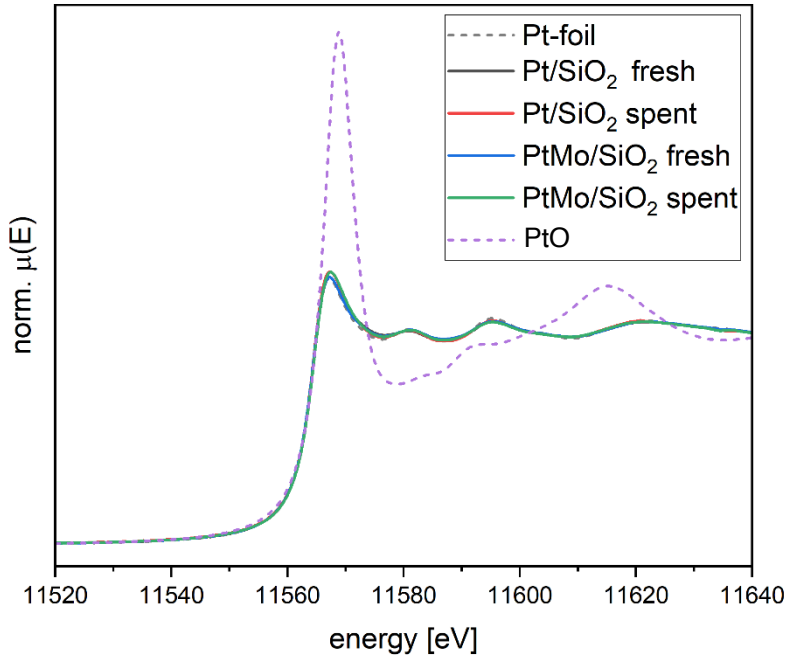

Figure S54. Pt L_3-edge XANES spectra of the Pt/SiO_2 and $PtMo/SiO_2$ materials before and after the HDO reaction together with the Pt foil reference.

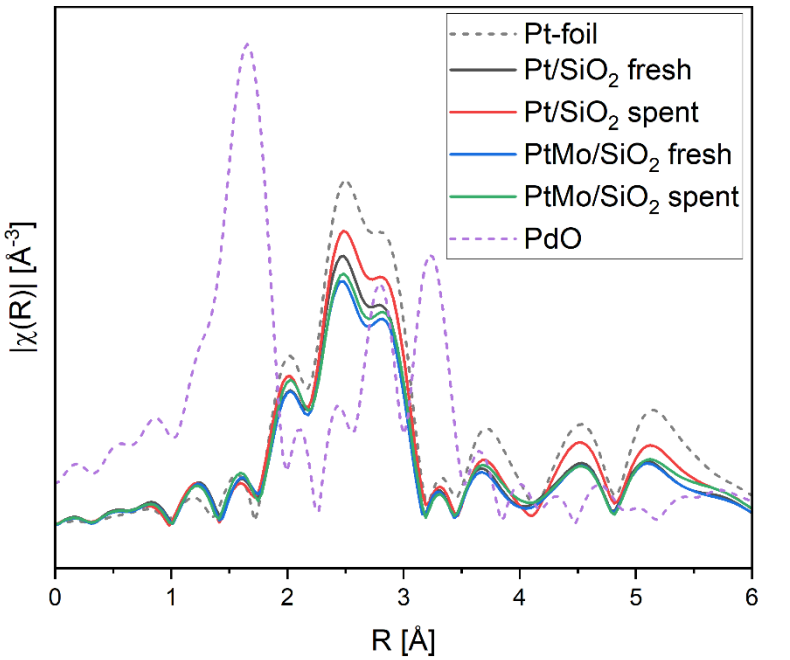

Figure S55. Pt L_3-edge R-space of the Pt/SiO_2 and $PtMo/SiO_2$ materials before and after HDO reaction together with the Pt foil reference.

Table S2. EXAFS fitting procedures' K-range, R-range, and amplitude reduction factor.

Absorption edge	K-range, $Å^{-1}$	R-range, Å	S_0^2	K-weight
Mo K	3-10. 8	1-3.5	0.79	3
Rh K	3-16.6	1-3.5	0.78 (Pd-foil)	3
Pd K	3-16.0	1-3.5	0.78	3
Ir L_3	3-16.6	1-3.5	0.82 (Pt-foil)	3
Pt L_3	3-15.8	1-3.5	0.82	3
Ni K	3-12	1-3.5	0.79	3

Sample: Ir/SiO_2 before reaction.

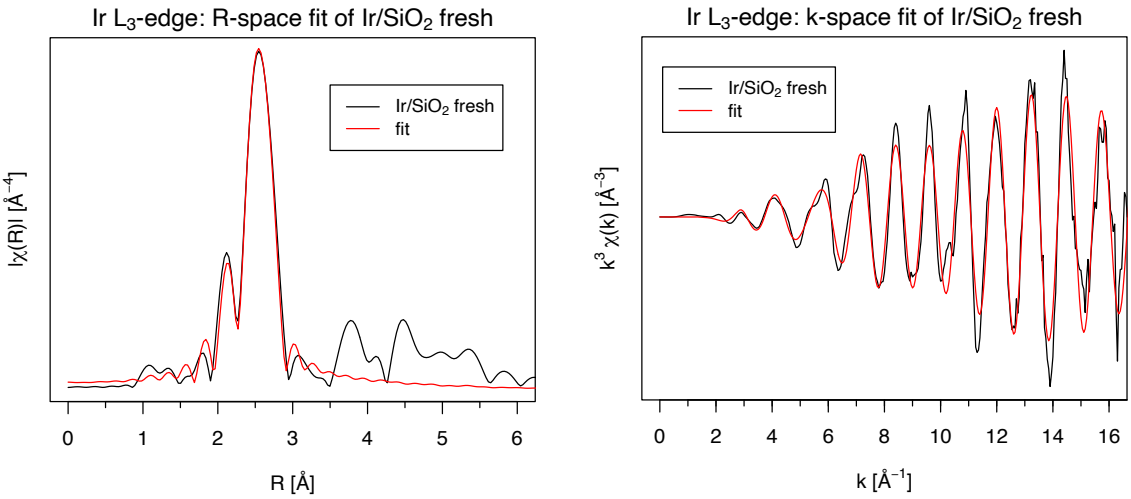

Figure S56. R-space and k-space EXAFS fit of the Ir L_3-edge data of Ir/SiO_2 before HDO reaction.

Table S3. EXAFS fitting results of Ir/SiO_2 before the HDO reaction.

Coordination shell	**N**	**σ^2, $Å^2$**	**R, Å**	**Reff, Å**	**ΔE_0, eV**	**Rf**
Ir L_3-edge						
Ir-Ir	10.6±0.7	0.0044±0.0003	2.691±0.003	2.691	7.1±0.7	0.0234

Sample: Ir/SiO_2 after reaction.

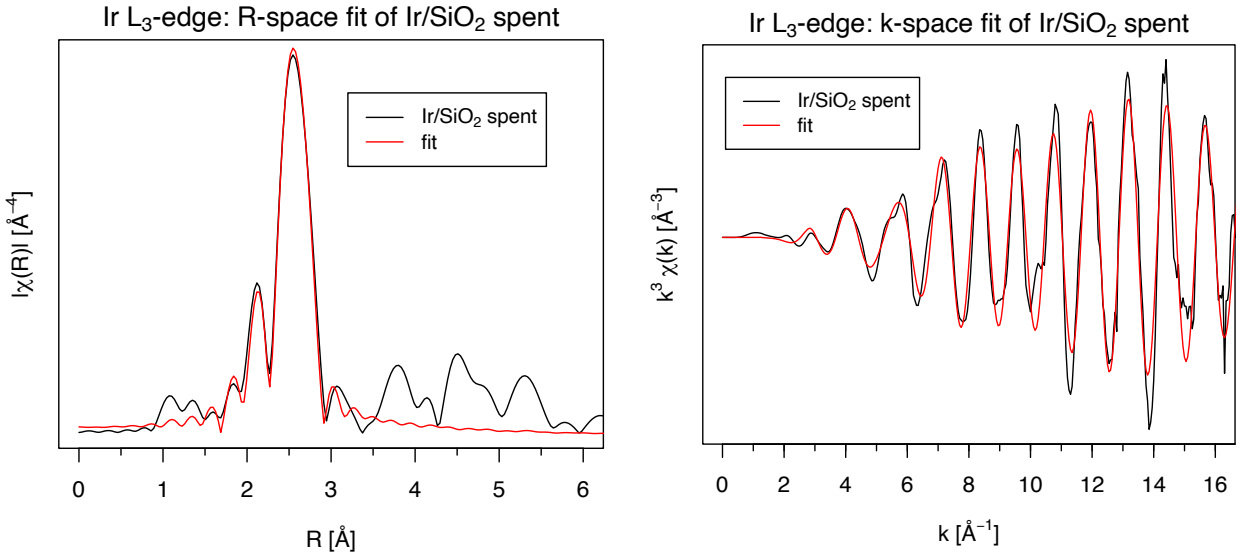

Figure S57. R-space and k-space EXAFS fit of the Ir L_3-edge data of Ir/SiO_2 after HDO reaction.

Table S4. EXAFS fitting results of Ir/SiO_2 after the HDO reaction.

Coordination shell	**N**	**σ^2, Å^2**	**R, Å**	**Reff, Å**	**ΔE_0, eV**	**Rf**
Ir L_3-edge						
Ir-Ir	10.8±0.7	0.0049±0.0003	2.699±0.003	2.691	6.2±0.6	0.0203

Sample IrMo/SiO_2 before reaction.

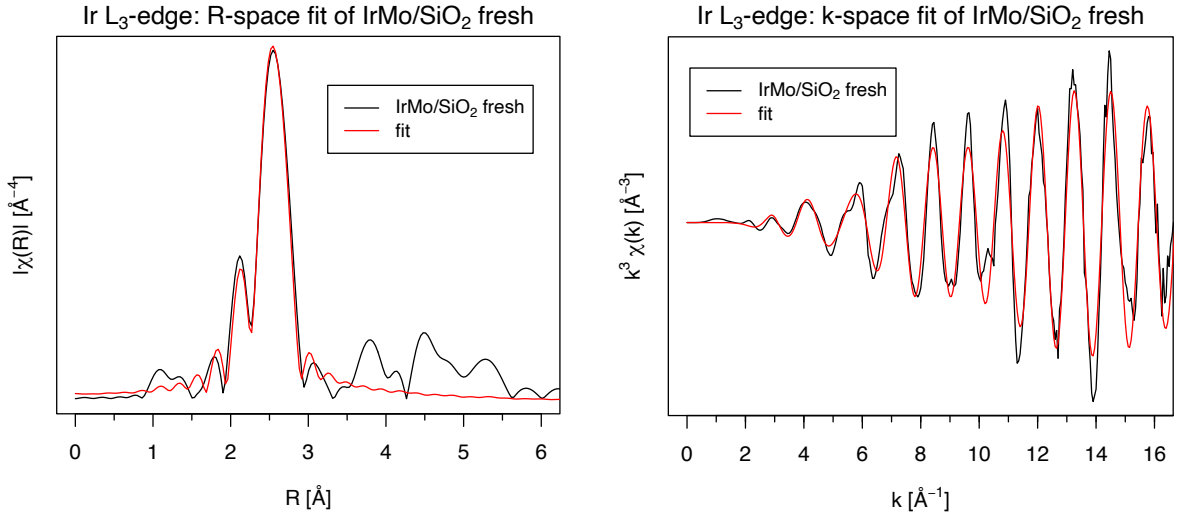

Figure S58. R-space and k-space EXAFS fit of the Ir L_3-edge data of IrMo/SiO_2 before HDO reaction.

Table S5. EXAFS fitting results of IrMo/SiO_2 before the HDO reaction.

Coordination shell	**N**	**σ^2, Å^2**	**R, Å**	**Reff, Å**	**ΔE_0, eV**
Ir L_3-edge					
Ir-Ir	9.7±0.7	0.0042±0.0003	2.687±0.003	2.691	7.3±0.7

Sample: IrMo/SiO_2 after reaction.

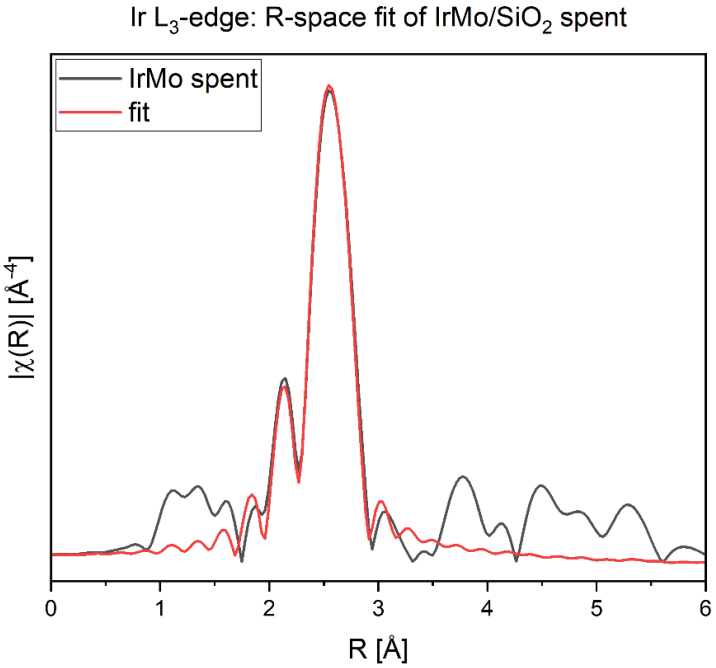

Figure S59. R-space EXAFS fit of the Ir L_3-edge data of IrMo/SiO_2 after HDO reaction.

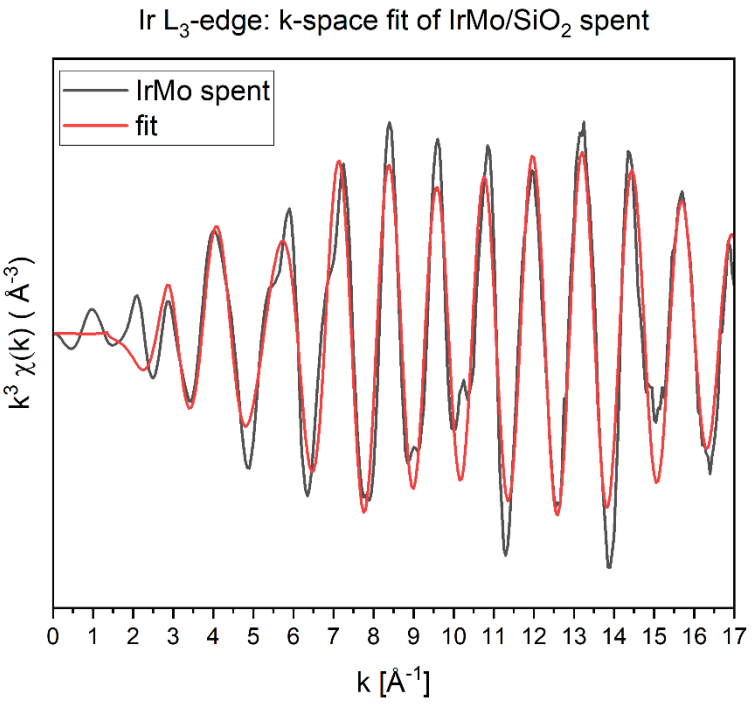

Figure S60. k-space EXAFS fit of the Ir L_3-edge data of $IrMo/SiO_2$ after HDO reaction.

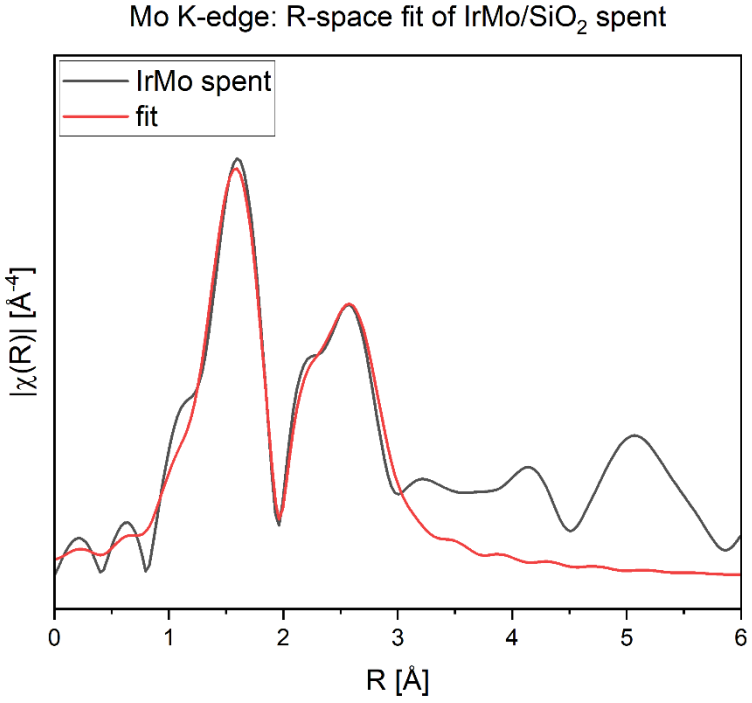

Figure S61. R-space EXAFS fit of the Mo K-edge data of $IrMo/SiO_2$ after HDO reaction.

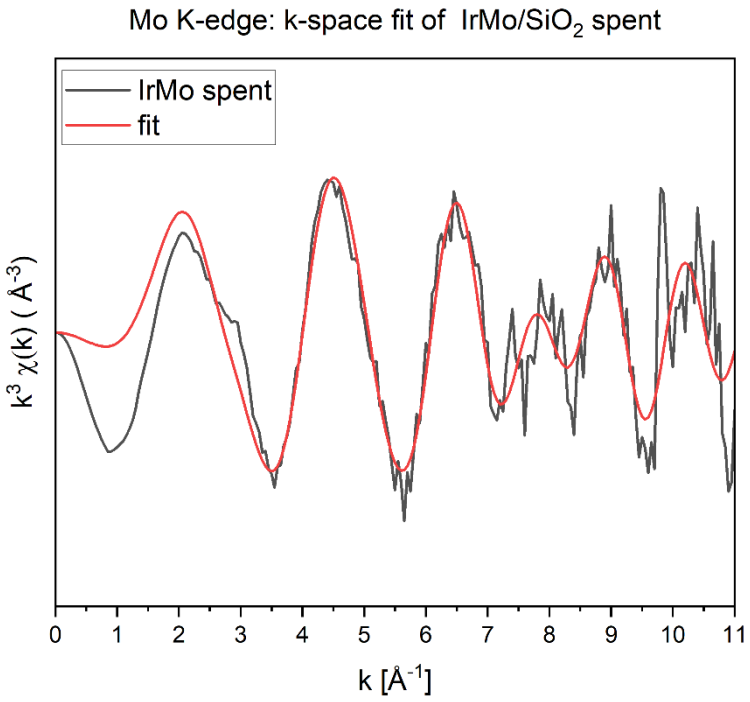

Figure S62. k-space EXAFS fit of the Mo K-edge data of $IrMo/SiO_2$ after reaction.

Table S6. EXAFS fitting results of $IrMo/SiO_2$ after HDO reaction.

Coordination shell	**N**	**σ^2, Å^2**	**R, Å**	**Reff, Å**	**ΔE_0, eV**
Ir L_3-edge					
Ir-Ir	9.7±0.6	0.0044±0.0002	2.697±0.003	2.691	7.2±0.6
Mo K-edge					
Mo-O	3.3±2.0	0.0065±0.0088	2.052±0.068	1.983	-0.5±8.5
Mo-Ir	2.5±1.4	0.0044±0.0002	2.745±0.051	2.691	-0.5±8.5

Sample: Pt/SiO_2 fresh.

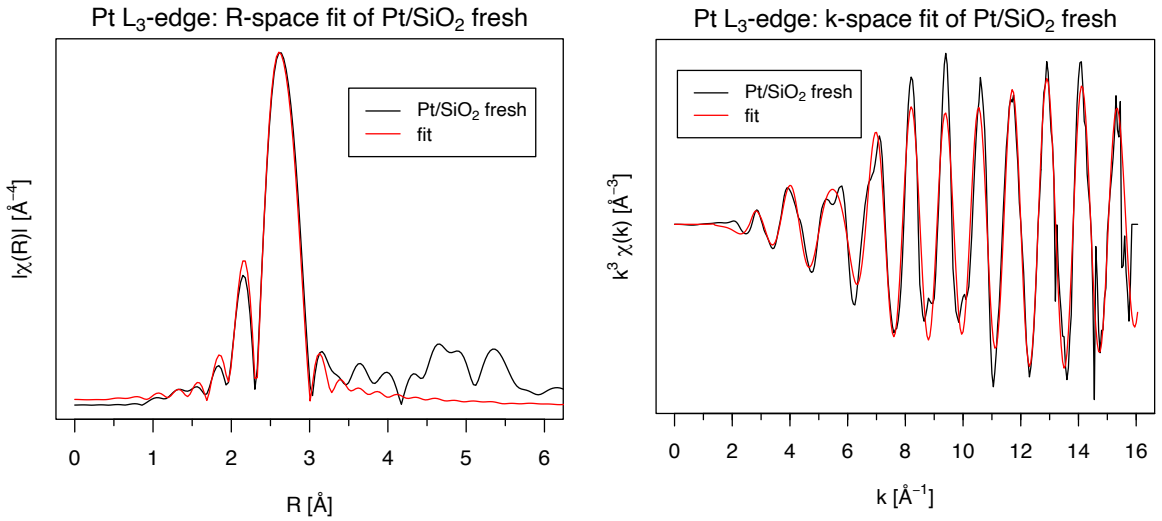

Figure S63. R-space and k-space EXAFS fit of the Pt L_3-edge data of Pt/SiO_2 before HDO reaction.

Table S7. EXAFS fitting results of Pt/SiO_2 before the HDO reaction.

Coordination shell	**N**	**σ^2, Å^2**	**R, Å**	**Reff, Å**	**ΔE_0, eV**	**Rf**
Pt L_3-edge						
Pt-Pt	10.3±0.4	0.006±0.0002	2.752±0.002	2.774	7.3±0.4	0.0109

Sample: Pt/SiO_2 after reaction.

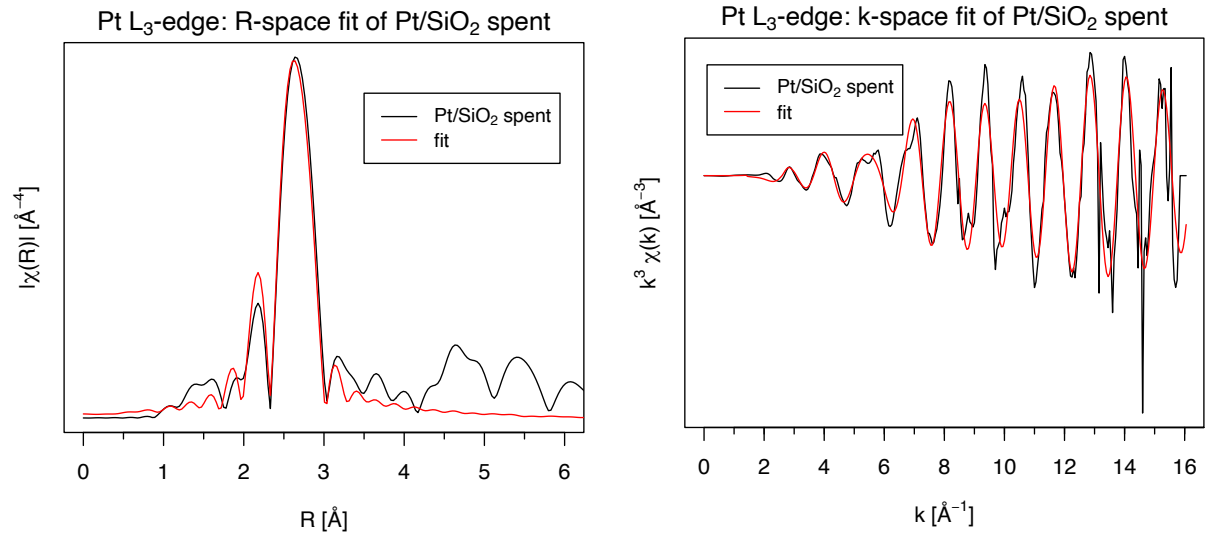

Figure S64. R-space and k-space EXAFS fit of the Pt L_3-edge data of Pt/SiO_2 after HDO reaction.

Table S8. EXAFS fitting results of Pt/SiO_2 after the HDO reaction

Coordination shell	N	σ^2, Å^2	R, Å	Reff, Å	ΔE_0, eV	Rf
Pt L_3-edge						
Pt-Pt	10.9±0.6	0.005±0.0003	2.763±0.003	2.774	7.5±0.5	0.0199

Sample: $PtMo/SiO_2$ fresh.

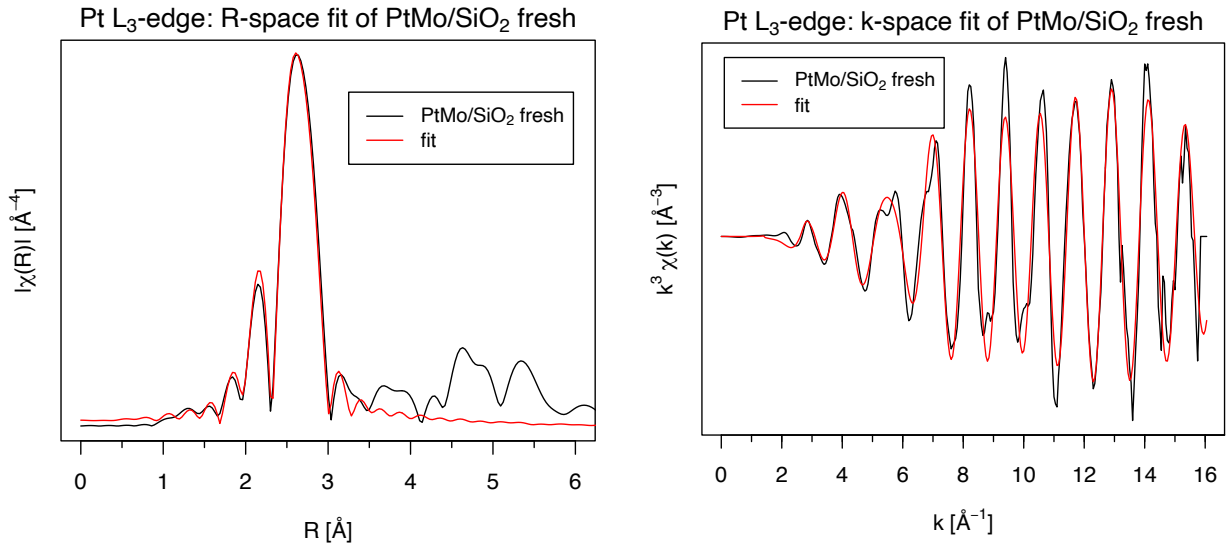

Figure S65. R-space and k-space EXAFS fit of the Pt L_3-edge data of $PtMo/SiO_2$ before HDO reaction.

Table S9. EXAFS fitting results of $PtMo/SiO_2$ before the HDO reaction.

Coordination shell	N	σ^2, Å^2	R, Å	Reff, Å	ΔE_0, eV
Pt L_3-edge					
Pt-Pt	10.3±0.4	0.0060±0.0002	2.753±0.002	2.774	7.6±0.4

Sample: PtMo/SiO_2 after reaction.

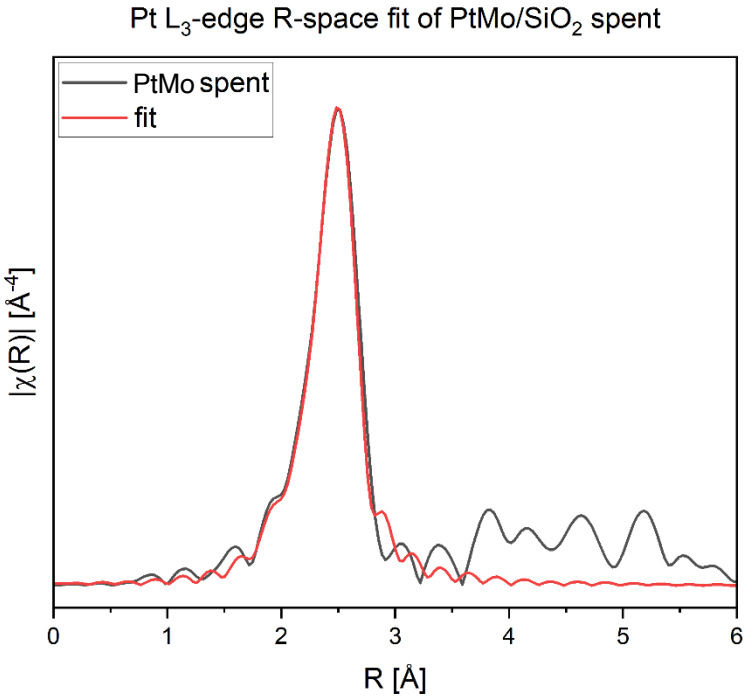

Figure S66. R-space EXAFS fit of the Pt L_3-edge data for PtMo/SiO_2 after HDO reaction.

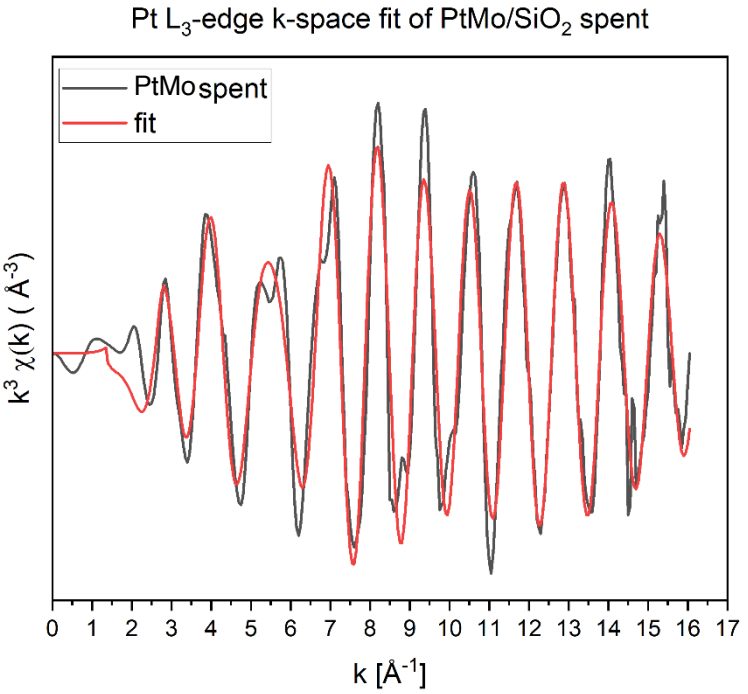

Figure S67. k-space EXAFS fit of Pt L_3-edge data for PtMo/SiO_2 after HDO reaction.

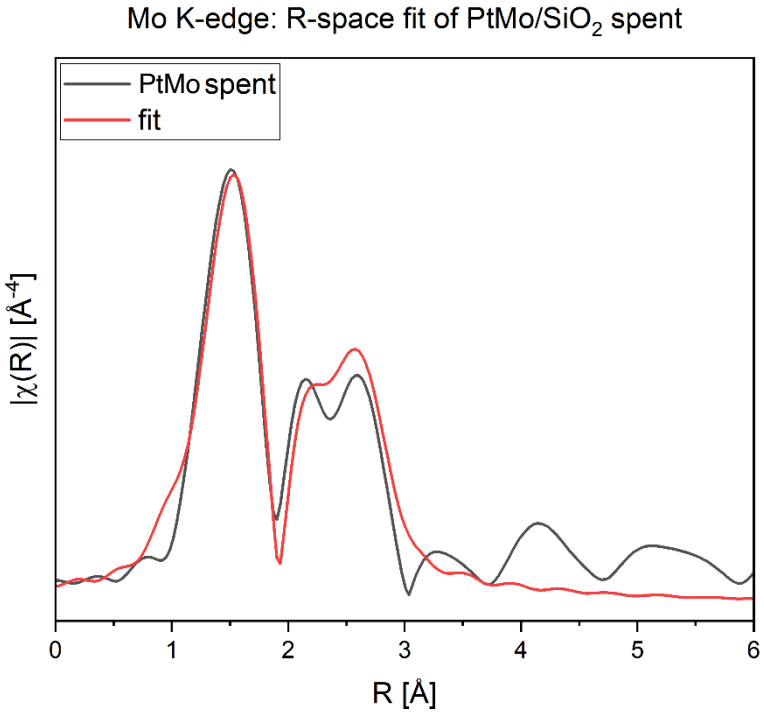

Figure S68. R-space EXAFS fit of the Mo K-edge data of PtMo/SiO_2 after HDO reaction.

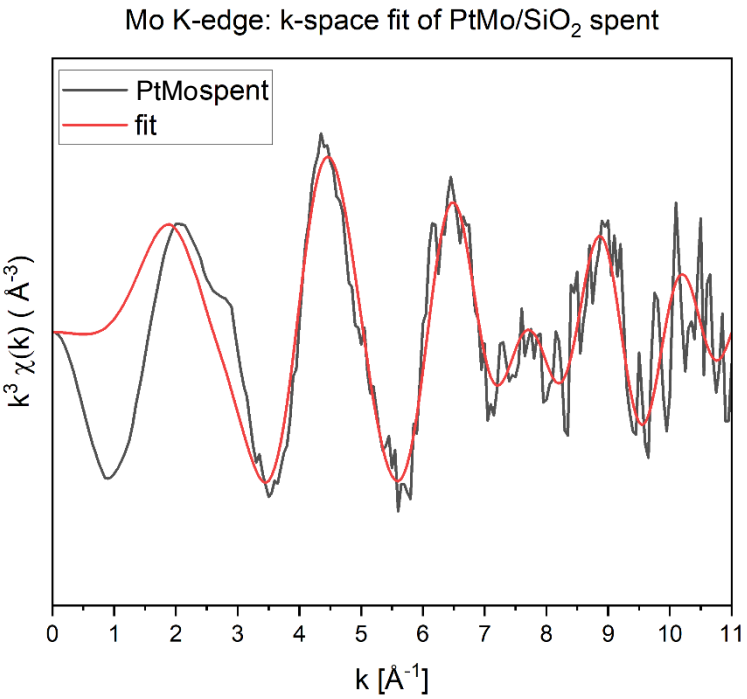

Figure S69. k-space EXAFS fit of the Mo K-edge data of PtMo/SiO_2 after HDO reaction.

Table S10: EXAFS fitting results of $PtMo/SiO_2$ after HDO reaction.

Coordination shell	N	σ^2, Å^2	R, Å	Reff, Å	ΔE_0, eV
Pt L_3-edge					
Pt-Pt	9.7±0.4	0.0054±0.0002	2.758±0.002	2.774	7.1±0.3
Mo K-edge					
Mo-O	3.5±1.3	0.0054±0.0045	2.025±0.032	1.983	-4.8±4.6
Mo-Pt	2.8±0.9	0.0054±0.0002	2.743±0.031	2.774	-4.8±4.6

Sample: Pd/SiO_2 before reaction.

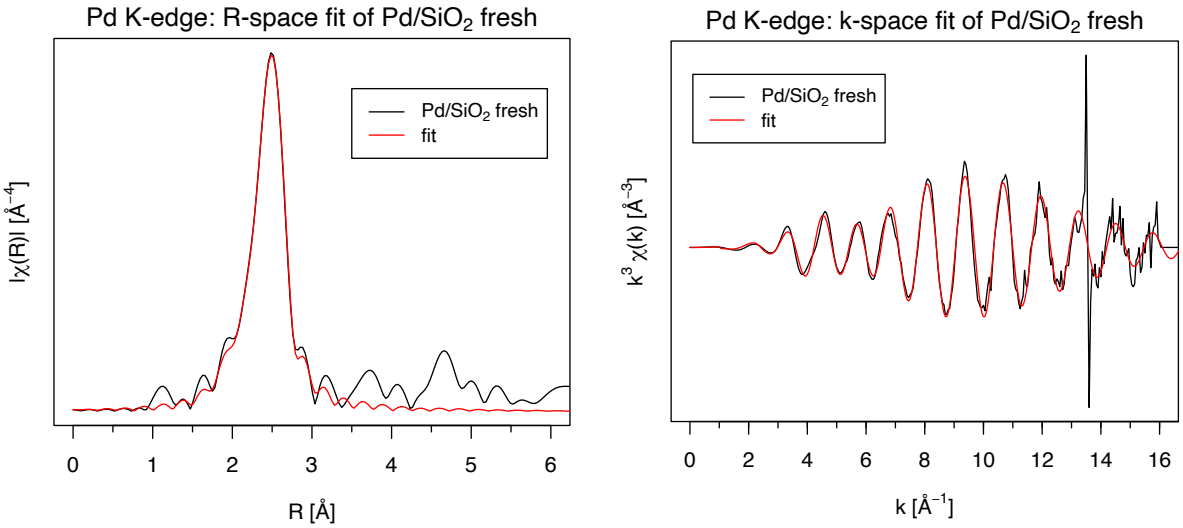

Figure S70. R-space and k-space EXAFS fit of the Pd K-edge data of Pd/SiO_2 before HDO reaction.

Table S11. EXAFS fitting results of Pd/SiO_2 before the HDO reaction.

Coordination shell	N	σ^2, Å^2	R, Å	Reff, Å	ΔE_0, eV	Rf
Pd K-edge						
Pd-Pd	10.0±0.5	0.007±0.0003	2.735±0.003	2.751	4.0±0.3	0.0109

Sample: Pd/SiO_2 after reaction.

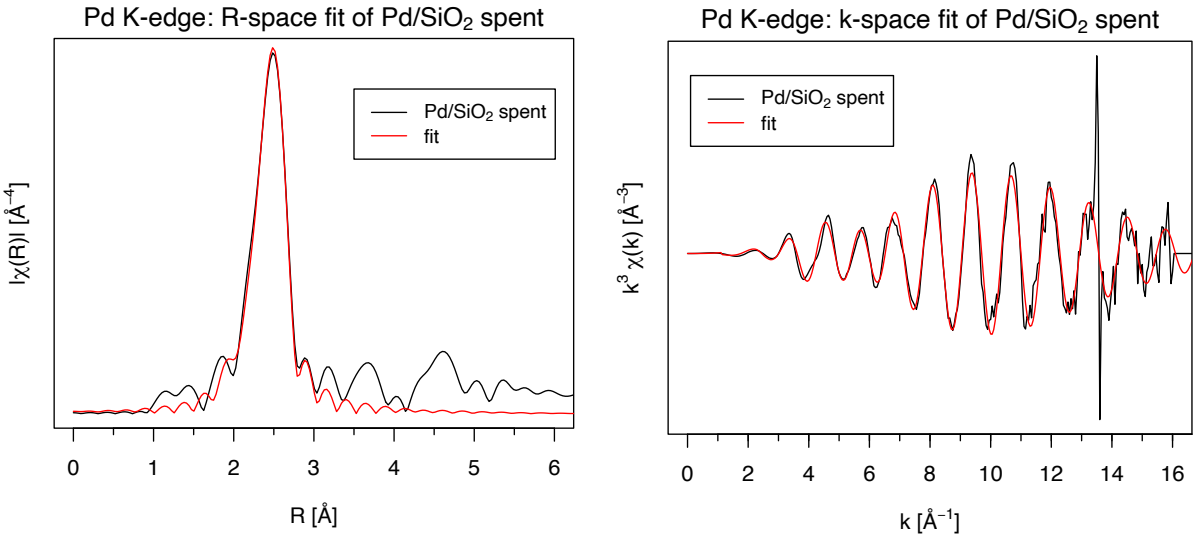

Figure S71. R-space and k-space EXAFS fit of the Pd K-edge data of Pd/SiO_2 after HDO reaction.

Table S12. EXAFS fitting results of Pd/SiO_2 after the HDO reaction.

Coordination shell	**N**	**σ^2, Å^2**	**R, Å**	**Reff, Å**	**ΔE_0, eV**	**Rf**
Pd K-edge						
Pd-Pd	10.6±0.5	0.006±0.0003	2.735±0.003	2.751	4.6±0.4	0.0171

Sample: $PdMo/SiO_2$ before reaction.

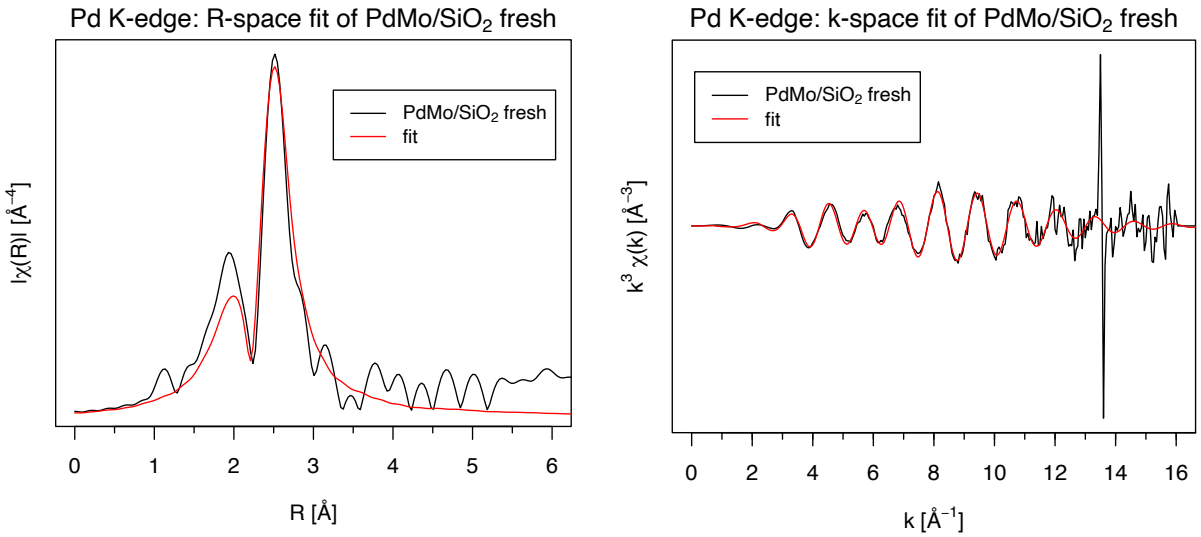

Figure S72. R-space and k-space EXAFS fit of the Pd K-edge data of $PdMo/SiO_2$ before HDO reaction.

Table S13. EXAFS fitting results of $PdMo/SiO_2$ before the HDO reaction.

Coordination shell	N	σ^2, Å^2	R, Å	Reff, Å	ΔE_0, eV
Pd K-edge					
Pd-Pd	8.3±0.7	0.010±0.0008	2.718±0.007	2.751	2.4±0.6

Sample: $PdMo/SiO_2$ after reaction.

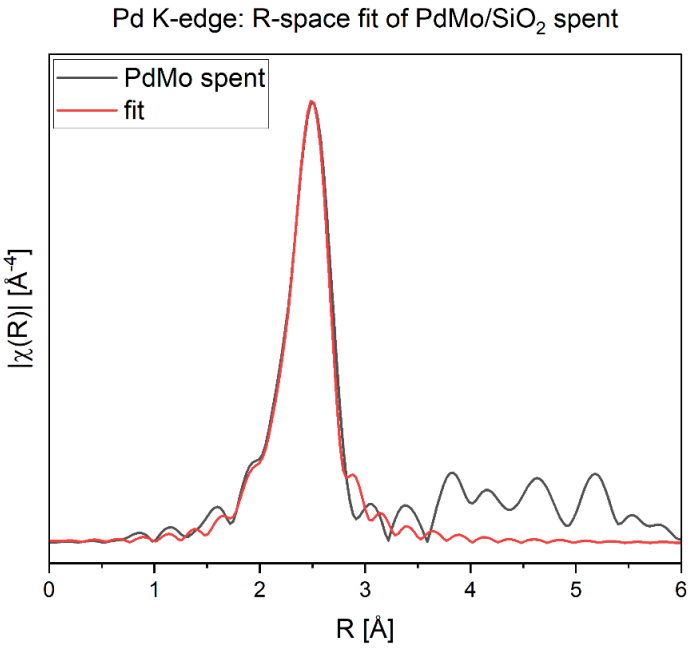

Figure S73. R-space EXAFS fit of the Pd K-edge data of $PdMo/SiO_2$ after HDO reaction.

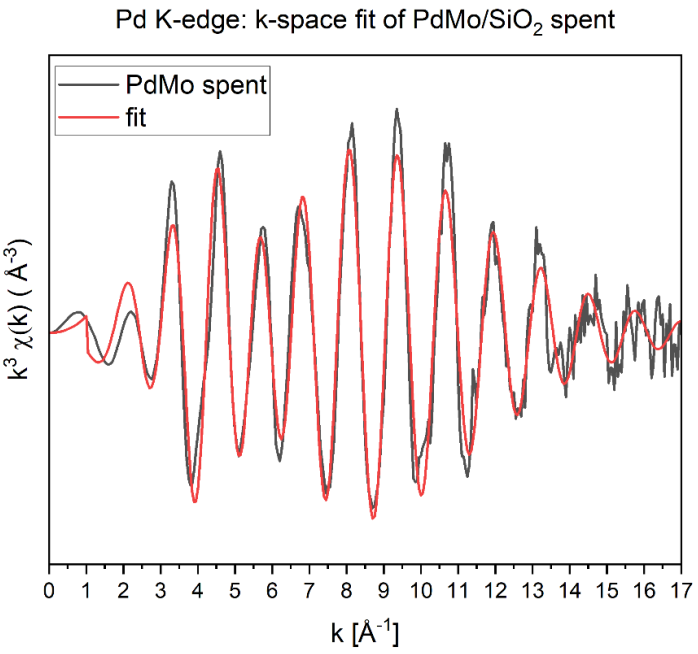

Figure S74. k-space EXAFS fit of the Pd K-edge data of $PdMo/SiO_2$ after HDO reaction.

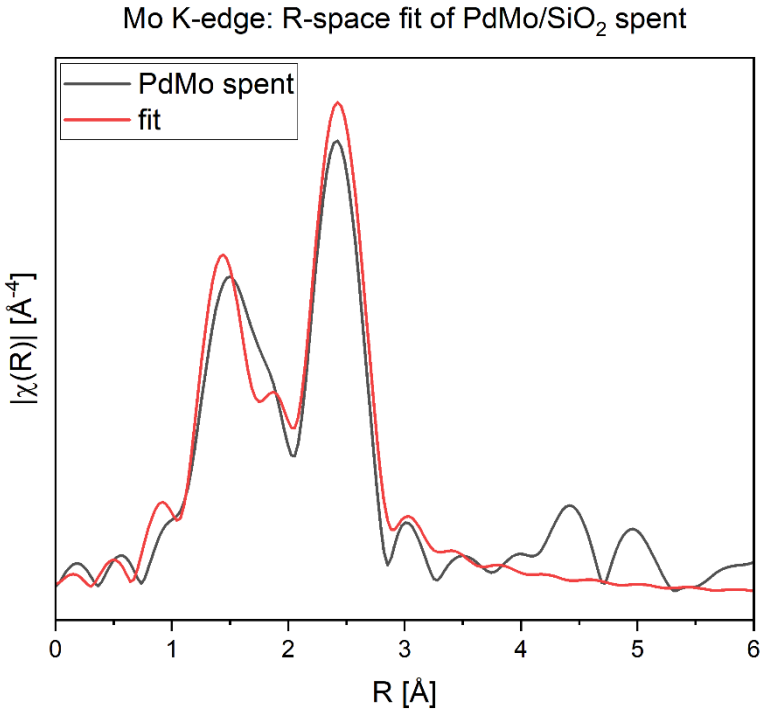

Figure S75. R-space EXAFS fit of the Mo K-edge data of $PdMo/SiO_2$ after HDO reaction.

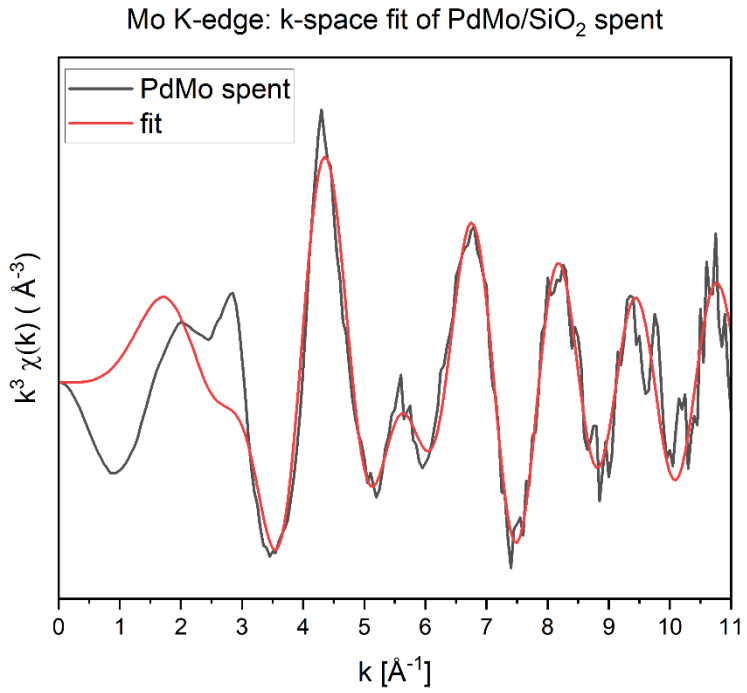

Figure S76. k-space EXAFS fit of the Mo K-edge data of $PdMo/SiO_2$ after HDO reaction.

Table S14. EXAFS fitting results of $PdMo/SiO_2$ after HDO reaction.

Coordination shell	N	σ^2, Å^2	R, Å	Reff, Å	ΔE_0, eV
Pd K-edge					
Pd-Pd	10.9±0.5	0.0070±0.0003	2.737±0.003	2.751	4.2±0.3
Mo K-edge					
Mo-O	3.3±0.8	0.0067±0.0031	2.024±0.015	1.982	-7.5±1.3
Mo-Pd	4.1±0.4	0.0070±0.0003	2.706±0.009	2.751	-7.5±1.3

Sample: Rh/SiO_2 before reaction.

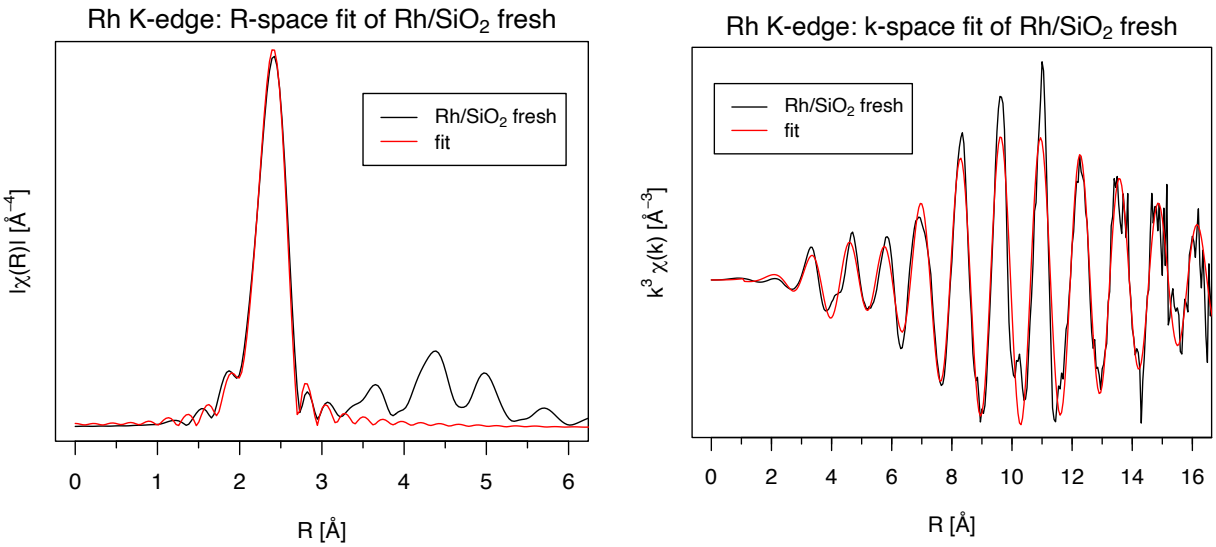

Figure S77. R-space and k-space EXAFS fit of the Rh K-edge data of Rh/SiO_2 before HDO reaction.

Table S15. EXAFS fitting results of Rh/SiO_2 before HDO reaction.

Coordination shell	N	σ^2, Å^2	R, Å	Reff, Å	ΔE_0, eV	Rf
Rh K-edge						
Rh-Rh	11.0±0.7	0.005±0.0004	2.683±0.003	2.539	4.4±0.5	0.0168

Sample: Rh/SiO_2 after reaction.

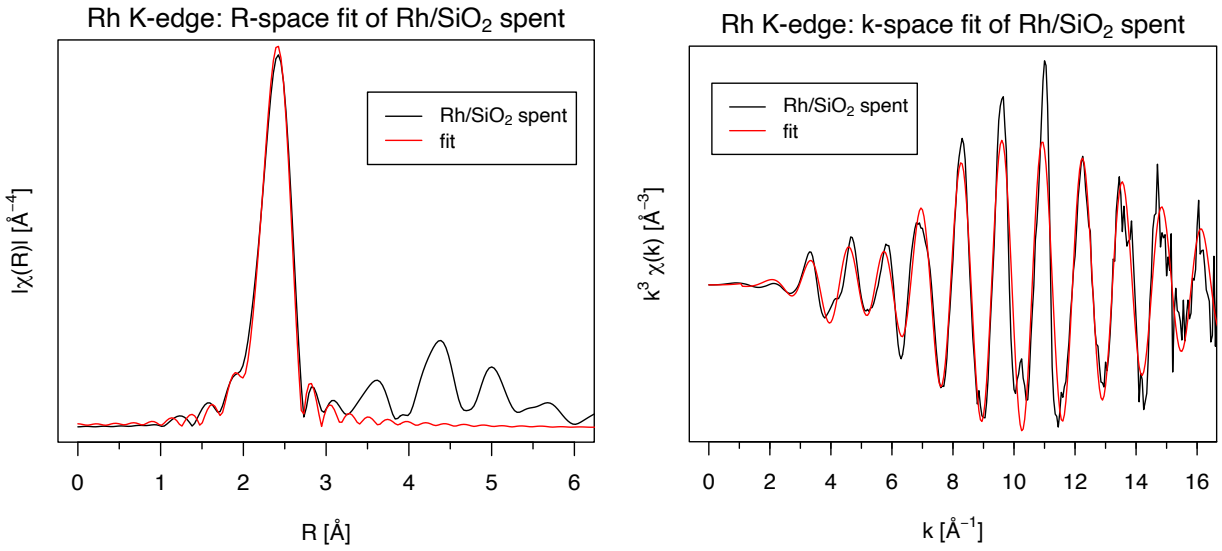

Figure S78. R-space and k-space EXAFS fit of the Rh K-edge data of Rh/SiO_2 after HDO reaction.

Table S16. EXAFS fitting results of Rh/SiO_2 after HDO reaction.

Coordination shell	N	σ^2, Å^2	R, Å	Reff, Å	ΔE_0, eV	Rf
Rh K-edge						
Rh-Rh	11.2±0.7	0.005±0.0004	2.688±0.003	2.539	4.2±0.5	0.0192

Sample: RhMo before reaction.

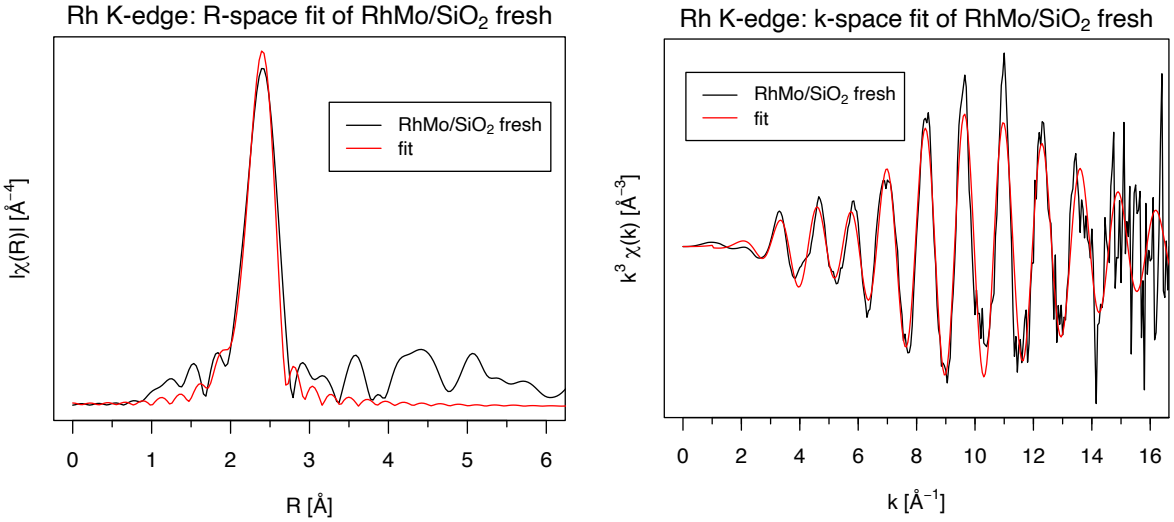

Figure S79. R-space and k-space EXAFS fit of the Rh K-edge data of $RhMo/SiO_2$ before HDO reaction.

Table S17. EXAFS fitting results of $RhMo/SiO_2$ before HDO reaction.

Coordination shell	N	σ^2, Å^2	R, Å	Reff, Å	ΔE_0, eV
Rh K-edge					

Rh-Rh	11.2±0.7	0.005±0.0004	2.688±0.003	2.539	4.2±0.5

Sample: RhMo/SiO_2 after reaction.

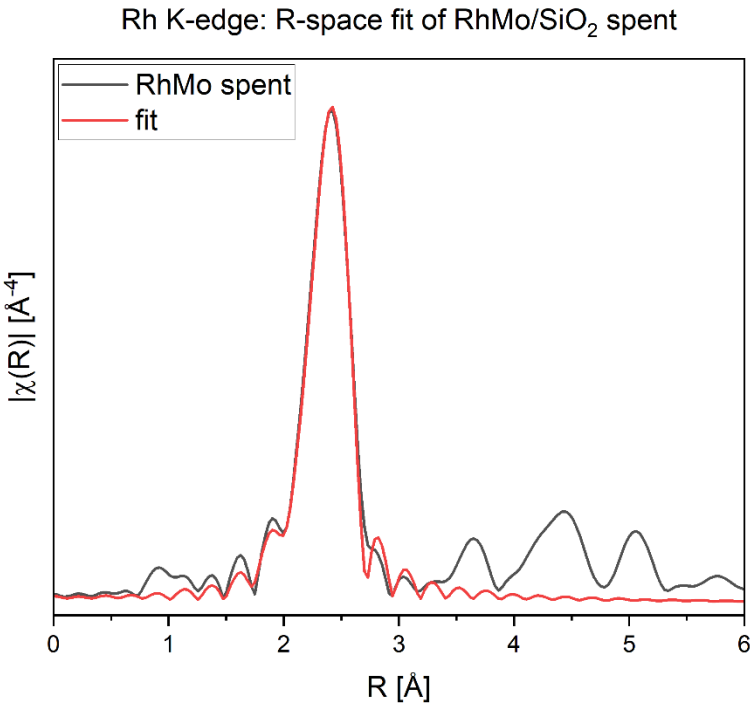

Figure S80. R-space EXAFS fit of the Rh K-edge data of RhMo/SiO_2 after HDO reaction.

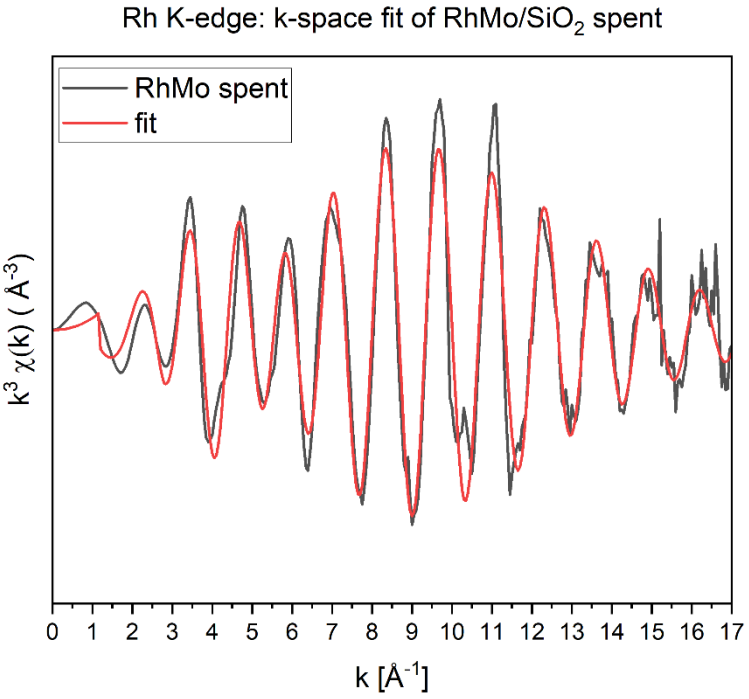

Figure S81. k-space EXAFS fit of the Rh K-edge data of RhMo/SiO_2 after HDO reaction.

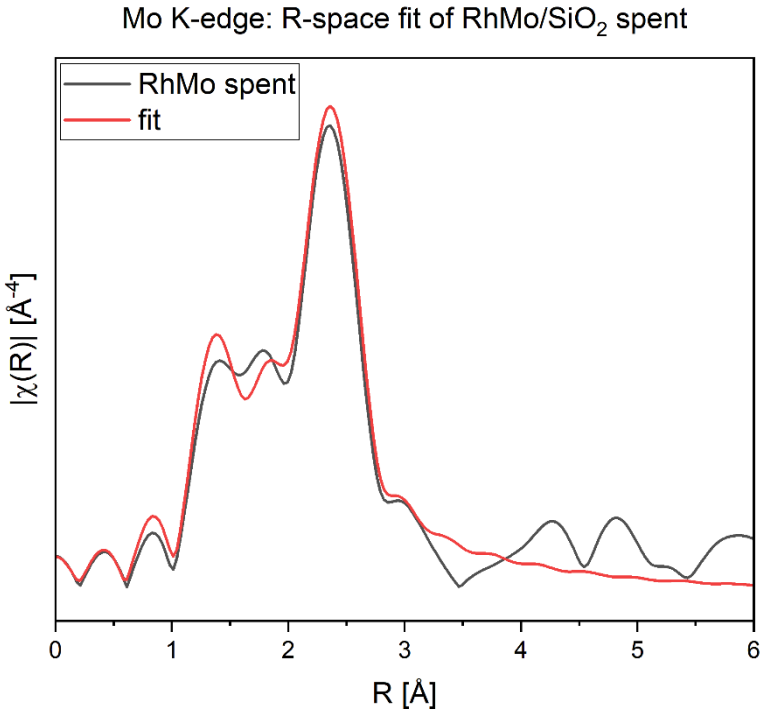

Figure S82. R-space EXAFS fit of the Mo K-edge data of RhMo/SiO_2 after HDO reaction.

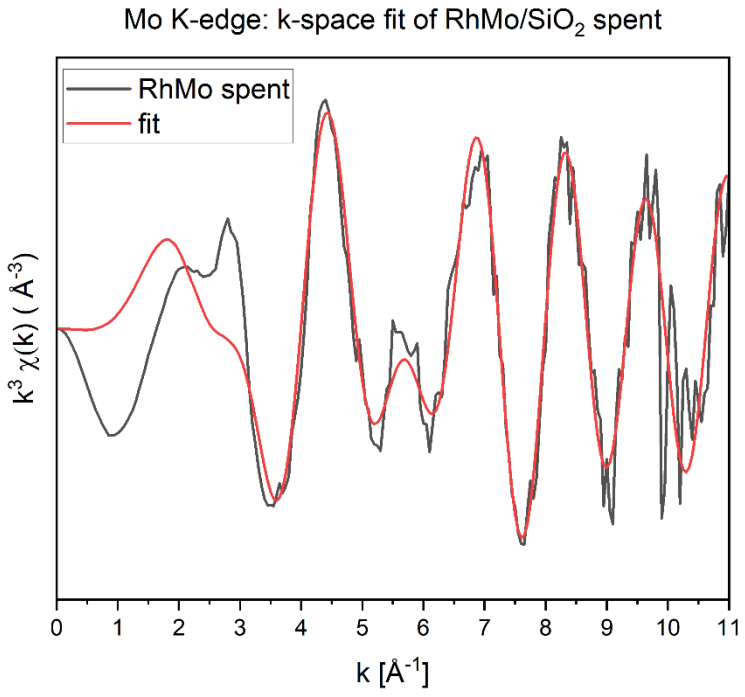

Figure S83. k-space EXAFS fit of the Mo K-edge data of RhMo/SiO_2 after HDO reaction.

Table S18. EXAFS fitting results of RhMo/SiO_2 after HDO reaction.

Coordination shell	N	σ^2, Å^2	R, Å	Reff, Å	ΔE_0, eV
Rh K-edge					
Rh-Rh	9.7±0.5	0.0046±0.0003	2.678±0.003	2.689	5.5±0.4
Mo K-edge					
Mo-O	3.2±1.5	0.0053±0.0047	2.010±0.023	1.983	-6.3±2.1
Mo-Rh	3.7±0.5	0.0046±0.0003	2.667±0.013	2.689	-6.3±2.1

Sample: Ni/SiO_2 before reaction.

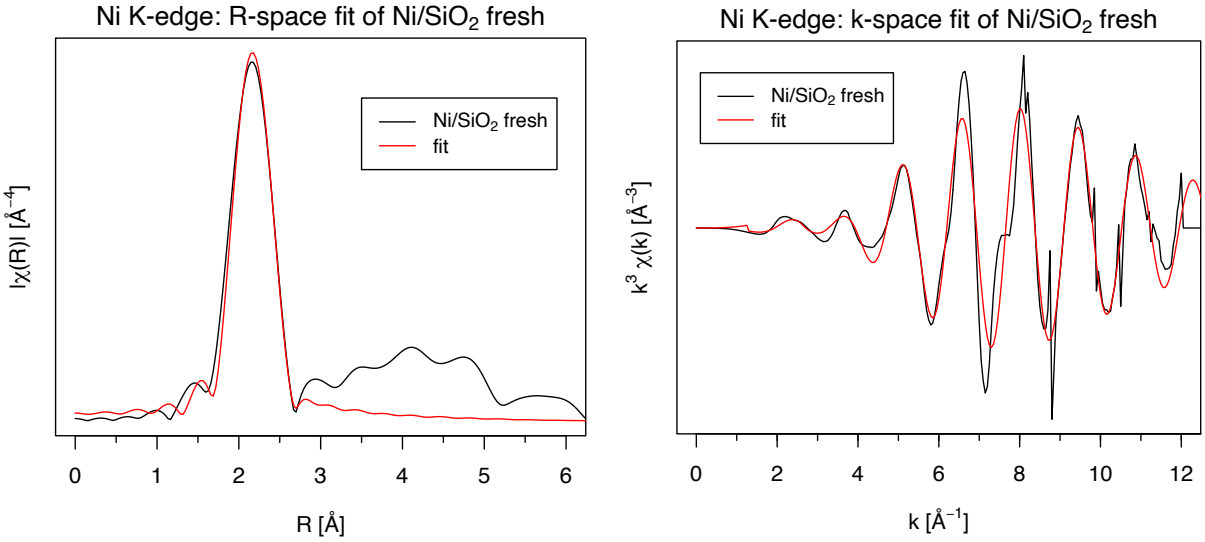

Figure S84. R-space and k-space EXAFS fit of the Ni K-edge data of Ni/SiO_2 before HDO reaction.

Table S19. EXAFS fitting results of Ni/SiO_2 before HDO reaction.

Coordination shell	N	σ^2, Å^2	R, Å	Reff, Å	ΔE_0, eV	Rf
Ni K-edge						
Ni-Ni	8.2±1.2	0.006±0.0012	2.475±0.009	2.492	6.0±1.6	0.0368

Sample: Ni/SiO_2 after reaction.

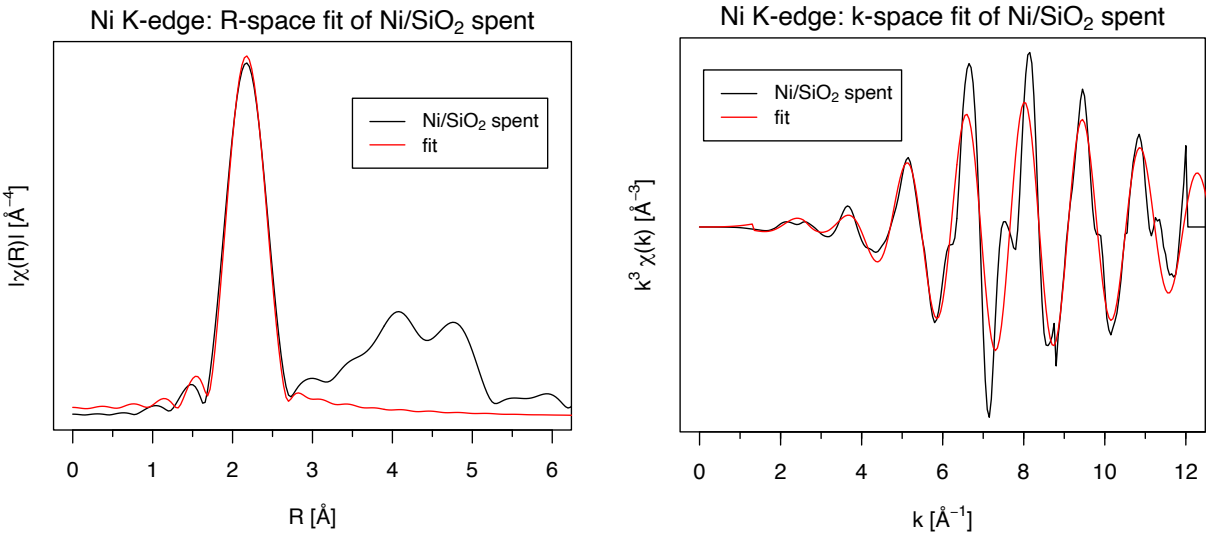

Figure S85. R-space and k-space EXAFS fit of the Ni K-edge data of Ni/SiO_2 after HDO reaction.

Table S20. EXAFS fitting results of Ni/SiO_2 after HDO reaction.

Coordination shell	N	σ^2, Å^2	R, Å	Reff, Å	ΔE_0, eV	Rf
Ni K-edge						
Ni-Ni	9.8±1.2	0.006±0.0010	2.477±0.008	2.492	6.8±1.3	0.0264

Sample: $NiMo/SiO_2$ before reaction.

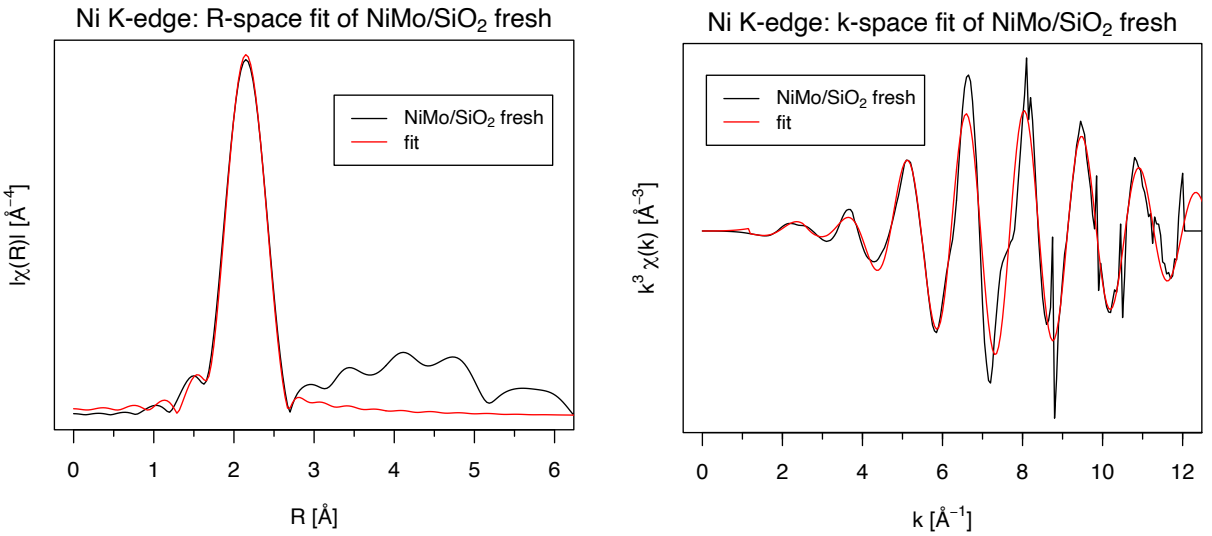

Figure S86. R-space and k-space EXAFS fit of the Ni K-edge data of $NiMo/SiO_2$ before HDO reaction.

Table S21. EXAFS fitting results of $NiMo/SiO_2$ before HDO reaction.

Coordination shell	N	σ^2, Å^2	R, Å	Reff, Å	ΔE_0, eV
Ni K-edge					
Ni-Ni	8.6±0.9	0.008±0.0009	2.466±0.007	2.492	5.3±1.1

Sample: $NiMo/SiO_2$ after reaction.

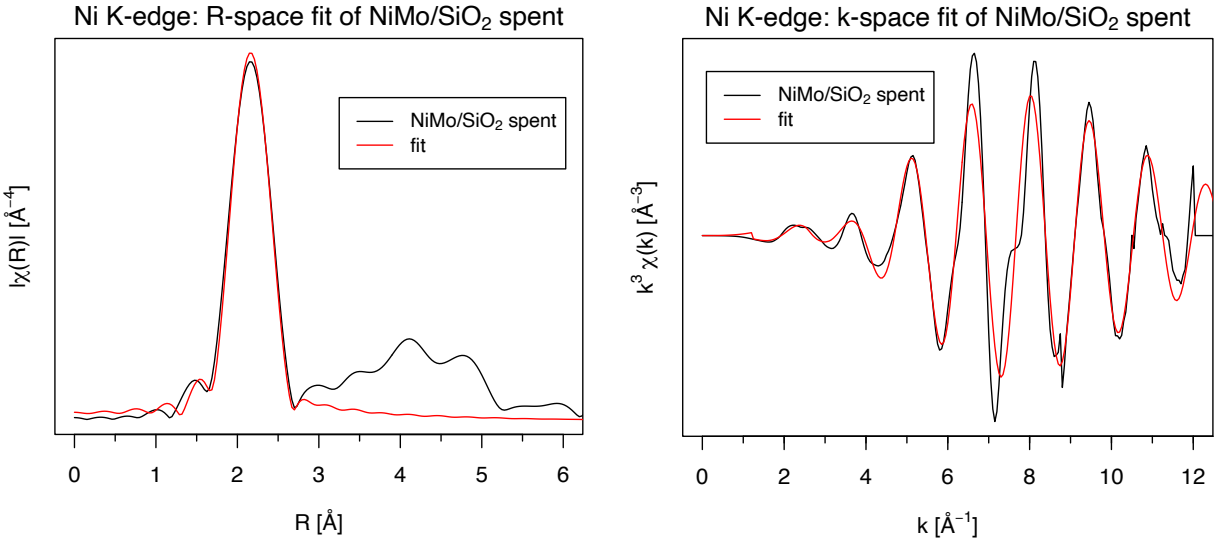

Figure S87. R-space and k-space EXAFS fit of the Ni K-edge data of $NiMo/SiO_2$ after HDO reaction.

Table S22. EXAFS fitting results of $NiMo/SiO_2$ after HDO reaction.

Coordination shell	N	σ^2, Å^2	R, Å	Reff, Å	ΔE_0, eV
Ni K-edge					
Ni-Ni	8.3±0.6	0.007±0.0007	2.472±0.005	2.492	5.9±0.8

Fitting of Mo K Edge EXAFS with Mo–Mo instead of Mo–M in Bimetallic Materials

Table S23. Comparison of R factors for the dual fits using models that include a Mo-O path along with either a Mo-Mo or Mo-M path. The bimetallic models incorporating Mo-M (M=Rh, Pd, Pt, and Ir) paths result in better fits for the spent catalysts.

Combined Mo K-edge + M K/L_3-edge fit	Model Mo-O +	Rf
IrMo/SiO_2 spent	Mo-Mo	0.0385
	Mo-Ir	0.0269
PtMo/SiO_2 spent	Mo-Mo	0.0341
	Mo-Pt	0.0227
RhMo/SiO_2 spent	Mo-Mo	0.0196
	Mo-Rh	0.0179
PdMo/SiO_2 spent	Mo-Mo	0.0227
	Mo-Pd	0.0190

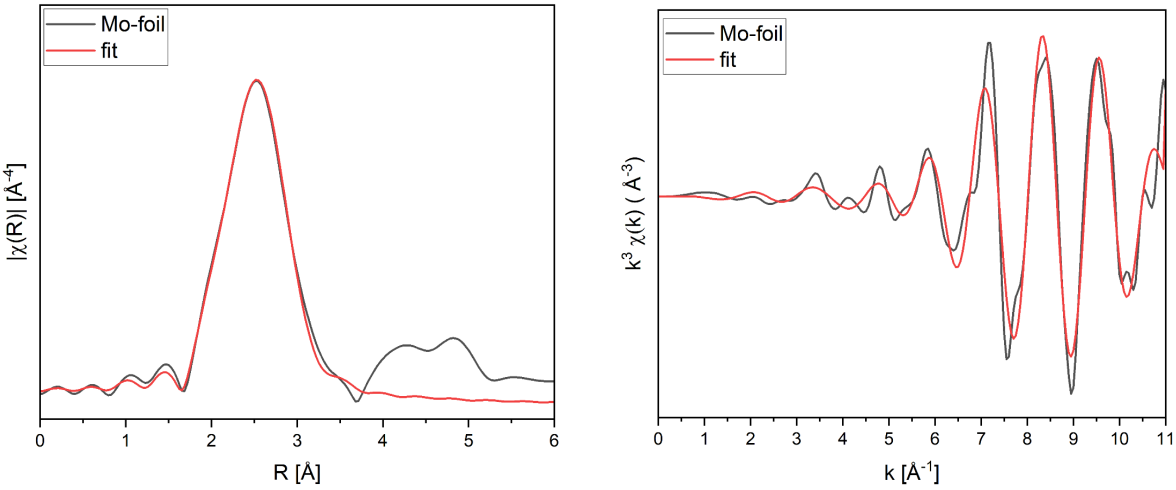

Figure S88. R-space (left) and k-space (right) EXAFS fit of the Mo K-edge data of bcc Mo-foil.

Table S24. EXAFS fitting results of bcc Mo foil. Rf = 0.0065.

Coordination shell	**N**	**σ^2, $Å^2$**	**R, Å**	**Reff, Å**	**ΔE_0, eV**
Mo K-edge					
Mo-Mo	8	0.0029±0.0009	2.700±0.004	2.726	2.7±1.6
Mo-Mo	6	0.0008±0.0011	3.118±0.004	3.147	2.7±1.6

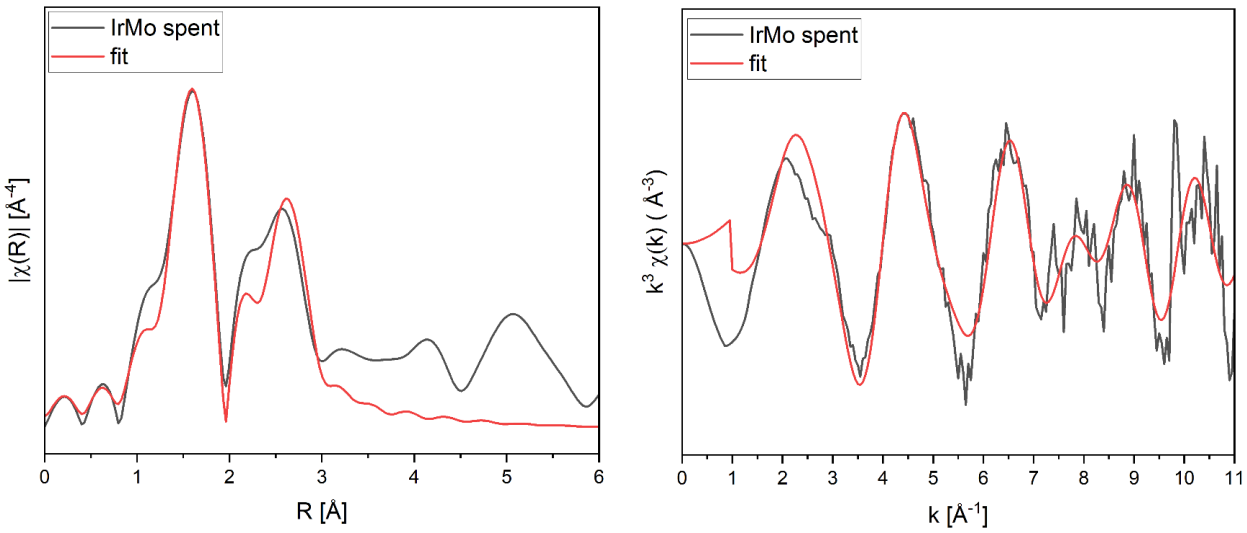

Figure S89. R-space (left) and k-space (right) EXAFS fit of the Mo K-edge data of IrMo/SiO_2 after HDO reaction using Mo-O and Mo-Mo paths.

Table S25. EXAFS fitting results of IrMo/SiO_2 after HDO reaction, using Mo-O and Mo-Mo paths.

Coordination shell	**N**	**σ^2, Å^2**	**R, Å**	**Reff, Å**	**ΔE_0, eV**
Ir L_3-edge					
Ir-Ir	9.7±0.6	0.0044	2.697±0.003	2.691	7.2±0.6
Mo K-edge					
Mo-O	3.0±1.6	0.0052±0.0080	2.076±0.049	1.983	3.7±1.6
Mo-Mo	1.4±0.9	0.0043±0.0002	2.906±0.047	2.726	3.7±1.6

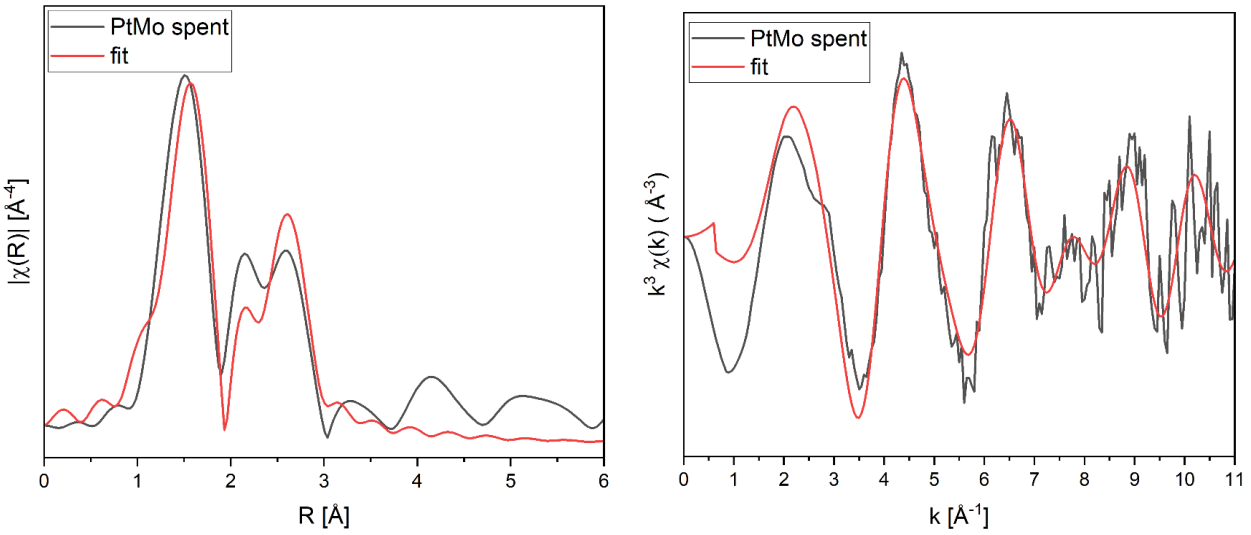

Figure S90. R-space (left) and k-space (right) EXAFS fit of the Mo K-edge data of PtMo/SiO_2 after HDO reaction using Mo-O and Mo-Mo paths.

Table S26. EXAFS fitting results of $PtMo/SiO_2$ after HDO reaction, using Mo-O and Mo-Mo paths.

Coordination shell	**N**	**σ^2, Å^2**	**R, Å**	**Reff, Å**	**ΔE_0, eV**
Pt L_3-edge					
Pt-Pt	9.7±0.4	0.0054	2.758±0.002	2.774	7.1±0.4
Mo K-edge					
Mo-O	3.8±1.4	0.0068±0.0049	2.064±0.029	1.983	1.4±3.5
Mo-Mo	1.7±0.6	0.0054±0.0002	2.905±0.030	2.726	1.4±3.5

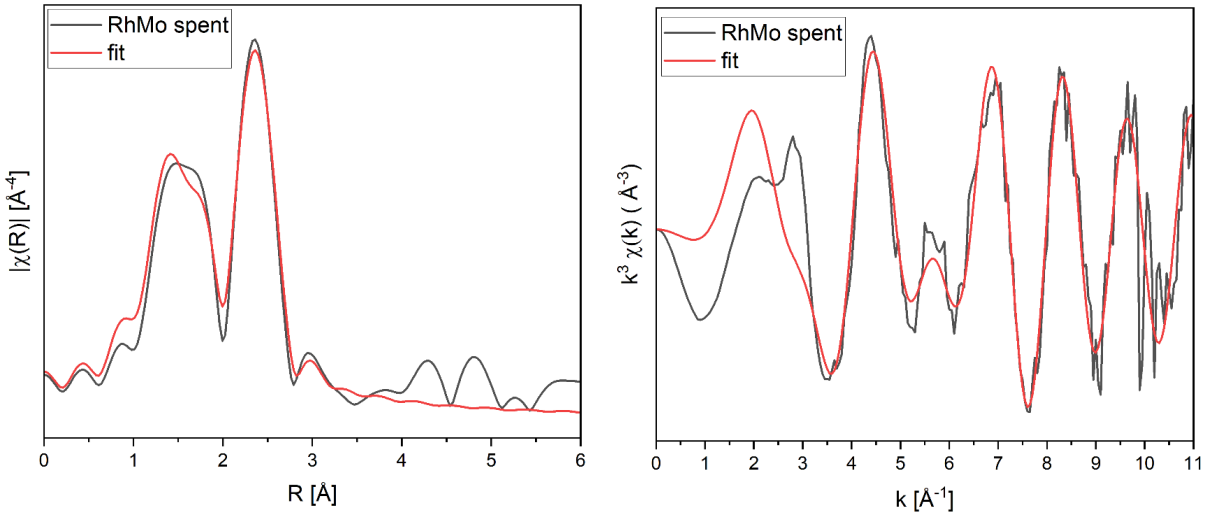

Figure S91. R-space (left) and k-space (right) EXAFS fit of the Mo K-edge data of $RhMo/SiO_2$ after HDO reaction using Mo-O and Mo-Mo paths.

Table S27. EXAFS fitting results of $RhMo/SiO_2$ after HDO reaction, using Mo-O and Mo-Mo paths.

Coordination shell	**N**	**σ^2, Å^2**	**R, Å**	**Reff, Å**	**ΔE_0, eV**
Rh K-edge					
Rh-Rh	9.7±0.5	0.0046	2.678±0.003	2.678	5.5±0.4
Mo K-edge					
Mo-O	4.5±1.5	0.0089±0.0053	2.033±0.025	1.983	-3.7±2.4
Mo-Mo	3.6±0.5	0.0046±0.0003	2.701±0.014	2.726	-3.7±2.4

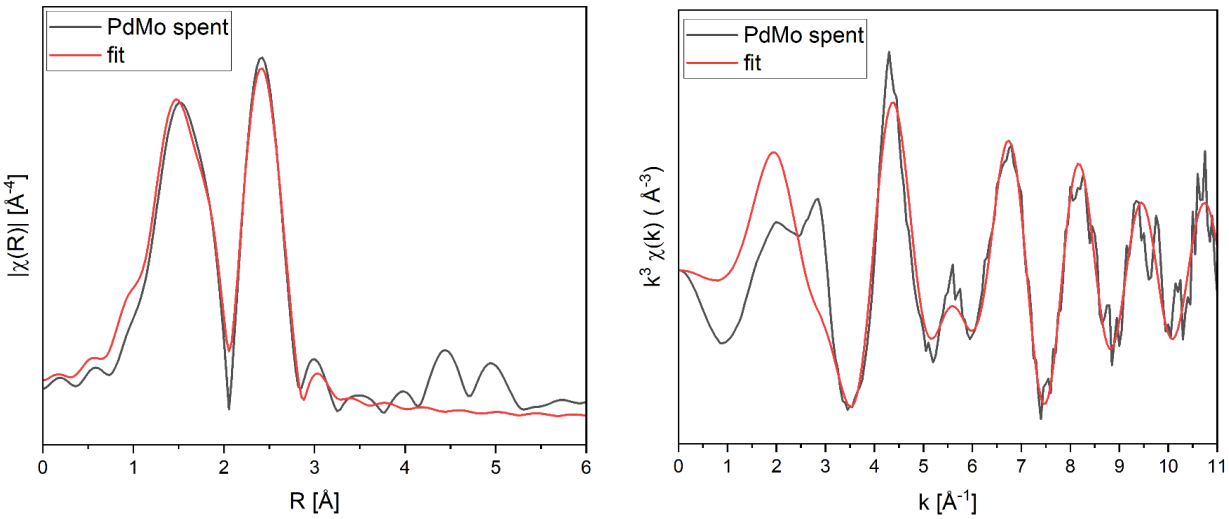

Figure S92. R-space (left) and k-space (right) EXAFS fit of the Mo K-edge data of PdMo/SiO_2 after HDO reaction using Mo-O and Mo-Mo paths.

Table S28. EXAFS fitting results of PdMo/SiO_2 after HDO reaction, using Mo-O and Mo-Mo paths.

Coordination shell	**N**	**σ^2, Å^2**	**R, Å**	**Reff, Å**	**ΔE_0, eV**
Pd K-edge					
Pd-Pd	10.9±0.5	0.0070	2.737±0.003	2.751	4.2±0.4
Mo K-edge					
Mo-O	4.8±1.1	0.0106±0.0037	2.063±0.018	1.983	-2.8±1.6
Mo-Mo	3.9±0.4	0.0070±0.0004	2.751±0.011	2.726	-2.8±1.6

13. References

(1) K. Searles, G. Siddiqi, O. V. Safonova, C. Copéret, 'Silica-supported isolated gallium sites as highly active, selective and stable propane dehydrogenation catalysts', *Chem. Sci.,* 2017, **8** (4), 2661.
(2) R. R. Schrock, 'Preparation and characterization of $M(CH_3)_5$ (M = Nb or Ta) and $Ta(CH_2C_6H_5)_5$ and evidence for decomposition by α-hydrogen atom abstraction', *J. Organomet. Chem.,* 1976, **122** (2), 209.
(3) W. L. Jolly, N. A. D. Carey, H. C. Clark. Bis(Cyclopentadienyl)Iron: (Ferrocene). In *Inorg. Synth.*, https://doi.org/10.1002/9780470132425.ch231968; pp 120.
(4) C. Ehinger, X. Zhou, M. Candrian, S. R. Docherty, S. Pollitt, C. Copéret, 'Group 10 Metal Allyl Amidinates: A Family of Readily Accessible and Stable Molecular Precursors to Generate Supported Nanoparticles', *JACS Au,* 2023, **3** (8), 2314.
(5) W. Zhou, S. R. Docherty, C. Ehinger, X. Zhou, C. Copéret, 'The promotional role of Mn in CO_2 hydrogenation over Rh-based catalysts from a surface organometallic chemistry approach', *Chem. Sci.,* 2023, **14** (20), 5379.
(6) W. Zhou, C. Hansen, W. Cao, E. Brack, S. R. Docherty, C. Ehinger, Y. Wang, C. Wang, C. Copéret, 'Gallium: A Universal Promoter Switching CO_2 Methanation Catalysts to Produce Methanol', *JACS Au,* 2025, **5** (1), 217.
(7) G. Bergeret, P. Gallezot. Particle Size and Dispersion Measurements. In *Handbook of Heterogeneous Catalysis*, https://doi.org/10.1002/9783527610044.hetcat0038pp 738.
(8) E. L. Lee, I. E. Wachs, 'In Situ Spectroscopic Investigation of the Molecular and Electronic Structures of SiO_2 Supported Surface Metal Oxides', *J. Phys. Chem. C,* 2007, **111** (39), 14410.
(9) Z. J. Berkson, R. Zhu, C. Ehinger, L. Lätsch, S. P. Schmid, D. Nater, S. Pollitt, O. V. Safonova, S. Björgvinsdóttir, A. B. Barnes, Y. Román-Leshkov, G. A. Price; et al., 'Active Site Descriptors from ^{95}Mo NMR Signatures of Silica-Supported Mo-Based Olefin Metathesis Catalysts', *J. Am. Chem. Soc.,* 2023, **145** (23), 12651.
(10) I. B. Moroz, K. Larmier, W.-C. Liao, C. Copéret, 'Discerning γ-Alumina Surface Sites with Nitrogen-15 Dynamic Nuclear Polarization Surface Enhanced NMR Spectroscopy of Adsorbed Pyridine', *J. Phys. Chem. C,* 2018, **122** (20), 10871.
(11) L. Lätsch, C. J. Kaul, A. V. Yakimov, R. McEntee, T. D. Baerdemaeker, A.-N. Parvulescu, K. Seidel, J. H. Teles, C. Copéret, 'Nature of Reactive Sites in TS-1 from 15N Solid-State NMR and Ti K-Edge X-Ray Absorption Spectroscopic Signatures Upon Pyridine Adsorption', *J. Am. Chem. Soc.,* 2024, **146** (43), 29675.
(12) S. Liu, W. Zheng, J. Fu, K. Alexopoulos, B. Saha, D. G. Vlachos, 'Molybdenum Oxide-Modified Iridium Catalysts for Selective Production of Renewable Oils for Jet and Diesel Fuels and Lubricants', *ACS Catal.,* 2019, **9** (9), 7679.
(13) A. Bugaev, A. H. Clark, N. S. Genz, O. V. Safonova, G. Smolentsev, M. Nachtegaal, 'X-ray Spectroscopy at the SuperXAS and Debye Beamlines: from in situ to Operando', *CHIMIA,* 2024, **78** (5), 304.
(14) A. H. Clark, P. Steiger, B. Bornmann, S. Hitz, R. Frahm, D. Ferri, M. Nachtegaal, 'Fluorescence-detected quick-scanning X-ray absorption spectroscopy', *J. Synchrotron Radiat.,* 2020, **27** (3), 681.
(15) A. H. Clark, J. Imbao, R. Frahm, M. Nachtegaal, 'ProQEXAFS: a highly optimized parallelized rapid processing software for QEXAFS data', *J. Synchrotron Radiat.,* 2020, **27** (2), 551.
(16) B. Ravel, M. Newville, 'ATHENA, ARTEMIS, HEPHAESTUS: data analysis for X-ray absorption spectroscopy using IFEFFIT', *J. Synchrotron Radiat.,* 2005, **12** (4), 537.